
THEORY AND DESIGN OF VARIABLE CONDUCTANCE HEAT PIPES: HYDRODYNAMICS AND HEAT TRANSFER

Research Report No. 1

APRIL 1971

Prepared by
B.D. MARCUS

Contract No. NAS 2-5503

Prepared for
AMES RESEARCH CENTER
NATIONAL AERONAUTICS AND SPACE ADMINISTRATION
Moffett Field, California 93405

TRM
SYSTEMS GROUP

REPRODUCED BY
NATIONAL TECHNICAL
INFORMATION SERVICE
U. S. DEPARTMENT OF COMMERCE
SPRINGFIELD, VA. 22161

(NASA-CR-146195) THEORY AND DESIGN OF
VARIABLE CONDUCTANCE HEAT PIPES:
HYDRODYNAMICS AND HEAT TRANSFER (TRM Systems
Group)

N76-71509

Unclas
00/98 09226

FOREWORD

The work described in this report was performed under NASA contract NAS2-5503, "Design, Fabrication, and Testing of a Variable Conductance Constant Temperature Heat Pipe". The contract is administered by Ames Research Center, Moffett Field, California, with Mr. J. P. Kirkpatrick serving as Technical Monitor.

The program is being conducted by TRW Systems Group of TRW, Inc., Redondo Beach, California, with Dr. Bruce D. Marcus serving as Program Manager and Principal Investigator. Major contributors to the effort include Mr. G. L. Fleischman and Prof. D. K. Edwards.

TABLE OF CONTENTS

	<u>Page</u>
1.0 INTRODUCTION	1
2.0 LITERATURE REVIEW	3
3.0 CONVENTIONAL HEAT PIPE THEORY	4
3.1 Hydrodynamics	4
3.1.1 Capillary Head	4
3.1.2 Liquid Pressure Drop	8
3.1.3 Vapor Pressure Drop	10
3.1.4 Body Force Head	11
3.1.5 Integrating the Flow Equations	15
3.1.6 Capillary Pumping Limit	18
3.1.7 Entrainment Limit	23
3.1.8 Sonic Limit	28
3.2 Heat Transfer	29
3.2.1 Evaporator Heat Transfer - Boiling in the Wick	30
3.2.2 Condenser Heat Transfer	36
4.0 CONVENTIONAL HEAT PIPE DESIGN	37
4.1 Wick Design	37
4.1.1 Effective Pore Radii of Various Wicks	38
4.1.2 Permeability of Various Wicks	46
4.1.3 Wick Optimization	51
4.1.4 Composite Wicks	60
4.2 Fluid Inventory	73
4.2.1 Fluid Inventory Variations	75
4.3 Excess Fluid Reservoirs	80
4.4 Working Fluid	82
4.4.1 Operating Temperature Range	82
4.4.2 Heat Transfer Requirements	83
4.4.3 Expected Body-Force Field	83
4.4.4 Tolerance of Wick Structure to Boiling	85

	<u>Page</u>
4.4.5 Conventional or Variable Conductance	
Heat Pipe	85
4.4.6 Special Requirements	88
4.4.7 Materials Compatibility and Stability . .	88
4.4.8 Summary	95
5.0 SELECTED BIBLIOGRAPHY PERTINENT TO SPACECRAFT	
THERMAL CONTROL	97
5.1 Hydrodynamics & Hydrostatics	97
5.2 Heat Transfer	99
5.3 Materials Compatibility	100
5.4 Variable Conductance Techniques	101
5.5 General	102
6.0 NOMENCLATURE	105

FIGURES

- 3-1 Schematic of Cylindrical Heat Pipe
- 3-2 Hydrodynamic Model Showing Effect of Body Force Component Perpendicular to Heat Pipe Axis
- 3-3 Capillary Pumping Limit Pressure Balance Graphs for Various Heat Pipe Configurations
- 3-4 Estimated Heat Pipe Entrainment and Sonic Axial Heat Flux Limitations for Water
- 3-5 Estimated Heat Pipe Entrainment and Sonic Axial Heat Flux Limitations for Ammonia
- 3-6 Estimated Heat Pipe Entrainment and Sonic Axial Heat Flux Limitations for Methyl Alcohol
- 4-1 Capillary Model for Parallel Wire Wick
- 4-2 Effective Pore Size for Parallel Wire Wick
- 4-3 Permeability of Wire Mesh Wicks
- 4-4 Wire Mesh Optimization Graph
- 4-5 Heat Pipe Optimization
- 4-6 Composite Wick Heat Pipes
- 4-7 Heat Flow Path for a Circumferentially Grooved Heat Pipe
- 4-8 Non-Arterial Composite Wick Design - Radial Heat Transfer De-coupled from Axial Liquid Flow
- 4-9 Self-priming Capacity of Pedestal Artery Heat Pipe with Ammonia Working Fluid
- 4-10 Liquid Volume Variation with Operating Temperature - Ammonia
- 4-11 Pressure Balance Criterion for Locating Excess Fluid Reservoir
- 4-12 Liquid Transport Factor for Heat Pipe Working Fluids
- 4-13 g-Field Figure of Merit for Heat Pipe Working Fluids
- 4-14 Nucleation Tolerance Parameter for Heat Pipe Working Fluids
- 4-15 Schematic Diagram of Gas Generation Compatibility Test
- 4-16 Compatibility Test Results - Heat Pipe No. 101

TABLES

4-1 Heat Pipe Materials Compatibility Matrix

4-2 Potential Heat Pipe Working Fluids for Spacecraft Thermal Control

1.0 INTRODUCTION

Heat pipe technology has advanced rapidly in the six years since Grover, et al, at Los Alamos, published their first paper [G1]. From the simple tube lined with a screen mesh, heat pipes are now being fabricated in many geometries with complex, multi-component capillary wick structures tailored to maximize their performance. Much work has been done to advance heat pipe hydrodynamics, heat transfer, materials compatibility and fabrication technology. However, one of the most important areas of endeavor has been in heat pipe control.

The heat pipe described by Grover is a completely passive device whose operating temperature automatically adjusts to the heat source and sink conditions so as to maintain conservation of energy. However, it was not long before investigators recognized the many potential applications of heat pipes which could be controlled, either actively or passively, to regulate temperatures. Numerous schemes have since been devised to accomplish this control, and many of these have been implemented. However, as is often the case in a rapidly advancing technology, the ability to accurately design and predict the performance of these devices had lagged the ability to build and operate them.

This program represents an effort to improve this situation through a comprehensive review and analysis of all aspects of heat pipe technology pertinent to the design of self-controlled, variable conductance, constant temperature devices for spacecraft thermal control. Subjects considered include hydrostatics, hydrodynamics, heat transfer into and out of the pipe, fluid selection, and materials compatibility, in addition to numerous variable conductance control techniques.

This report presents the results of efforts to date in each of the areas mentioned except variable conductance techniques. The theory and design practice relating to heat pipe control will be covered in an additional report to follow shortly: Research Report No. 2 - "Theory and Design of Variable Conductance Heat Pipes: Control Techniques". Since this

is a continuing program, some of the material presented herein constitutes the current status of work in progress. In other cases, the work has been completed and the material presented serves to document these accomplishments.

In addition to the fundamental studies described, a major endeavor on this program was the design, fabrication and testing of prototype, qualification and flight units for the Ames Heat Pipe Experiment on board the OAO-C spacecraft. This experiment, which involves a functional internal reservoir gas controlled heat pipe, is currently scheduled for launch in February 1972. Although several fundamental studies, ancillary to the experiment, are presented in this report, the detailed documentation of this phase of the program is not. Instead, it constitutes a separate report; the "Ames Heat Pipe Experiment Description Document," to be issued shortly.

2.0 LITERATURE REVIEW

Judging by the remarkable growth rate of the literature, the heat pipe field has indeed attracted the interest of many workers in academia, industry and government. Whereas, in 1965, the pertinent literature numbered but a few documents, TRW's current heat pipe bibliography contains well over three hundred references.

As one task on this program, all of the identified and available literature was reviewed to select that information pertinent to the design of variable conductance heat pipes for spacecraft thermal control. The selective bibliography thus obtained is presented in Section 5.

Where possible, references have been cataloged as to their principal subject. These include:

- Hydrodynamics & Hydrostatics
- Heat Transfer
- Materials Compatibility
- Variable Conductance Techniques

Where references are too broad for inclusion in one of these categories, they have been listed under the "General" heading.

The specific literature of greatest importance to this program is identified throughout the body of this report where each of the pertinent subjects are discussed.

3.0 CONVENTIONAL HEAT PIPE THEORY

The theory of heat pipes has been developing for many years and is well documented in the literature (see Section 5). Consequently, it will not be developed again in its entirety within this report. Rather, a review of current theory is presented which provides a basis for the hydrodynamic and thermal design of variable conductance heat pipes. In those cases where new contributions to the theory have been made as a result of efforts on this program, detailed developments are presented.

3.1 Hydrodynamics

Because the heat pipe involves the circulation of a working fluid, certain pressure drops arise. In general, there will be viscous losses due to liquid flow in the wick or capillary structure, and viscous and inertial losses due to vapor flow in the core. In addition, there may be body forces which either aid or hinder circulation (e.g., acceleration fields due to gravity, rotation, rocket thrust, etc.). For steady-state operation of a heat pipe, a pressure head equal to the sum of these losses must be supplied by capillarity in the wick. This yields the following steady-state pressure balance, which must be satisfied between all points along the heat pipe.

$$\Delta P_c = \Delta P_l + \Delta P_v \pm \Delta P_b \quad (3-1)$$

$$\left[\begin{array}{c} \text{net} \\ \text{capillary} \\ \text{head} \end{array} \right] = \left[\begin{array}{c} \text{liquid} \\ \text{pressure} \\ \text{drop} \end{array} \right] + \left[\begin{array}{c} \text{vapor} \\ \text{pressure} \\ \text{drop} \end{array} \right] \pm \left[\begin{array}{c} \text{body force} \\ \text{head} \\ \text{(if any)} \end{array} \right]$$

3.1.1 Capillary Head

Of the terms in Eq. (3-1), the liquid and vapor pressure drops are functions of the circulation rate and increase with the heat transfer load on the device. On the other hand, the body force term is usually independent of load. Thus, to satisfy Eq. (3-1), the capillary head

must also increase with load in such a way as to match the losses incurred.

The capillary head in a saturated heat pipe wick arises as a dynamic phenomenon. It is due to the existence of a pressure difference across a curved liquid-vapor interface which is given by:

$$\Delta P_i = \sigma \left(\frac{1}{R_1} + \frac{1}{R_2} \right) \quad (3-2)$$

where:

- ΔP_i - interfacial pressure difference
- σ - surface tension
- R_1, R_2 - two orthogonal radii of curvature of the interface

This pressure difference, which for concave menisci results in a depression of the liquid pressure with respect to the vapor, exists all along the heat pipe wick. In order to obtain a net capillary head, it is necessary for it to be greater at the evaporator than at the condenser. In a heat pipe under load, this is exactly what occurs due to changes in the interface curvatures. Vaporization of the liquid in the evaporator causes the menisci to recede into the wick resulting in a decrease in radii of curvature while condensation in the condenser has the opposite effect. Therefore, the capillary pressure is not constant. Capillary pumping is a passive phenomenon which automatically adjusts to meet the flow requirements--within limits.

The extremes of the interfacial pressure difference (Eq. 3-2) which can be generated along the wick depend on the wick pore geometry and the wetting angle between the liquid and wick material. The appropriate values for these extremes has been the subject of a good deal of heat pipe literature [H1, H2, H3, G2].

Class A Wicks:

In many wick structures, the maximum value of the interfacial pressure difference corresponds to the minimum possible values of R_1 and R_2 . These might be referred to as "Class A" wicks. For cylindrical pores, which fall into this category, it is easily shown [G2] that this is given by:

$$\Delta P_{imax} = \frac{2\sigma \cos \psi}{r_p} \quad (3-3)$$

where:

ψ - wetting angle

r_p - actual pore radius

On the other hand, it seems to be generally accepted that, in a practical heat pipe, the liquid meniscus cannot exhibit a significant convex curvature. Thus, the maximum liquid pressure at any point along the wick surface cannot exceed the local static vapor core pressure.

Consequently, the maximum net capillary head (ΔP_{cmax}) which can be generated between various points along a heat pipe is equal to ΔP_{imax} .

The capillary head, as given by Eq. (3-3), applies only to cylindrical pores, which is not characteristic of most class A heat pipe wicks. However, the form of this equation has been generally adapted for all such wicks by replacing the cylindrical pore radius (r_p) with an "effective" pore radius (r_{eA}) so calculated or measured as to render the equation applicable. Thus, in general:

$$\Delta P_{cmax} = \frac{2\sigma \cos \psi}{r_{eA}} \quad (\text{Class A wicks}) \quad (3-4a)$$

Class B Wicks:

It has been proposed [H3] that, for many heat pipe wicks, the maximum interfacial pressure difference which can be generated in the evaporator does not correspond to the minimum possible meniscus radii of curvature, but rather to the coalescence of adjacent menisci prior to the attaining

of a minimum surface free energy configuration. Under such circumstances, it is suggested that ΔP_{cmax} is independent of the wetting angle ψ . Thus, referring to these as "Class B" wicks, we have:

$$\Delta P_{cmax} = \frac{2\sigma}{r_{eB}} \quad (\text{Class B wicks}) \quad (3-4b)$$

For certain well-defined pore geometries, the effective pore radius can be analytically determined (see Section 4.1.1). However, in many cases (e.g., metal felts and foams, woven fabrics, sintered particles) this parameter must be experimentally measured.

There are several standard techniques utilized to make these measurements. These include, (1) measuring the height to which a wick will lift fluid against gravity [G3], (2) measuring the pressure difference required to break the menisci at the wick surface [H4], and (3) utilizing the hydrodynamic theory (to be discussed later) in conjunction with actual or simulated heat pipe performance measurements [H5].

Equations (3-4a) and (3-4b) presume a unique wick pore size. Thus, for completely isotropic wicks of uniform pore size, each of these measurement methods would yield the same result. However, this is usually not the case with heat pipe wicks, and thus the results differ. The rise test measures the smallest wick pores while the pressure test measures the largest wick pores. Since it is the largest pores which fail first in a heat pipe under load, the pressure test yields more realistic results. Most preferable, however, is the simulated or actual heat pipe test, for this measures the largest pores which are saturated at given operating conditions. Under certain conditions (e.g., operating against gravity) the largest pores of a wick with a pore size distribution can be desaturated at the evaporator without resulting in pipe failure. Instead the heat pipe continues to operate on the smaller pores, but with reduced capacity due to partial wick desaturation. This experimental technique is unique in that it allows measuring the effective pore size as a function of the body force head.

3.1.2 Liquid Pressure Drop

Liquid flow in heat pipe wicks is generally characterized by very low flow velocities and Reynolds numbers. Consequently, inertial effects can be neglected for steady-state operation, and the flow losses attributed only to viscous shear. Treating a cylindrical heat pipe (Fig. 3-1), with these assumptions, Cotter [H1] derived an expression for the liquid pressure gradient in the wick due to shear loss as follows:

$$\frac{dP_L}{dz} = + \frac{b\mu_L \dot{m}_L(z)}{A\rho_L \phi r_p^2} \quad (3-5)$$

where:

- μ_L - liquid viscosity
- ρ_L - liquid density
- $\dot{m}_L(z)$ - local axial mass flow rate
- A - wick cross sectional area
- ϕ - wick porosity
- b - tortuosity factor
- r_p - wick pore radius

Actually, as pointed out in reference [G4], Eq. (3-5) is a rigorous solution for flow in parallel circular capillaries of radius r_p when the tortuosity factor is set equal to 8. As with Eq. (3-3) for maximum capillary head, Eq. (3-5) has been generalized for all wick structures by setting r_p equal to the effective pore radius and including an empirical constant - b .

Again, the constant b can be calculated for certain well defined wick geometries, but in most cases must be measured. In fact, what is usually measured is the grouping $\frac{b}{\phi r_p^2}$.

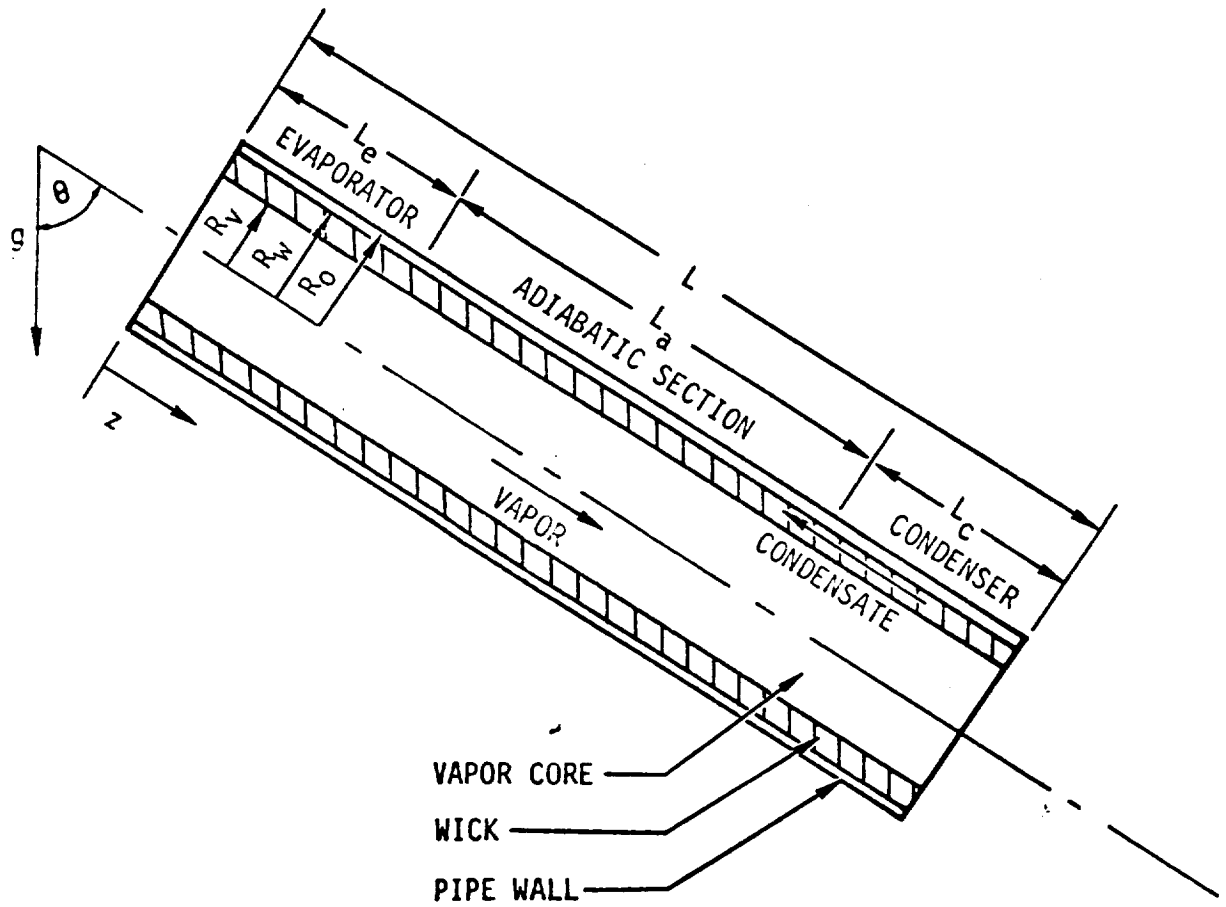


FIGURE 3-1. Schematic of Cylindrical Heat Pipe

Equation (3-5) is, in essence, a form of Darcy's Law for flow in porous media. Usually, Darcy's Law is expressed in terms of a permeability - K , which is a measure of the wick flow resistance.

$$\frac{dP_\ell}{dz} = + \frac{\mu_\ell \dot{m}_\ell (z)}{KA\rho_\ell} \quad (3-6)$$

Comparing Eqs. (3-5) and (3-6), it is seen that the grouping $\frac{b}{\phi r_p^2}$ is equivalent to the reciprocal of the permeability. Since both of these are usually empirically determined quantities, it seems preferable to use the more familiar form of the flow equation (Eq. 3-6). This is particularly true in that for many wicks (e.g., screens, metal felt), the pore geometry for axial flow is not the same as that for radial pumping. Thus, setting r_p in Eq. (3-5) equal to r_e as defined by Eq. (3-4) is somewhat misleading.

3.1.3 Vapor Pressure Drop

The vapor pressure drop in heat pipes is often considerably more difficult to calculate than that in the liquid, for in addition to viscous shear, the analysis must account for momentum effects and perhaps turbulent flow and compressibility. Complicating this analysis is the fact that mass addition in the evaporator and mass removal in the condenser can significantly alter the velocity profiles and, hence, the local pressure gradient.

In terms of heat pipes used for spacecraft thermal control, however, evaporation rates, condensation rates, and axial vapor velocities are usually relatively small. Under such circumstances laminar flow exists throughout the system, and the vapor pressure gradient can be approximated by the sum of two terms, that due to viscous shear and that due to momentum gradients in the evaporator and condenser. As discussed by Katsoff [G5], the gradient due to friction is given by:

$$\left(\frac{dP_v}{dz}\right)_f = - \frac{8\dot{m}_v(z)\mu_v}{\rho_v A_v R_v^2} \quad (3-7)$$

and the gradient due to momentum changes by:

$$\left(\frac{dP_v}{dz}\right)_m = - \frac{8\dot{m}_v(z)}{3\rho_v A_v^2} \frac{d\dot{m}_v(z)}{dz} \quad (3-8)$$

where:

- $\dot{m}_v(z)$ - local mass flow rate
- μ_v - vapor viscosity
- ρ_v - vapor density
- R_v - radius of vapor core
- A_v - vapor core flow area

More rigorous treatments of the vapor pressure loss can be found in the literature [H1, H6, H7, H8, G4]. However, they yield very nearly the same expressions as given by Eq. (3-7) and (3-8), differing only slightly in the constant terms.

Since in spacecraft thermal control type heat pipes the vapor pressure loss is generally quite small, and often negligible, the equations presented here can be used with little error.

3.1.4 Body Force Head

The last term in the pressure balance equation (Eq. 3-1) is the pressure head due to body forces acting on the fluid - ΔP_b . Most frequently, body forces arise as a result of acceleration fields due to gravity, rotation, rocket thrust, etc. In these cases the body force head is dependent on the acceleration field, fluid density, heat pipe geometry and orientation, and is not dependent on the flow velocities. There do exist exceptions to this, such as electromagnetic body forces on a liquid metal flowing in a magnetic field gradient [H8], but this situation does not usually arise in spacecraft thermal control applications.

Furthermore, in all practical situations, the density of the vapor is very much lower than that of the liquid, so that body forces on the vapor can be neglected. Thus, for cases of interest in this program, the body force on the liquid is a vector quantity, independent of heat load, given by:

$$F_b = \rho_l \bar{g} dV \quad (3-9)$$

where:

\bar{g} - acceleration field vector
 dV - volume element

The fact that the body force is a vector quantity is of considerable significance. The cylindrical heat pipe theory presented here and in most of the literature is based on a one-dimensional hydrodynamic model. Thus, the contribution of body forces has typically been calculated by integrating the axial component of the body force along the length of the pipe [H1, G4].

$$\Delta P_{b_{ax}} = \int \frac{dP_b}{dz} = \pm \int \rho_l g \cos \theta \, dz \quad (3-10)$$

where:

$\Delta P_{b_{ax}}$ - axial component of body force head
 g - magnitude of acceleration field
 θ - angle of heat pipe axis with respect to
 acceleration field vector (see Fig. 1)
 dz - elemental length

The component of the body force perpendicular to the pipe axis has usually been neglected. Integrated over the wick diameter - D_w this is given by:

$$\Delta P_{b_{\perp}} = D_w \rho_l g \sin \theta \quad (3-11)$$

Contrary to common practice, this component of the body force cannot be ignored. Clearly, in a spinning satellite, a high centrifugal field perpendicular to the pipe axis can render g in Eq. (3-11) so large as to completely dry the wick on one side of the heat pipe. However, even under less severe conditions, such as 1-g testing in the laboratory, the head corresponding to the pipe diameter can have a very significant effect. This is particularly true for the low surface tension fluids commonly used in spacecraft thermal control heat pipes (e.g., ammonia, methanol, freon).

This effect becomes clear when one considers the model shown in Fig. 3-2.

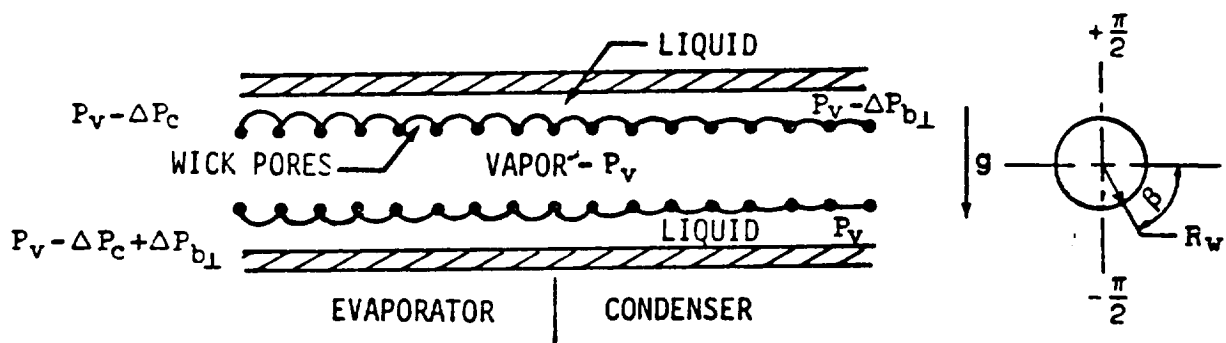


FIGURE 3-2. Hydrodynamic Model Showing Effect of Body Force Component Perpendicular to Heat Pipe Axis

The assumptions made are:

- The pipe is horizontal in a gravity field
- The vapor pressure loss is negligible*
- Liquid flow is in the axial direction only
- The wick is thin ($R_v \approx R_w$)

The figure shows a typical variation in pore menisci for a heat pipe operating under the assumed conditions. It was previously established that the maximum liquid pressure is equal to the local vapor core pressure - P_v and the minimum liquid pressure was equal to $P_v - \Delta P_c$ (Section 3.1.1).

The maximum liquid pressure (P_v) will exist at the end of the condenser along the bottom of the pipe ($\beta = -\frac{\pi}{2}$). Thus, the circumferential distribution of liquid pressure at this axial position is given by:

$$P_l(\beta)_c = P_v - \rho_l g(R_w + R_w \sin\beta) \quad (3-12)$$

where R_w is the wick radius.

At the top of the pipe, this yields $P_l = P_v - \Delta P_{b\perp}$. On the other hand, the minimum liquid pressure ($P_v - \Delta P_c$) will exist at the beginning of the evaporator along the top of the pipe. The circumferential distribution of pressure at this end is thus given by:

$$P_l(\beta)_e = (P_v - \Delta P_c) + \rho_l g(R_w - R_w \sin\beta) \quad (3-13)$$

At the bottom of the pipe, this yields $P_l = P_v - \Delta P_c + \Delta P_{b\perp}$.

Now, since liquid pumping is proportional to the axial gradient in liquid pressure, it is possible to obtain an averaged value of this parameter for the heat pipe by circumferentially averaging the quantity $[P_l(\beta)_c - P_l(\beta)_e]$. Thus, using symmetry to treat half the pipe,

*Vapor pressure losses do not change the results, but complicate the model.

$$\overline{\Delta P}_\ell = \frac{1}{\pi} \int_{-\frac{\pi}{2}}^{+\frac{\pi}{2}} \left[P_V - \rho_\ell g (R_W + R_W \sin \theta) - (P_V - \Delta P_C) - \rho_\ell g (R_W - R_W \sin \theta) \right] d\theta \quad (3-14)$$

$$= \frac{1}{\pi} \int_{-\frac{\pi}{2}}^{+\frac{\pi}{2}} (\Delta P_C - 2\rho_\ell g R_W) d\theta$$

$$= \Delta P_C - 2\rho_\ell g R_W$$

Substituting the wick diameter - D_W for $2R_W$, we finally get:

$$\overline{\Delta P}_\ell = \Delta P_C - \rho_\ell g D_W = \Delta P_C - \Delta P_{b_\perp} \quad (3-15)$$

Thus, it is seen that the available pumping head for a horizontal pipe is not ΔP_C , but that value reduced by the perpendicular body force head. In other words, the body force head to be used in the heat pipe pressure balance must include both the axial and perpendicular components. However, whereas the axial contribution can either aid or hinder performance, the perpendicular component is always a degrading factor. Thus, for a cylindrical heat pipe,

$$\left. \begin{aligned} \frac{dP_b}{dz} &= \pm \rho_\ell g \cos \theta \\ \text{but, } \Delta P_b &= \rho_\ell g \left[D_W \sin \theta \pm \int \cos \theta dz \right] \end{aligned} \right\} \quad (3-16)$$

3.1.5 Integrating the Flow Equations

In sections 3.1.1 through 3.1.4, equations were presented for each of the four elements making up the pressure balance equation (Eq. 1). These are summarized as follows:

$$\text{Maximum Capillary Head: } \Delta P_{\text{cmax}} \begin{cases} \frac{2\sigma \cos \psi}{r_{eA}} & (\text{Class A wicks}) \\ \frac{2\sigma}{r_{eB}} & (\text{Class B wicks}) \end{cases} \quad (3-4)$$

$$\text{Liquid Flow Loss: } \frac{dP_{\ell}}{dz} = \frac{\mu_{\ell} \dot{m}_{\ell}(z)}{KA_{\rho_{\ell}}} \quad (3-6)$$

Vapor Pressure Loss:

$$\text{Friction: } \left(\frac{dP_v}{dz} \right)_f = - \frac{8\dot{m}_v(z)\mu_v}{\rho_v A_v R_v^2} \quad (3-7)$$

$$\text{Momentum: } \left(\frac{dP_v}{dz} \right)_m = - \frac{8\dot{m}_v(z)}{3\rho_v A_v^2} \frac{d\dot{m}_v(z)}{dz} \quad (3-8)$$

$$\text{Body Force Head: } \frac{dP_b}{dz} = \pm \rho_{\ell} g \cos \theta \quad (3-16)$$

$$\Delta P_b = \rho_{\ell} g \left[D_w \sin \theta \pm \int \cos \theta \, dz \right]$$

These equations are generally applicable to all one-dimensional type heat pipes (tubes of any cross section) which operate in the temperature and heat load ranges applicable to spacecraft thermal control.* Also, since the loss equations are in differential form, there are no restrictions on the number of evaporator and condenser sections, the flux distribution along them, or axial changes in the wick system or pipe geometry.

*For other than circular cross sections, the hydraulic radius and an appropriate shape factor should be substituted for R_v in Eq. (3-7). Also, the required static pumping height for the liquid at $\theta = 90^\circ$ should be substituted for D_w in Eq. (3-16).

To apply the equations to a particular heat pipe one simply integrates the loss terms over the pipe length. To accomplish this, however, several ancillary equations are required. First, continuity requires that, at any axial position - z , the vapor and liquid flow rates must be equal. Thus,

$$\dot{m}_l(z) = \dot{m}_v(z) \quad (3-17)$$

Second, neglecting axial wall conduction and sensible heat transport [H1, G2], the mass flow rate of change is related to the heat transfer rate per unit length as follows:

$$\frac{d\dot{m}(z)}{dz} = \frac{Q'}{\lambda} \quad (3-18)$$

where:

- Q' - radial heat transfer rate per unit length
- λ - latent heat of vaporization

For all but the simplest systems, integration of the flow losses is best performed numerically. However, one configuration, which is of significant practical importance, is readily solved analytically. This is the system shown on Fig. 3-1, consisting of a tube with single evaporator and condenser sections at the ends of the pipe, with or without an intervening adiabatic section. Also, the pipe geometry and wick are uniform axially as is the heat input and rejection over the evaporator and condenser respectively. Under such circumstances, the losses are given by [G4]:

$$\begin{aligned} \Delta P_l &= \frac{Q (L + L_a) \mu_l}{2\pi K_{ol} \lambda (R_w^2 - R_v^2)} \\ \Delta P_v &= \frac{4Q (L + L_a) \mu_v}{\pi \rho_v \lambda R_v^4} \\ \Delta P_b &= \rho_l g [D_w \sin\theta + L \cos\theta] \end{aligned} \quad (3-19)$$

where:

- Q - total axial heat transport
- L - total pipe length
- L_a - length of adiabatic section
- R_v - vapor core radius
- R_w - wick radius

3.1.6 Capillary Pumping Limit

The fact that there exists a maximum capillary head for any wick-fluid combination (Eq. 3-4) results in a hydrodynamic limit on heat pipe capacity. As mentioned previously, the capillary head must increase with the liquid and vapor pressure drops as the heat load (and hence the fluid circulation rate) increases. Since there exists a limit on the capillary head, there also exists a corresponding limit on the heat load if the pressure balance criterion (Eq. 3-1) is to be satisfied. This defines the capillary pumping limit.

In the general case, the capillary pumping limit is established for a given heat pipe by integrating the pressure drop equations along the pipe (as described in the last section) and comparing the sum of the losses at all points with the local maximum capillary head. Since the maximum capillary head and the body force head are usually not dependent on load, the capillary pumping limit criteria is most clearly defined by transposing Eq. (3-1), using ΔP_{cmax} , to read:

$$\Delta P_{cmax} - \Delta P_b \geq \Delta P_l + \Delta P_v \quad (3-20)$$

In Eq. (3-20), only the terms on the right hand side are load dependent. Thus, the heat pipe operates below the capillary pumping limit as long as the inequality holds everywhere along the pipe. When the load increases so that the two sides of the equation are equal at any point along the pipe, the capillary pumping limit has been reached. Thus, to calculate the capillary pumping limit for a given heat pipe, the heat load is progressively increased until such an equality occurs. This is shown in Fig. 3-3 for a number of heat pipe configurations.

Fig. 3-3a represents a conventional heat pipe, with uniform heat transfer over the evaporator and condenser, operating against gravity. The pressure balance graph is drawn for the capillary pumping limit--that is, the sum of the liquid and vapor pressure drops just equals the maximum capillary head minus the body force head. In this case the failure point (shown as a dot) would occur on the top of the pipe at the beginning of the evaporator.

Fig. 3-3b depicts the same heat pipe operating in a gravity-aiding mode. Note that $\Delta P_{b,1}$ and $\Delta P_{b,II}$ are now of opposite sign. The critical point on the pipe is still at the beginning of the evaporator, but failure occurs at a higher value of $\Delta P_L + \Delta P_V$, and thus at a higher heat load.

Fig. 3-3c depicts a situation where there are multiple evaporator and condenser sections along the heat pipe. This does not change the failure criterion. The capillary pumping limit still occurs at the heat load for which the equality in Eq. (3-20) is first reached at any point in the pipe. The fact that the liquid and vapor pressure curves are no longer monotonic functions is due to an assumed flow reversal situation along the pipe.

In Fig. 3-3c the failure point is still shown at the beginning of the evaporator. However, the situation often arises where the distribution of evaporator and condenser loads are such that failure occurs elsewhere along the pipe. This is shown in Fig. 3-3d. Note that in this case the vapor pressure loss curve does not start at the origin. Rather the lowest point along this curve is set equal to zero. This is consistent with the fact that the pressure balance equation must be satisfied at all points along the heat pipe.

Fig. 3-3e represents a heat pipe with an axial composite wick. The wick in the evaporator is presumed to have a smaller effective pore size and a higher flow resistance than the condenser wick. The vapor pressure loss curve is not affected by the wick variation but the liquid loss curve is, showing a discontinuity in slope at the wick juncture. More important,

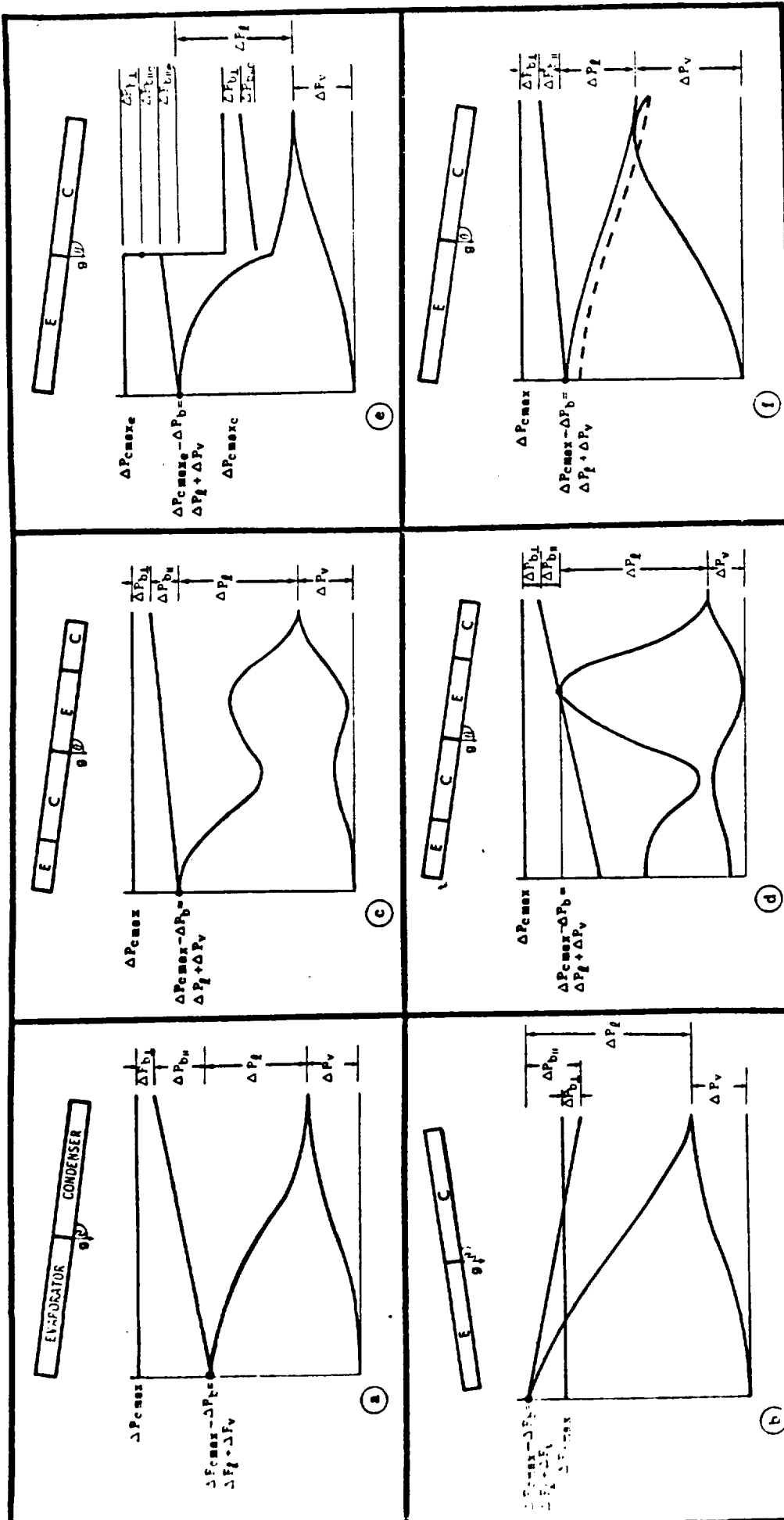


FIGURE 3-3. Capillary Pumping Limit Pressure Balance Graphs for Various Heat Pipe Configurations

the maximum capillary head is different in the two sections, giving rise to the pressure balance graph shown. Fig. 3-3e again shows the failure point at the beginning of the evaporator. However, it is clear that this could also occur at the beginning of the condenser if ΔP_{cmax} for the condenser were chosen a little lower. The object of using such composite wicks is, of course, to reduce the flow resistance in regions of the pipe where the sum of the flow losses is small, thus allowing higher circulation rates and heat loads. The simultaneous reduction in maximum capillary head within these regions can be tolerated (within limits) as shown in Fig. 3-3e.

Finally, Fig. 3-3f represents a case where the vapor flow is presumed high enough that the momentum pressure drop is significant (Eq. 3-8). Generally, for spacecraft thermal control heat pipes, the momentum drop is quite small; but for certain cases (very high loads at low operating pressure) it could be large enough so that recovery in the condenser leads to an extremum in the vapor loss curve as shown. Under such circumstances, the point of equal vapor and liquid pressure may no longer be at the end of the condenser as shown in Figs. 3-3a - e. This would yield the dashed line for $\Delta P_v + \Delta P_l$, which violates the requirement that the liquid be everywhere at a pressure equal to or lower than the local static vapor core pressure (sec. 3.1.1). Thus, the liquid loss curve must be elevated such that it is tangent to the vapor loss curve, and the point of tangency represents the position of equal liquid and vapor pressure. This phenomenon is discussed in more detail by Ernst [H2].

Note that this situation need not arise only as a result of momentum recovery. In the distributed source and sink case shown in Fig 3-3d, a slightly higher load on the interior condenser would result in tangency at the extremums of the loss curves rather than equality at the end of the pipe.

The six cases shown represent but a small number of possible situations. These cases were selected to demonstrate the pressure balance principle leading to a capillary pumping limit and the technique for calculating it. As stated earlier, the technique is generally applicable to heat pipes with any number of evaporator and condenser sections having arbitrary flux distributions along them, and can handle arbitrary axial variations in wicking or in pipe geometry.

Under certain simple configurations, numerical evaluation of the capillary pumping limit is not necessary. Thus, for the conventional heat pipe shown in Fig. 3-1, assuming uniform heat input and output, uniform wicking, and negligible momentum pressure drop, one can obtain a closed form analytical solution for this limit. To do this, one simply equates the maximum capillary head (Eq. 3-4) to the sum of the loss equations integrated over the entire length of the pipe (Eq. 3-19), yielding:

$$\left. \begin{array}{l} \frac{2\sigma\cos\psi}{r_{eA}} \\ \frac{2\sigma}{r_{eB}} \end{array} \right\} = \Delta P_{cmax} = \frac{Q(L + L_a)\mu_\ell}{2\pi K_\ell \lambda (R_w^2 - R_v^2)} + \frac{4Q(L + L_a)\mu_v}{\pi \rho_v \lambda R_v^4} + \rho_\ell g [D_w \sin\theta + L \cos\theta] \quad (3-21)$$

Solving for the maximum heat transport (capillary pumping limit) yields:

$$CPL = Q = \frac{\pi \lambda}{(L + L_a)} \frac{[\Delta P_{cmax} - \rho_\ell g (D_w \sin\theta + L \cos\theta)]}{\left[\frac{\mu_\ell}{2K_\ell (R_w^2 - R_v^2)} + \frac{4\mu_v}{\rho_v R_v^4} \right]} \quad (3-22)$$

3.1.7 Entrainment Limit

A phenomenon which can affect the capillary pumping limit, but is not included in Eq. (3-1), is liquid entrainment in the vapor. In a heat pipe, the vapor and liquid generally flow in opposite directions. Since they are in contact at the wick surface, this sets up a mutual drag at the vapor-liquid interface. If the relative velocity between the liquid and vapor becomes too great, the interface becomes unstable and droplets of liquid will be torn from the wick and entrained in the vapor. Since this liquid never reaches the evaporator, it cannot contribute to the heat transferred by the heat pipe. However, it does contribute to the liquid flow loss. Thus, the maximum axial heat transfer in the heat pipe is no longer equal to the maximum fluid circulation rate times the latent heat of vaporization, but is some lower value which defines the entrainment limit.

The conditions leading to entrainment are expressed in terms of the ratio of vapor inertial forces to liquid surface tension forces, called the Weber number:

$$We = \frac{\rho_v \bar{V}^2 z}{\sigma} \quad (3-23)$$

where:

- ρ_v - vapor density
- \bar{V} - average vapor velocity
- σ - liquid surface tension
- z - characteristic dimension associated with liquid surface

At present, limited experimental data with screen wicks indicate that a Weber number of unity represents the entrainment condition when the characteristic dimension, z , is set approximately equal to the screen wire diameter [H9].* This suggests that by using finer mesh screens,

*Some authors argue that the wire-to-wire spacing is a more appropriate value for z [G4]. Additional experimentation is necessary to resolve this question.

entrainment can be inhibited--an hypothesis which has been verified at Los Alamos.

For wick structures that do not involve screens, any construction which reduces interaction between the vapor and liquid will serve to raise the entrainment limit. On the other hand, open wick structures such as axial grooves cut in the wall are particularly susceptible to the effects of vapor-liquid drag [G6].

When the Weber number is set equal to unity, the limiting axial heat flux corresponding to incipient entrainment is given by:

$$\frac{Q_e}{A_v} = \left[\frac{\rho_v \sigma \lambda^2}{z} \right]^{\frac{1}{2}} \quad (3-24)$$

where:

- $\frac{Q_e}{A_v}$ - maximum axial heat flux for incipient entrainment
- A_v - vapor core flow area
- λ - latent heat of vaporization

Using Eq. (3-24), the entrainment limit was calculated for water, ammonia and methanol; the primary fluids of interest in spacecraft thermal control. Calculations were performed for a series of characteristic lengths - z .

The results are presented on Figs. 3-4, 3-5 and 3-6 along with sonic flow limit curves (to be discussed later). The figures also include a table of standard screen meshes whose wire diameters equal the characteristic dimensions used in the calculations. Assuming the equivalence of wire diameter and characteristic dimension establishes the entrainment limit curves as those applicable to the corresponding

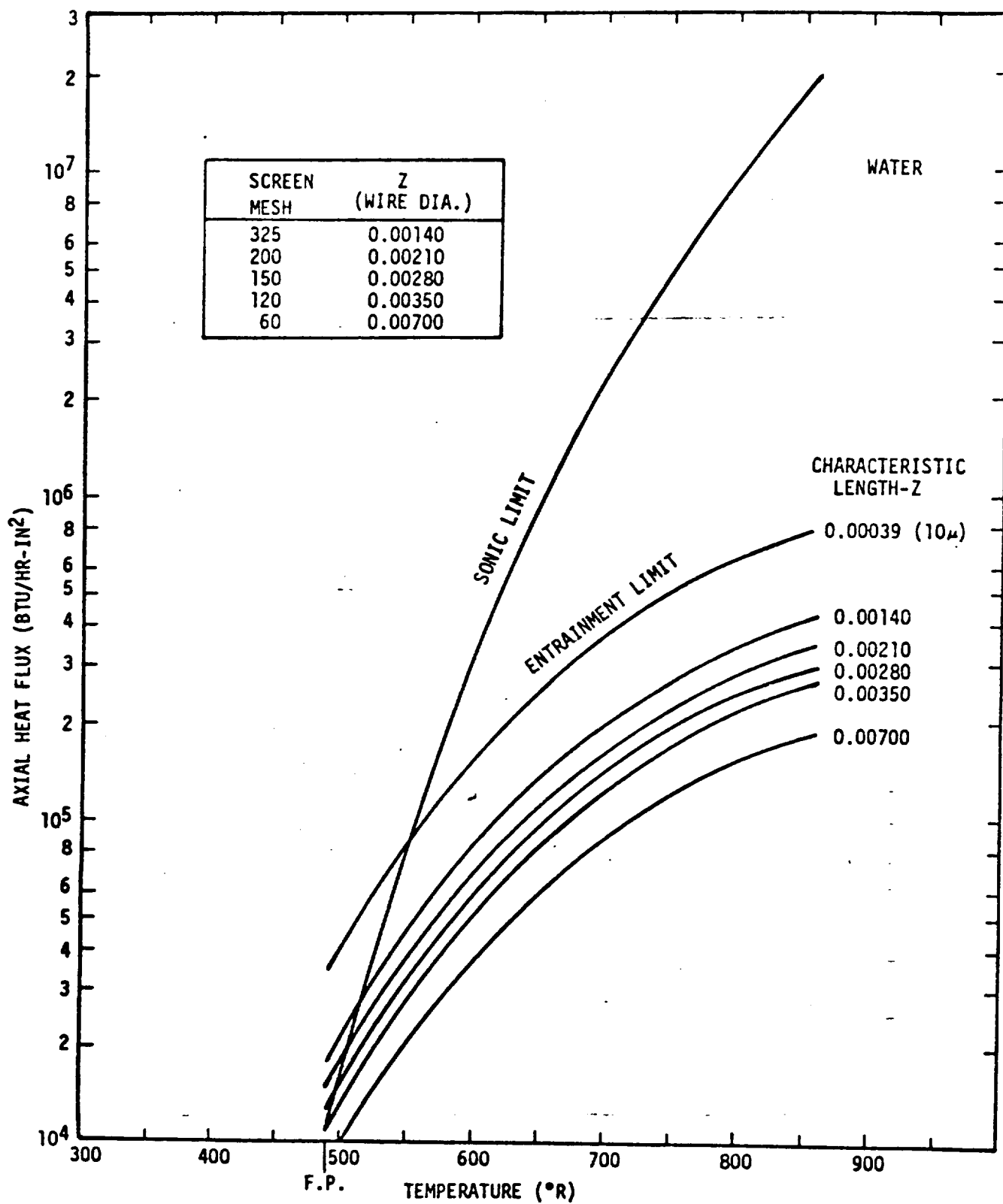


FIGURE 3-4. Estimated Heat Pipe Entrainment and Sonic Axial Heat Flux Limitations for Water

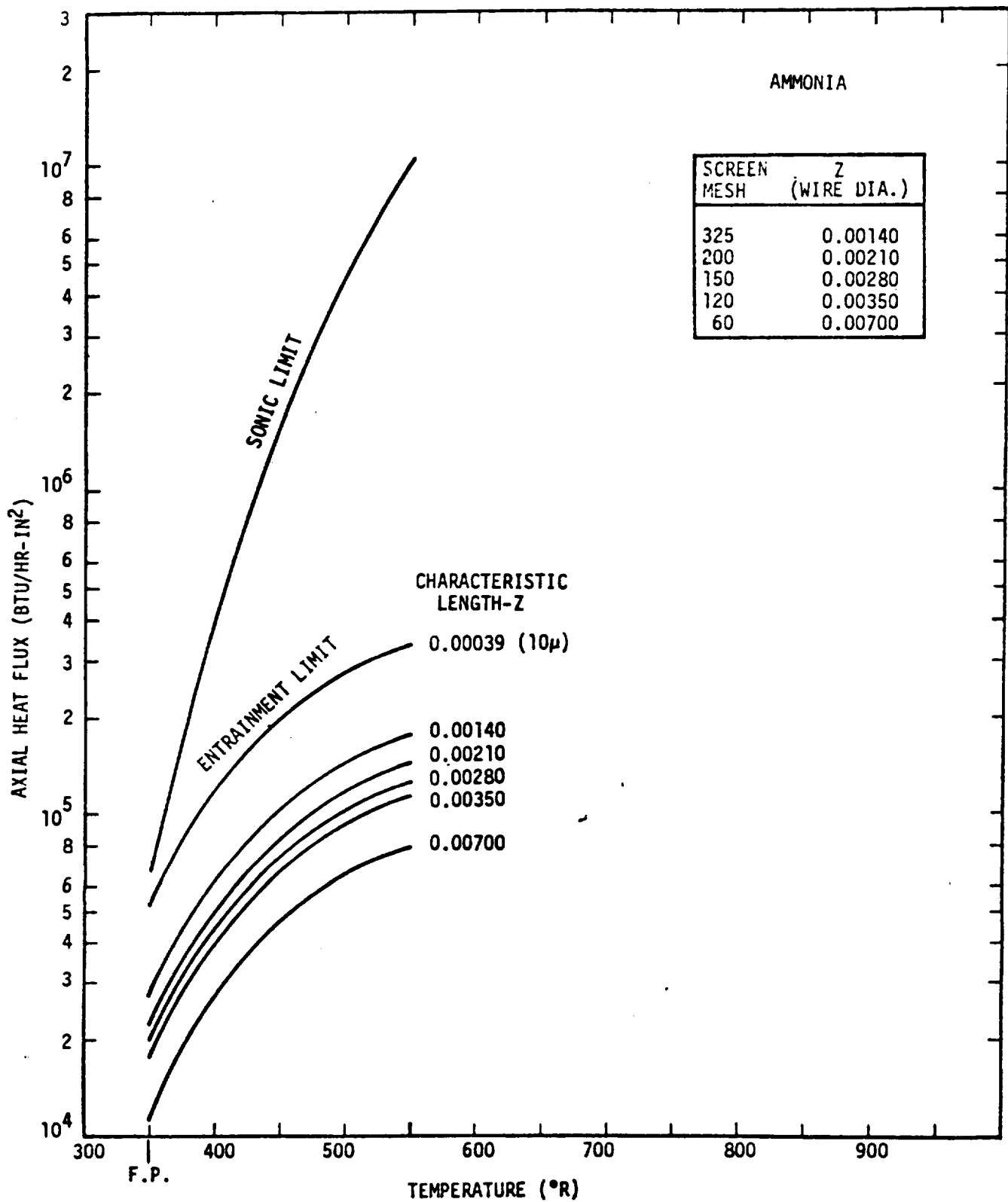


FIGURE 3-5. Estimated Heat Pipe Entrainment and Sonic Axial Heat Flux Limitations for Ammonia

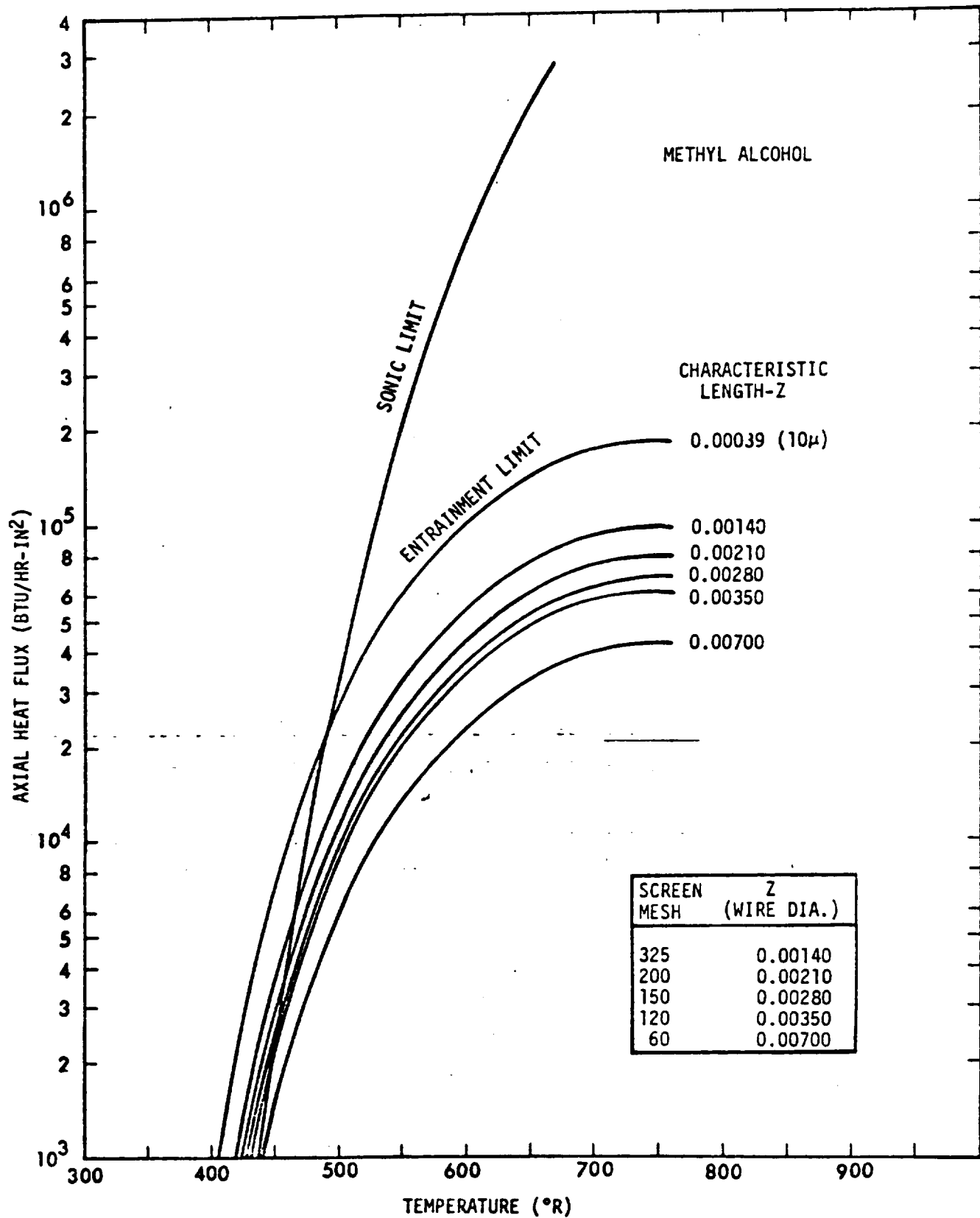


FIGURE 3-6. Estimated Heat Pipe Entrainment and Sonic Axial Heat Flux Limitations for Methyl Alcohol

screen mesh size. The curves are drawn in terms of z , however, and are valid whatever method is used to establish this value.

It was noted in the calculations that at high temperatures the surface tension decreases rapidly enough to result in a maximum in the curves. That is, the entrainment limit can actually decrease with increasing temperature. This is clearly seen from Eq. (3-24) since both σ and λ go to zero at the critical point.

3.1.8 Sonic Limit

It can be shown analytically [H10] that there is a correspondence between constant area flow in a heat pipe with mass addition (evaporator) and removal (condenser) and constant mass flow in a converging-diverging nozzle. The end of the evaporator section in the heat pipe corresponds to the throat of the nozzle. Consequently, just as there is a sonic (MACH 1) limitation on the flow velocity through a nozzle throat, there is a similar limit on the flow velocity at the heat pipe evaporator exit. For a given evaporator exit temperature and working fluid, this choked flow condition is a fundamental limitation on the axial heat flux capacity of the heat pipe. To increase the axial heat transfer capacity of the heat pipe, one must increase the vapor flow area.

The sonic limit is calculated by setting the vapor flow velocity equal to the sonic velocity in the continuity equation and multiplying by the latent heat of vaporization as follows:

$$\frac{Q_s}{A_v} = \lambda \rho_v V_s \quad (3-25)$$

where:

$\frac{Q_s}{A_v}$ - axial heat flux at MACH 1 conditions

V_s - sonic velocity of vapor

Using Eq. (3-25), the sonic limit was calculated for water, ammonia and methanol. The results are presented on Figs. 3-4, 3-5 and 3-6 along with the entrainment limit curves. Note that over most of the temperature range of interest in spacecraft thermal control, the sonic limit on axial heat flux exceeds the entrainment limit. Furthermore, except at very low temperatures, both limits are quite high ($>10^4$ Btu/hr-in²). Consequently, they are seldom encountered in the design of spacecraft thermal control heat pipes.*

When using Eq. (3-25) to calculate the sonic limit, the parameters must be evaluated at the local conditions where choking occurs (the exit of the evaporator). It is sometimes more convenient to calculate this limit in terms of conditions at the beginning of the evaporator. This can be done using an equation developed by Levy [H10]:

$$\frac{Q_s}{A_v} = \frac{\lambda_p V_s}{\sqrt{2(k+1)}} \quad (3-26)$$

where k = ratio of specific heats (C_p/C_v).

3.2 Heat Transfer

The fluid circulation phenomena discussed in the previous sections arise as a result of heat transfer into the heat pipe at the evaporator and out of it at the condenser. In most heat pipes this heat must be transferred through the pipe wall and saturated wick in both cases. Generally, these heat transfer processes are the major source of temperature drop in the heat pipe.**

*Except in the case of open axially grooved heat pipes where the vapor drag on the liquid can be appreciable.

**Temperature drops also arise due to the vapor flow losses along the pipe and to non-equilibrium at the vapor-liquid interfaces. However, these effects are relatively small unless the pipe operates under very high heat loads [H1, G2].

In many cases, the heat transfer process at the evaporator and condenser is by conduction in that the presence of the wick impedes convection. Thus, the temperature drop experienced in transferring heat into and out of the device is proportional to the local heat flux and wick-wall thickness, and inversely proportional to the effective thermal conductivity of the wall-wick-fluid composite.

3.2.1 Evaporator Heat Transfer - Boiling in the Wick

The fact that heat is transferred into the heat pipe through the wick gives rise to another limit on the heat pipe capacity. Frequently, liquid is vaporized only at the wick surface as a result of the heat conducted through the wick. However, the vapor at the wick surface is thermodynamically saturated. Consequently, the fluid within the wick at the evaporator is superheated by virtue of (1) the curvature of the menisci, and (2) the existing radial temperature gradient. The greatest superheat occurs at the interface of the wick and pipe wall. If this superheat becomes too large (it increases with the heat transfer rate), the fluid will begin to boil within the wick.

3.2.1.1 Nucleation Superheat

It is difficult to say just what level of liquid superheat must exist before nucleation (boiling) will begin at the pipe wall. However, using criteria similar to those which apply to nucleate boiling from planar surfaces, an estimate can be made. In this way, Marcus [G2] has shown that the critical evaporator superheat (temperature drop across the wick) is given by:

$$\Delta T_{\text{crit}} = \frac{T_{\text{sat}}}{J\lambda\rho_v} \left[\frac{2\sigma}{r_n} - \Delta P_c^* \right] \quad (3-27)$$

where:

- T_{sat} - saturation temperature of the fluid
- J - mechanical equivalent of heat
- r_n - effective radius of critical nucleation cavity
- ΔP_c^* - maximum value of capillary head along the evaporator

Note that ΔP_c^* does not equal ΔP_{cmax} as given by Eq. (3-4) unless the heat pipe is operating at the capillary pumping limit. Rather, it is the maximum value of ΔP_c (as given by Eq. (3-1)) along the evaporator section(s) of the pipe.

Generally, all of the terms on the right hand side of Eq. (3-27) are known except r_n , which is a function of the boiling surface finish. To establish the appropriate value of r_n , one should first establish its value assuming cavities of all sizes were present on the surface, and then impose appropriate limits. This can be done using the nucleation theory of Rohsenow and Bergles [T1]. Their equation for r_n is:

$$r_n = \left[\frac{2\sigma T_{sat} k_l v_{lg}}{\lambda q'_r} \right]^{1/2} \quad (3-28)$$

where:

- k_l - thermal conductivity of liquid
- v_{lg} - difference in specific volumes of vapor and liquid
- q'_r - radial heat flux into evaporator

The value of r_n given by Eq. (3-28) is the appropriate one to use in Eq. (3-27), assuming that cavities of such size exist on the surface and are potential nucleation sites.* On typical smooth surfaces, the largest potential nucleation sites have critical radii between 10^{-4} and 10^{-3} inches. Thus, Eq. (3-28) is appropriate if it predicts a smaller value of r_n but not if it predicts a larger value.

It is not clear that r_n is similarly bounded by 10^{-4} - 10^{-3} inches for wicked surfaces; but it is certainly bounded by the pore size of the wick (r_e in Eq. (3-4)). Thus, a conservative approach to establishing

*A potential nucleation site is a cavity which contains a pre-existing gaseous phase.

the critical superheat for nucleation is to use Eq. (3-28) for r_n as long as it predicts a value below the effective wick pore radius - r_e , and to use r_e otherwise.

This approach is actually very conservative for conventional heat pipe design, for it presumes the existence of nucleation sites containing a pre-existing gaseous phase. In the absence of such conditions, very much higher superheats are required for nucleation than those predicted by Eqs. (3-27) and (3-28). Thus, since a conventional heat pipe is very carefully processed to eliminate all foreign gases, one seldom observes nucleation at the superheat levels predicted in this way. For example, using ammonia as the working fluid with an operating temperature of 70°F, TRW has measured nucleation superheats of 7°F, compared with a maximum predicted value of 0.4°F (Eq. (3-27) with $r_n = 10^{-4}$ in.) [G7].

On the other hand, this program is primarily concerned with variable conductance heat pipes, in which control is frequently effected through the use of non-condensable gases. Under such circumstances, gases are abundantly present to promote nucleation and Eqs. (3-27) and (3-28) will apply. They are similarly applicable in cases where a non-condensable gas charge is introduced to aid start-up from a frozen state [G7, G8].

3.2.1.2 Maximum Heat Flux

The nucleation superheat predicted by Eqs. (3-27) and (3-28) represents the maximum temperature differential which can be sustained across the evaporator wick without nucleate boiling within the wick. The consequences of wick boiling depend on the nature of the wick used. In certain composite wicks, such as annular arteries or screen-covered grooves (to be discussed later), wick boiling clearly renders the heat pipe inoperative since the vapor cannot escape the wick. On the other hand, if the wick structure does permit the escape of vapor (e.g., a feltmetal wick, a packed bed wick), operation with boiling can be sustained.

In cases where the incipience of boiling represents heat pipe failure, heat must be conducted to the wick surface and the liquid vaporized there. Under these circumstances, the maximum pipe heat transfer (Boiling Limit) corresponds to the conduction heat flux into the evaporator which yields a wick temperature drop equal to ΔT_{crit} from Eq. (3-27). For cylindrical heat pipes such as that in Fig. 3-1, this is given by:

$$Q_{BL} = \frac{2\pi L_e k_{eff} \Delta T_{crit}}{\ln \frac{R_w}{R_v}} \quad (3-29)$$

where:

- Q_{BL} - boiling limit on pipe heat transport
- L_e - length of evaporator section
- ΔT_{crit} - nucleation superheat (Eq. 3-27)
- k_{eff} - effective thermal conductivity of saturated wick

For certain well defined wick structures the effective thermal conductivity of the saturated wick can be analytically calculated. However, as with the effective pore size (r_e), and permeability (K) of wicking materials, this must often be a measured quantity. Several investigators have dealt with this problem analytically and experimentally [T2, T3, T4], and a number of correlations exist for certain classes of wicks. However, considering the countless combinations of wick structures and fluids available, these correlations are of very limited usefulness.

Neglecting convection effects, it is relatively simple to show that the effective thermal conductivity of any saturated wick is bracketed by assuming either parallel or series conduction paths and weighting the solid and liquid conductivities on a void fraction basis. Thus:

$$\frac{k_s k_l}{\phi k_s + (1 - \phi) k_l} \leq k_{eff} \leq (1 - \phi) k_s + \phi k_l \quad (3-30)$$

(series) (parallel)

Unfortunately, for the metallic wicks and non-metallic working fluids typical of spacecraft thermal control heat pipes, the bounds on k_{eff} given by Eq. (3-30) are very broad. If the wick design is such that nucleation represents heat pipe failure, conservative heat pipe design generally dictates that the lower bound (series case) be used. Thus, for conduction heat transfer, k_{eff} in Eq. (3-29) should be determined analytically, experimentally, or by correlation if possible; and if not, by the lower bound of Eq. (3-30).

In cases where the wick structure permits operation with internal vapor generation, the problem becomes much more complex. Under these circumstances, much higher evaporator heat fluxes can be tolerated than those predicted by Eq. (3-29) for conduction heat transfer. Still, there exists a maximum heat flux corresponding to the condition where vapor is generated within the wick at such a high rate that it cannot escape and forms an insulating layer which blankets the heat pipe wall. Although this failure mode is similar to the critical heat flux condition in pool boiling, it cannot be predicted using the pool boiling equations, for the presence of the wick alters both the vapor and liquid hydrodynamics.

Numerous investigators have studied the wick boiling phenomenon [G1, G3, H4, H11, H12, T5, T6, T7, T8, T9], and although there is still some controversy as to the phenomena involved, a theory is beginning to emerge for certain cases. For wicks with a pore size distribution (e.g., metal felt, sintered particles), the proposed mechanism is that once nucleation begins the liquid recedes into the wick such that, over the bulk of the evaporator wall, heat is conducted through a thin micro-layer of liquid. The thickness of the liquid layer is hypothesized to be independent of the wick thickness but rather on the order of the fiber or particle size making up the wick. Thus, the theory suggests that, even with vapor generation internal to the wick, the heat transfer is by conduction through a fairly well defined liquid layer, and that the ebullition-induced mechanisms which characterize nucleate boiling are not significant. Such a model predicts a constant coefficient of

heat transfer for the "boiling" mode. This has been experimentally observed by Ferrel, et al [T9, T10] using packed sphere bed wicks, and also by workers at TRW using sintered particle wicks.

The maximum heat flux consistent with this model occurs when the pressure drop associated with vapor escape through the wick exceeds the ability of the available capillary forces to maintain the liquid film. Thus, the maximum heat flux is a function of the wick thickness whereas the coefficient of heat transfer is not. With this model Ferrel, et al [T9, T10] have been able to approximately predict maximum heat fluxes for packed sphere bed wicks.

Note that the theory described is limited to wicks with a pore size distribution and, in fact, has been seriously tested only for packed sphere bed wicks. Substantially different behavior has been observed for other wick types such as rolled screens [T8].

For a detailed discussion of wick boiling the reader is referred to the referenced literature. It is considered beyond the scope of this program--primarily because satisfactory predictive methods (either analytical or by correlation) do not yet exist. Furthermore, if a heat pipe operates with vapor generation internal to the wick, the hydrodynamic theory presented in Section 3.1 is no longer applicable. That theory is based upon laminar flow through fully saturated wicks. Liquid recession into the wick or vapor bubbles present within the wick will significantly alter the liquid flow in an as yet unpredictable way. Consequently, although it is certainly possible to operate heat pipes with wick boiling, it is not yet possible to predict their performance except by empirical means.

The application of heat pipes to spacecraft thermal control generally requires a predictive design capability, and thus it is recommended that such heat pipes be designed to avoid boiling altogether. This can be done using the nucleation criteria presented in the last section to

establish the maximum evaporator heat flux. Methods of achieving high radial heat fluxes without incurring nucleation will be discussed later in this report.

3.2.2 Condenser Heat Transfer

The heat transfer process at the condenser section of a heat pipe is a much simpler phenomenon than at the evaporator. Vapor is condensed at the wick surface and the latent heat of vaporization released is generally conducted through the wick to the pipe wall.* However, in this case, the conduction temperature drop results in subcooling of the liquid which is a stable situation. The condenser heat transfer is thus described by an equation similar to Eq. (3-29), but with no practical heat transfer limit on ΔT or Q .**

As with the evaporator case, techniques available for minimizing the condenser temperature drop will be discussed later in this report.

*Exceptions to this do exist, such as grooved wall condensers where the pipe wall is the wick.

**The limit on Q due to condenser flooding is actually a hydrodynamic limit, and that imposed by the kinetic rate of vapor arrival is so high that it can safely be neglected (except for some liquid metal pipes).

4.0 CONVENTIONAL HEAT PIPE DESIGN

The previous discussion dealt with the theory of conventional heat pipes from the hydrodynamic and heat transfer points of view. The theory of variable conductance heat pipes will be taken up in Research Report No. 2. This section deals with the application of the hydrodynamic and heat transfer theory to the design of heat pipes with reference to wick design, fluid selection, materials selection and heat pipe optimization.

In all but the simplest geometries, closed form solutions to the differential flow equations summarized in Section 3.1.5 are not available. Consequently, proper heat pipe design technique generally involves numerical analysis. All heat pipe design at TRW is accomplished with one of several digital computer programs which integrate the differential forms of the equations for the appropriate boundary conditions. These programs are outside the scope of this contract and will not be discussed here.

To illustrate the points to be made regarding the various design parameters, the closed form solution for the special case shown in Fig. 3-1 will be used as an example. This system consists of a tube with single evaporator and condenser sections at the ends of the pipe, with or without an intervening adiabatic section. The pipe geometry is assumed axially uniform as is the heat input and rejection.

4.1 Wick Design

The primary purpose of the heat pipe wick is to provide a capillary flow mechanism for liquid circulation. As such, it is clear from Eq. (4-1) that a "good" wick is one which generates a high capillary head while offering a minimal resistance to liquid flow. Furthermore, as discussed in Section 3.2, it is frequently the case that heat must be transferred through the saturated wick in both the evaporator and condenser sections. Thus, a "good" wick is also one which provides for this heat transfer with a minimum temperature drop.

4.1.1 Effective Pore Radii of Various Wicks

It was shown in Section 3.1.1 that the maximum capillary head is given by:

$$\Delta P_{\text{cmax}} = \frac{2\sigma \cos \psi}{r_{\text{eA}}} \quad (\text{Class A wicks}) \quad (3-4a)$$

$$\Delta P_{\text{cmax}} = \frac{2\sigma}{r_{\text{eB}}} \quad (\text{Class B wicks}) \quad (3-4b)$$

Thus, to maximize this quantity for a given fluid and material, one must minimize the effective pore radius r_{eA} or r_{eB} .

For certain well defined pore geometries, the effective pore radius can be determined analytically. Several examples, neglecting body force effects, are presented below.

Cylindrical holes:

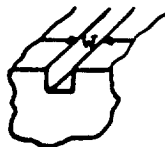


The isolated cylinder is the class A case for which Eq. (3-4a) was derived. Thus:

$$r_{\text{eA}} = r_p \quad \text{where } r_p \text{ is the actual pore radius.} \quad (4-1)$$

Most wicks do not exhibit ideal cylindrical pores. However, one wick which approaches this--called the "parallel capillary channel" wick--has recently been developed [G9].

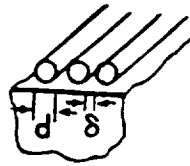
Rectangular grooves:



A popular wick geometry consists of axial grooves cut into the heat pipe wall. This is also a class A wick in that the lands between grooves separate adjacent menisci. As long as the groove depth is greater than half the groove width:

$$r_{eA} = w \quad \text{where } w \text{ is the groove width.} \quad (4-2)$$

Parallel wires:



An interesting wick structure, first reported by Sweeney [H13], consists of a series of parallel wires spaced a given distance apart. This is similar to axial grooves but provides a re-entrant flow cavity. Thus, the ratio of capillary head to flow resistance will be higher than for the rectangular groove. This case will be developed in more detail to show the analytical method involved.

Using the model shown in Fig. 4-1, it is readily shown through a little geometry that the meniscus radius of curvature - R can be expressed in terms of the other variables as follows:

$$R = \frac{\frac{\delta}{2} + \frac{d}{2} (1 - \cos \beta)}{\cos (\beta - \psi)} \quad (4-3)$$

where:

- d - wire diameter
- δ - wire spacing
- R - meniscus radius of curvature
- ψ - wetting angle
- β - position in degrees around wire where liquid-vapor-solid contact exists

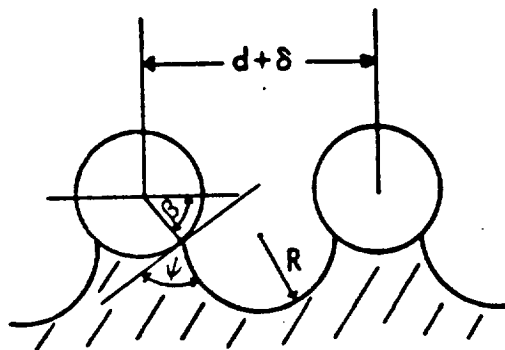


FIGURE 4-1. Capillary Model for Parallel Wire Wick

Assuming a class A wick and solving Eq. (3-4a) for r_{eA} by substituting Eq. (3-2) for ΔP_{cmax} , one sees that:

$$r_{eA} = \frac{2\cos\psi}{\left(\frac{1}{R_1} + \frac{1}{R_2}\right)_{\max}} \quad (4-4)$$

For parallel wires (or axial grooves, etc.), one of the meniscus radii of curvature is infinite. Thus, Eq. (4-2) can be reduced to:

$$r_{eA} = 2\cos\psi R_{\min} \quad (4-5)$$

where R_{\min} is the minimum possible value for the meniscus curvature. For parallel wires R_{\min} is the minimum value of R as given by Eq. (4-3).

Considering Eq. (4-3), it is immediately apparent that for zero wetting angle ($\psi = 0$), the minimum value of R is simply $\frac{\delta}{2}$, corresponding to $\beta = 0$. Thus, for $\psi = 0$, the effective pore radius is simply $r_{eA} = \delta$, which is similar to the result for straight-walled grooves. However, it is also apparent from Eq. (4-3) that this result does not hold for wetting angles other than zero. For this geometry it is possible for the meniscus to "roll around" the wire, altering the "effective" wire spacing. Thus, to solve the general case one must minimize Eq. (4-3) with respect to the angle β . Note that if a minimum exists in R for $\beta < 90^\circ$ the maximum capillary head is determined by a minimum free energy condition and we indeed do have a class A wick. If no minimum exists for $\beta < 90^\circ$ the meniscus will recede until adjacent menisci coalesce and we have a class B wick.

Differentiating Eq. (4-3) with respect to β , and setting $\partial R / \partial \beta$ equal to zero, one finds after a little algebra that the minimum R occurs when β satisfies the following equation:

$$\sin(\psi - \beta) = \frac{\sin\psi}{1 + \frac{\delta}{d}} \quad (4-6)$$

Since for wetting fluids $0 \leq \psi \leq 90^\circ$, the right hand side of Eq. (4-6) is a positive number less than unity.

This, and the upper bound on ψ , limit the quantity $\psi - \beta$ to the first quadrant. Thus, the value of β at which R reaches a minimum is always equal to or less than ψ and is therefore $\leq 90^\circ$; i.e., this is a class A wick.

We also see from Eq. (4-6) that the critical value of β is not generally zero, but varies with the wetting angle and the ratio δ/d . To determine r_{eA} , one must specify d , δ and ψ , solve Eq. (4-6) for β , solve Eq. (4-3) for R_{\min} , and then determine r_{eA} from Eq. (4-5).

Fig. 4-2 shows the results of such computations for the general cases where $\delta = d$ and $\delta = 2d$. The effective pore radius is expressed in terms of the wire spacing: $r_{eA} = f\delta$, and the graph shows the variation in the factor f with the wetting angle.

As opposed to straight-walled grooves where the factor f is always unity, the parallel wire wick exhibits a decreasing value of f with increasing wetting angle. In other words, the ability of the meniscus to "roll around" the wires decreases the sensitivity of ΔP_{\max} to the wetting angle.

Screen Mesh:

One of the most commonly used heat pipe wick materials is woven wire mesh. Although its popularity is in part due to precedent, it does offer certain features such as (1) a wide selection of readily available pore sizes, (2) ease of fabrication--especially of composite wick structures, and (3) low cost.

Wire mesh wicks are actually very complex and difficult to characterize. Their properties vary widely depending on whether single or multiple layers are used, how tightly adjacent layers contact each other,

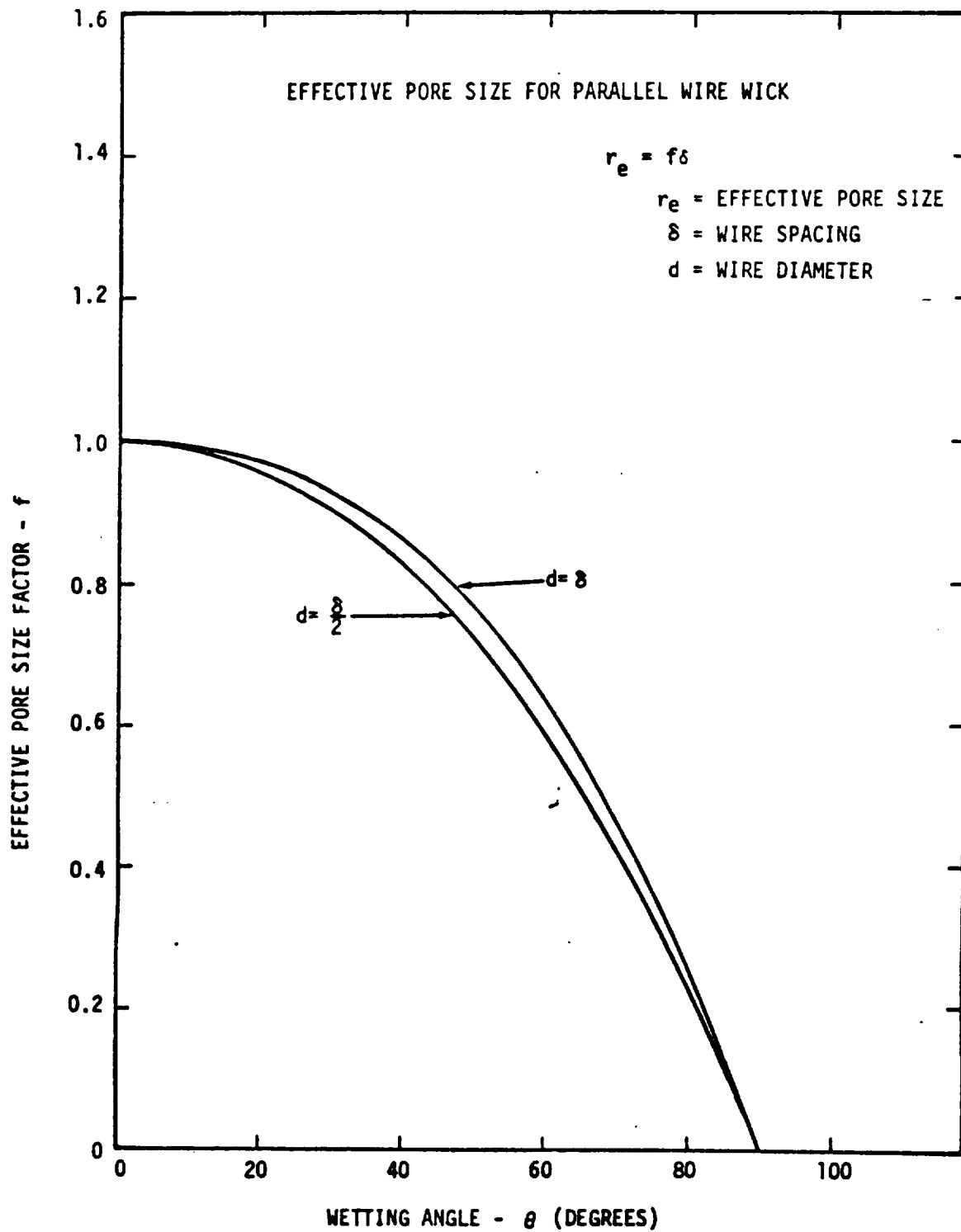


FIGURE 4-2. Effective Pore Size for Parallel Wire Wick

whether or not the evaporator end of the wick is sealed, etc. It will be assumed in this discussion that the wick layers are in close enough contact or that the evaporator end is sealed such that capillary pumping is limited by the mesh pores rather than the gaps between layers.

It might at first appear that a screen wick is similar to the parallel wire case just discussed. This, however, is not true by virtue of the multiple vs. single curvatures of the respective menisci. The meniscus formed in a screen pore is not a segment of a sphere but a complex geometry of varying curvature. To this author's knowledge, nobody has yet analytically studied the interfacial free energy of a screen pore meniscus to establish whether or not a minimum exists prior to coalescence of adjacent menisci. That is, it has not been analytically demonstrated whether screens represent a class A or class B wick.

Assuming a square mesh screen is a class B wick, Tien and Sun [H3] have shown that for single layers, the effective pore radius is given by:

$$r_{eB} = \frac{d + \delta}{2} \quad (4-7)$$

This formulation, which is independent of wetting angle, has successfully correlated the data of a number of investigators.

For multiple screen layers, Eq. (4-7) is no longer valid because of intermeshing between adjacent layers. No general correlation has been put forth for this case, but experience of several laboratories have shown that, in almost all cases,

$$\frac{\delta}{4} < r_e < \frac{\delta}{2} \quad (4-8)$$

Eq. (4-8) does not specify whether multi-layer screens represent class A or class B wicks. Insufficient data using multiple fluids with the same wick are available to reliably determine whether or not there exists a contact angle effect, and the uncertainty in the actual pore geometry

does not permit establishing whether measured capillary pressures correspond to minimum free energy menisci or menisci coalescence.

Because of the uncertainty in pore geometry of multi-layer screen wicks, and an observed irreproducibility depending on the degree of inter-meshing, one should design these wicks conservatively. Thus, for single layer or loosely layered screen wicks, Eq. (4-7) is appropriate. For tightly wrapped multi-layer wicks, the upper bound of Eq. (4-8), assuming a class B wick ($r_{eB} = \frac{\delta}{2}$), will yield a conservative design.

Packed Sphere Beds, Metal Felts, Woven Cloths, etc.:

As with multi-layer screens, it has not yet been established whether materials in this category fall into class A or class B, or whether they vary depending on their microgeometry. This will have to await further study. However, from a design point of view, all of these materials exhibit behavior similar to the parallel wire wick in that, if they do suffer a class A limit, their dependence on wetting angle is much reduced by the ability of the menisci to "roll around" the fibers or particles. This, in addition to the fact that most fluid-material combinations exhibit very low wetting angles, allows the designer to neglect wetting angle effects and use Eq. (3-4b) for ΔP_{cmax} .

As opposed to cylindrical pores, grooves, single screen layers and parallel wires, materials of this type will have a distribution of pore sizes. Under such circumstances, the effective pore size varies with the level of wick saturation (the largest pores desaturate first). For cases where initial desaturation corresponds to heat pipe failure (e.g., a uniform wicked pipe with no boiling or body forces), the effective pore size is determined by the largest pores available. Under these circumstances, the literature [H3, T10, G10] suggests that:

For randomly packed sphere beds (a good approximation to sintered particle wicks):

$$r_{eB} = 0.41 r_s \quad (4-9)$$

where r_s is the sphere radii.

For fibrous wicks (e.g., metal felt):

$$r_{eB} = \frac{d + (32 K/\phi)^{1/2}}{2} \quad (4-10)$$

where:

d is the fiber diameter

K is the permeability

Using Eqs. (4-7) for single layer screens, (4-9) for packed sphere beds, and (4-10) for metal felts, in conjunction with Eq. (3-4b) for ΔP_{cmax} in class B wicks, Tien and Sun [H3], have been able to correlate the data of numerous investigators on a single curve.

To summarize this discussion, it appears that there are two (at least) phenomena which give rise to a limit on pumping head, and thus which establish the effective pore size. One corresponds to the meniscus reaching a minimum free energy configuration (class A), and the other to the coalescence of adjacent menisci (class B). Wicks with isolated pores (e.g., parallel capillaries, grooves) are always of the class A type. Wicks with interconnecting pores may be either class A (parallel wires) or class B (single layer square mesh).

For well defined geometries it is often possible to analytically determine the failure mechanism and the effective pore size. For poorly defined geometries one must either empirically measure the appropriate effective pore size or, if available, use existing correlations.

Unfortunately, there exist very few correlations for r_e compared with the myriad of different wick materials and operating conditions (e.g., partial desaturation), and even those that exist are not as yet very well supported. Thus, measured wick property data is extremely

important to the heat pipe designer. A limited quantity of such data can be found in the open literature [H3, H4, H5, H11, H12, H14, T10, G3, G5, G11].

4.1.2 Permeability of Various Wicks

The permeability of a wick is an inverse measure of its flow resistance. Thus, a "good" wick has a high permeability.

As with the effective pore radius, it is possible to analytically determine the permeability of well defined capillary structures. The approach is to write an expression for the liquid pressure gradient-- dP_l/dz and equate it to Eq. (3-6) in order to solve for the permeability - K. Several examples follow for laminar flow.

Parallel Cylindrical Capillaries:

The pressure gradient for Poiseuille flow in a wick made up of cylindrical capillaries is given by:

$$\frac{dP_l}{dz} = \frac{8\mu_l \dot{m}_l(z)}{A_{pl} \phi r_p^2} \quad (4-11)$$

Equation (4-11), when combined with Eq. (3-6) yields:

$$K = \frac{\phi r_p^2}{8} \quad (4-12)$$

Axial Grooves, Parallel Wires, etc.:

Capillary structures consisting of grooves cut into the heat pipe wall or parallel wires laid against the wall can all be treated as a series of straight flow channels of various cross-section. Laminar flow solutions have been obtained for a large variety of flow cross-section shapes. These can all be reduced to a form similar to that for cylindrical channels which will yield approximate values for the liquid pressure gradient. Thus:

$$\frac{dP_L}{dz} = \frac{8\mu_L \dot{m}_L(z)}{A_{\phi} \phi r_h^2} \cdot S \quad (4-13)$$

where S is a shape factor dependent on the particular cross-sectional geometry, and r_h is the hydraulic radius, given by:*

$$r_h = \frac{2 \text{ (flow area)}}{\text{(wetted perimeter)}} = \frac{2A_F}{P_w} \quad (4-14)$$

Values of the shape factor - S can be obtained from the literature for shapes whose laminar flow solutions are available [G12]. Typical values for heat pipe wicks range between 0.6 - 1.4. In the absence of a solution for a geometry similar to that of interest, one might simply use that for a circular duct; $S = 1.0$.

In Eq. (4-13) the product A_{ϕ} is simply the total wick cross-sectional flow area, equal to the number of grooves (channels, etc.) multiplied by the flow area per groove. Unless the groove depth is large compared with its width, the curvature of the meniscus must be accounted for in computing A_F . Equation (4-13), when combined with Eq. (3-6) yields:

$$K = \frac{\phi r_h^2}{8S} \quad (4-15)$$

Packed Sphere Beds (sintered particles):

The permeability of randomly packed sphere beds in the laminar flow regime is fairly well predicted by the Blake-Kozeny equation [G13]:

$$K = \frac{D_s^2 \phi^3}{150 (1 - \phi)^2} \quad (4-16)$$

*The use of the hydraulic radius for the characteristic dimension in Eq. (4-13) is somewhat arbitrary. The concept of the hydraulic radius is most useful in turbulent flow where it has been empirically demonstrated that it generally leads to a shape factor - S near unity. This is not true for laminar flow, as found in most heat pipes. However, using r_h is consistent with common practice, and in the absence of appropriate values for S , yields engineering estimates with $S = 1$.

where: D_s is the sphere diameter.

Metal Felts, Woven Cloths, etc.:

Wicks of this nature are difficult to treat analytically or by correlation. Tien and Sun [H3] argue that the permeability, porosity and effective pore diameter (for flow) are related in such materials as follows:

$$K = \frac{D_e^2 \phi}{32} \quad (4-17)$$

They also suggest that the effective pore size for flow is simply related to the effective pore size for capillary pumping (substituting D_e for $(32K/\phi)^{1/2}$ in Eq. (4-10). However, this assumes a class B wick, and even at that, has yet to be substantiated to any degree.

Thus, once again, measured wick property data are required to effectively design heat pipes with this type of wick. As with the effective pore size radius, a limited quantity of such data can be found in the open literature [H4, H5, H11, H12, T10, G3, G11].

Screen Mesh:

As mentioned earlier, the properties of screen mesh wicks vary widely depending on the degree of intermeshing between adjacent layers, etc. However, it is the case that loosely wrapped screen wicks have lower flow resistance than tightly wrapped or sintered wicks. Thus, using results for tightly wrapped wicks provides a conservative design approach.

Schmidt [G11] has presented a correlation for the pressure drop in wire mesh wicks based on experimental data for screens of 45 through 270 mesh. He was able to correlate all of his low Reynolds number data ($Re < 15$) with a modified form of the Blake-Kozeny equation as follows:

$$\frac{dP}{dz} = - \frac{\rho \ell v_o^2}{D_p} \frac{(1 - \phi)}{\phi^3} \left(\frac{275}{Re} + 3.1 \right) \quad (4-18)$$

where the Reynolds number is defined as:

$$R_e = \frac{D_p v_o \rho \ell}{\mu \ell} \left(\frac{1}{1 - \phi} \right) \quad (4-19)$$

and:

- v_o - average liquid velocity
 D_p - 1.5 times screen wire diameter

Equation (4-18) can be considerably simplified at little cost in accuracy if one drops the constant 3.1 as insignificant compared with $275/R_e$ for small R_e . With this assumption Eq. (4-18) can be equated with Darcy's Law for dp_ℓ/dz (Eq. (3-6)) to yield:

$$K = \frac{d^2}{122} \frac{\phi^3}{(1 - \phi)^2} \quad (4-20)$$

where d is the screen wire diameter. Also, an expression for the porosity of wire mesh wicks may easily be derived from the geometry of screens (neglecting intermeshing):

$$\phi = 1 - \frac{\pi F M d}{4} \quad (4-21)$$

where:

- M - wires per inch
 F - crimping factor* (≈ 1.05)

Note that Eq. (4-20) is now identical to the Blake-Kozeny expression for permeability of packed beds (Eq. (4-16)) except for the empirical constant.

Equations (4-20) and (4-21) have been fairly successful at correlating data on screen wicks. Fig. 4-3 shows the data of several investigators compared with the predicted curve. The large quantity of data by

*The crimping factor accounts for the fact that screens are not simply crossed rods.

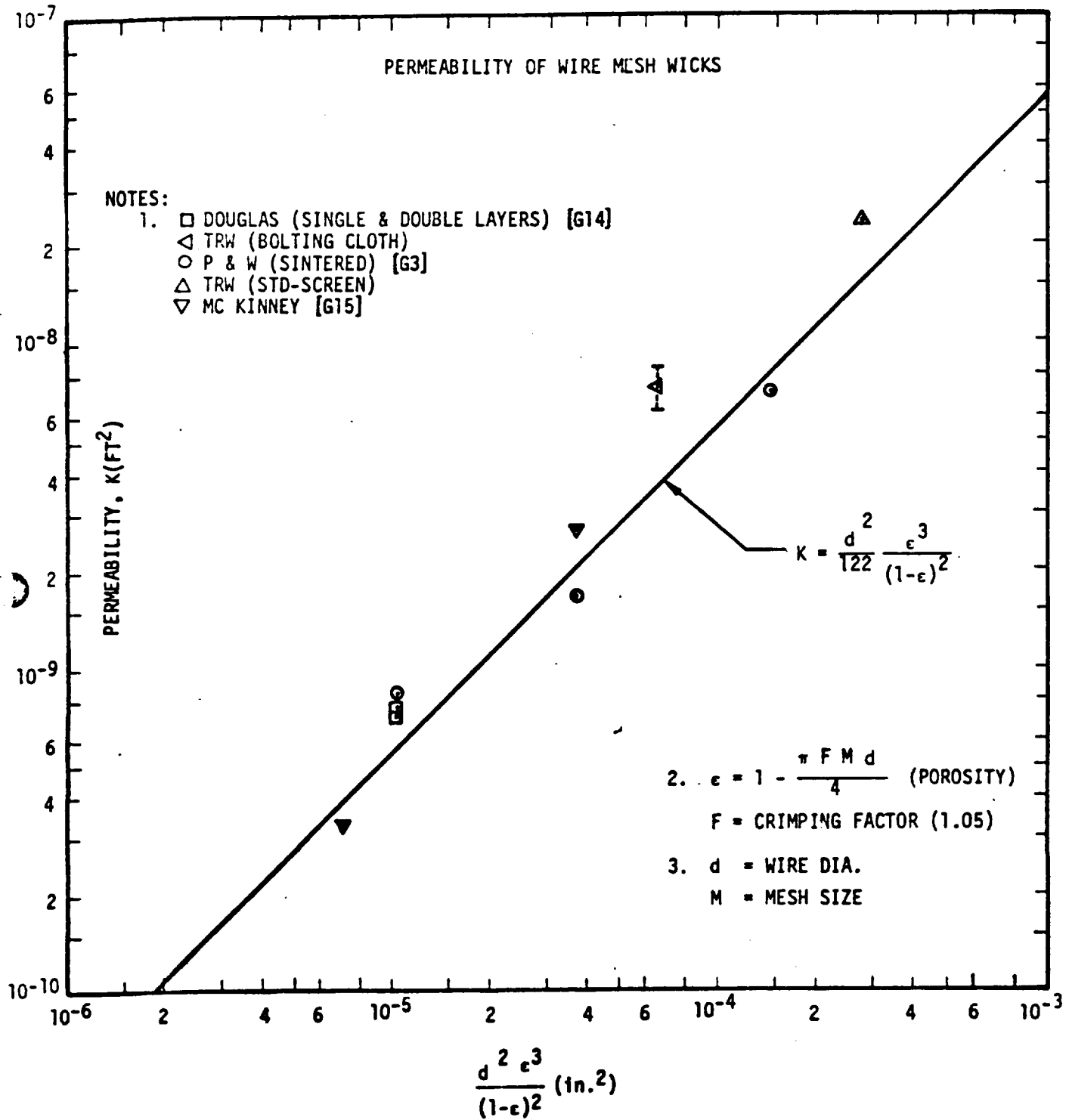


FIGURE 4-3. Permeability of Wire Mesh Wicks

Schmidt [G11] from which the equations were derived, and thus successfully correlate, is not shown.

4.1.3 Wick Optimization

It is always a desirable goal to design and build optimized heat pipes. Consequently, the heat pipe literature is full of heat pipe optimization analyses. Unfortunately, many of these analyses are not really pertinent--and some are actually incorrect. The basic difficulty here is in establishing the appropriate basis on which to perform the optimization. Depending on the application, the optimum heat pipe may be based on maximum hydrodynamic capacity, minimum temperature drop, minimum weight, minimum cost, maximum reliability, maximum life, maximum conductance ratio (for variable conductance pipes), etc. In practice, in designing a heat pipe for a particular application one must consider all of these criteria, weighted according to their relative importance, and perform trade-offs between them to arrive at an overall optimum design. Unfortunate as it may be, this does not generally reduce to the simple task of differentiating a single equation with respect to a single variable and setting the derivative equal to zero.

Hydrodynamic Criterion:

Not only is a simple extremizing procedure frequently inappropriate, it is sometimes misleading. For example, the heat pipe optimizing procedure most commonly seen in the literature [H1, G4] involves a hydrodynamic optimization. A pressure balance is written for the fluid cycle and extremized with respect to "the" appropriate capillary dimension of the wick (pore size). In this way, a relationship is derived for the optimum pore (groove, etc.) size which, when substituted in the pressure balance, leads to an optimum liquid/vapor flow area ratio and hence an optimum heat pipe based on hydrodynamic capacity.

In the first place, the equations derived in this manner are frequently misused, for most wicks (e.g., screen mesh, felt metal, foam metal,

woven fibers, etc.) are not truly homogeneous and isotropic, and therefore are not characterized by a single dimension (e.g., pore size). In other words, the porosity and tortuosity factors, which are treated as constants in this extremizing procedure, are themselves generally functions of the pore size. This functionality must be, and seldom is, included in the pressure balance before it is extremized with respect to the pore size. This can lead to a substantially different result for the optimum pore size than that generally seen in the literature for isotropic wicks.

These points can readily be illustrated by treating the case of wire mesh wicks. The pressure balance equation for the heat pipe shown in Fig. 3-1 at the capillary pumping limit was given by Eq. (3-21).

$$\left. \begin{array}{l} \frac{2\sigma\cos\psi}{r_{eA}} \\ \frac{2\sigma}{r_{eB}} \end{array} \right\} = \Delta P_{\text{cmax}} = \frac{Q(L + L_a)\mu_l}{2\pi K_0 \ell \lambda (R_w^2 - R_v^2)} + \frac{4Q(L + L_a)\mu_v}{\pi \rho_v \lambda R_v^4} + \rho_l g [D_w \sin\theta + L \cos\theta] \quad (3-21)$$

The procedure in hydrodynamically optimizing the wick is first to maximize the heat transport rate - Q with respect to the wick micro-structure. For simplicity, we shall assume a zero degree wetting angle and the upper bound of Eq. (4-8) for r_e so that distinctions between class A and class B wicks disappear. Thus, the maximum capillary head is given by $\Delta P_{\text{cmax}} = 4\sigma/\delta$.

If one now substitutes Eq. (4-20) for K in Eq. (3-21), and Eq. (4-21) for ϕ in Eq. (4-20), the pressure balance equation can be re-written after some algebraic manipulation as follows:

$$\frac{4\sigma}{\delta} = \frac{Q(L + L_a)\mu_l}{2\pi\rho_l\lambda(R_w^2 - R_v^2)} \left\{ \frac{122\pi^2}{16} \frac{(FM)^2}{(1 - \frac{\pi FMd}{4})^3} \right\} + \frac{4Q(L + L_a)\mu_v}{\pi\rho_v\lambda R_v^4} + \rho_l g [D_w \sin\theta + L \cos\theta] \quad (4-22)$$

In extremizing with respect to the wick microstructure, many of the terms in Eq. (4-22) are constant. Thus, the equation can be simplified considerably by defining the following constant groupings:

$$A = \frac{(L+L_a)\mu_l}{2\pi\rho_l\lambda(R_w^2 - R_v^2)} \left(\frac{122\pi^2}{16} \right)$$

$$B = \frac{4\mu_v(L+L_a)}{\pi\rho_v\lambda R_v^4}$$

$$C = \rho_l g [D_w \sin\theta + L \cos\theta] \quad (4-23)$$

With these substitutions, and noting that $Md = 1 - M\delta$, Eq. (4-22) can be rearranged to yield:

$$Q = \frac{\frac{4\sigma}{\delta} - C}{\left[\frac{A(FM)^2}{(1 - \frac{\pi F}{4} + \frac{\pi FM\delta}{4})^3} + B \right]} \quad (4-24)$$

It is clear from Eq. (4-24) that the wick cannot be characterized by a single variable as is frequently assumed,* but depends on both M and δ (or d and δ since $Md = 1 - M\delta$). Thus, to properly optimize the wick, one must extremize Eq. (4-24) with respect to both of these variables to find the maximum Q in the three-dimensional (Q, M, δ) space. This extremizing procedure is algebraically very cumbersome and is best performed numerically.

*By assuming the porosity and tortuosity constant, the denominator is reduced to $\frac{A}{\delta^2} + B$.

The wick optimization procedure for screens is substantially simplified if it can be assumed that the vapor pressure loss - ΔP_v is small compared with the other terms in the pressure balance equation. Experience has shown that this is frequently the case in the design of thermal control heat pipes which must be tested in a 1-g field.

If ΔP_v is small enough so that its variation with Q can be neglected in comparison with that of ΔP_ℓ , it can be treated as a constant in Eq. (4-22). Then the constant grouping B in Eq. (4-23) can be modified to include Q :

$$B' = \frac{4Q\mu_v(L + L_a)}{\pi\rho_v\lambda R_v^4} \quad (4-25)$$

The equivalent form of Eq. (4-24) now becomes:

$$Q = \frac{\frac{4\sigma}{\delta} - B' - C}{\frac{A(FM)^2}{(1 - \frac{\pi F}{4} + \frac{\pi FM\delta}{4})^3}} \quad (4-26)$$

This equation is much easier to extremize algebraically. Differentiating with respect to δ and setting the result equal to zero yields an optimum screen wire spacing for fixed M :

$$\delta_{opt} = \frac{4\sigma}{3(B'+C)} + 4 \left[\frac{\sigma^2}{9(B'+C)^2} - \frac{(1 - \frac{\pi F}{4})}{3\pi FM(B'+C)} \right] \quad (4-27)$$

The wire spacing - δ_{opt} , as given by Eq. (4-27) yields a maximum value of Q for a given mesh. It is interesting to consider whether there similarly exists an optimum mesh size. Differentiating Eq. (4-26) with respect to M (holding δ constant) does yield an extremum, as follows:

$$M_{extremum} = \frac{8(1 - \frac{\pi F}{4})}{\pi F\delta} \quad (4-28)$$

However, if one examines the second derivative ($\partial^2 Q / \partial M^2$), one finds it is positive at this value of M . On the other hand, the second derivative with respect to δ ($\partial^2 Q / \partial \delta^2$) is negative at the extremum.

Thus, Eq. (4-28) does not yield an optimum value of M . Rather, the point in the (Q, δ, M) space defined by Eqs. (4-27) and (4-28) is a saddle point corresponding to a maximum in Q with respect to δ but a minimum in Q with respect to M .*

Examining Eq. (4-26) directly, in light of Eq. (4-27) for δ_{opt} , it can be shown that the required departure from the extremum of Eq. (4-28) is in the direction of increasing mesh size. One wants to use the highest mesh possible for a given wire spacing.

The design procedure for optimizing the wick thus reduces to the simultaneous solution of Eq. (4-27) which relates δ_{opt} to M and a table or graph of δ vs. M for available screen meshes. This procedure is shown on Fig. 4-4. The curve represents Eq. (4-27) showing a typical variation of δ_{opt} with M . The points on the graph represent δ, M couples for generally available screen mesh. The optimum wick corresponds to the screen of largest mesh size which falls on (or near) the curve.

Equation (4-27) for δ_{opt} was derived for the specific heat pipe shown in Fig. 3-1. However, it is easily generalized. If one replaces the constants $B' + C$ with ΔP_0 and includes a safety factor - S defined by:

$$\Delta P_{cmax} = S (\Delta P_l + \Delta P_v \pm \Delta P_b) \quad (4-29)$$

the equivalent form of Eq. (4-27) becomes:

*It is interesting to note that if Eq. (4-28) is substituted into Eq. (4-27), one finds that this saddle point corresponds to the condition where $\Delta P_l = \frac{1}{2} \Delta P_{cmax}$. This is the criteria suggested by Cotter [H1] for optimum wicks.

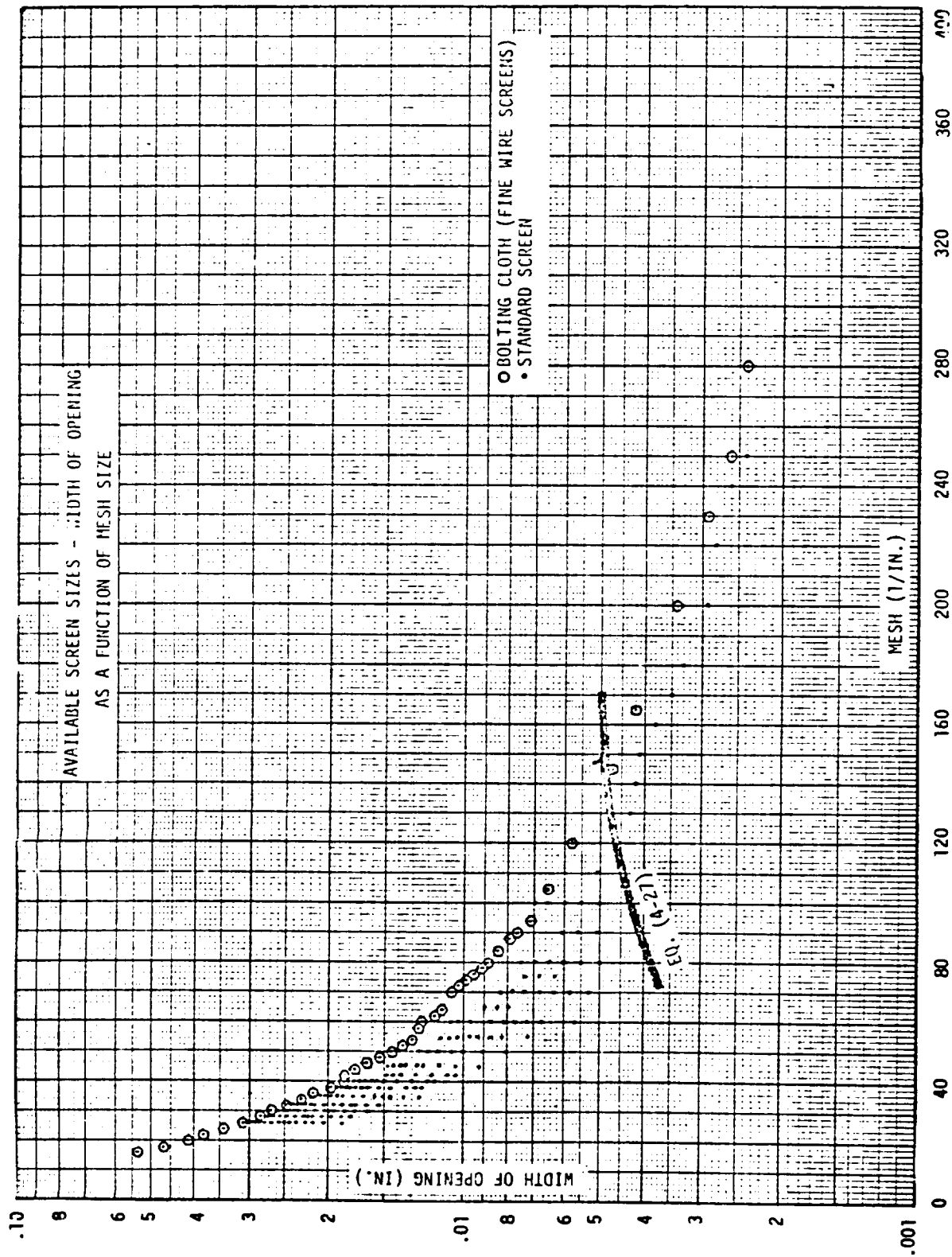


FIGURE 4-4. Wire Mesh Optimization Graph

$$\delta_{\text{opt}} = \frac{4\sigma}{3S\Delta P_0} + 4 \left[\frac{\sigma^2}{9S^2 \Delta P_0^2} - \frac{(1 - \frac{\pi F}{4})}{3\pi F S M \Delta P_0} \right] \quad (4-30)$$

Equation (4-30) now allows optimizing the wick for a desired safety factor, which should always be considered in heat pipe design. Furthermore, the term ΔP_0 now represents a generalized "loading" on the wick. In other words, the capillary head available for liquid pumping in the wick is given by:

$$\Delta P_{\ell \text{ avail}} = \frac{\Delta P_{\text{cmax}}}{S} - \Delta P_0 \quad (4-31)$$

Thus, Eq. (4-30) can also be used for heat pipes with axial variations in wicking (hybrid wicks - see Fig. 3-3e). For example, if a pipe had a different wick in the evaporator than in the adiabatic section and condenser, ΔP_0 would include the liquid pressure drop in the condenser and adiabatic section when optimizing the evaporator wick; i.e., $\Delta P_0 = \Delta P_v + \Delta P_b + (\Delta P_{\ell})_{\text{cond} + \text{adiab.}}$

Also, since Eq. (4-30) does not include specific wick dimensions, it can be used for wicks of any cross-sectional configuration; i.e., it is not limited to annular wicks as shown on Fig. 3-1.

Heat Transfer Criterion:

Even more important than avoiding the use of isotropic wick optimization procedures for non-isotropic wicks, one must exercise great care to assure that the optimization criterion used is the appropriate one.

For example, if one uses the appropriate procedure to obtain the optimum pore size, and then varies the wick thickness to alter the liquid/vapor flow area ratio, the resulting curve for maximum heat transfer vs. area ratio will appear as shown in Fig. 4-5a.

As seen in this figure, there will exist an optimum area ratio based on hydrodynamic considerations. For isotropic wicks under zero body force conditions, the vapor core should represent $2/3$ of the total flow area. However, this is a strong function of the body force field.

One must recognize, however, that the hydrodynamic optimum may well correspond to an evaporator input heat flux which far exceeds the conduction heat transfer limit (i.e., there must exist internal vapor generation). Under such conditions, the equations that led to this optimum, which are based on Darcy flow through fully saturated wicks, are no longer applicable and the entire analysis is invalid. The generally utilized heat pipe hydrodynamic equations are only valid for fully saturated wicks and thus, for operation below the conduction heat transfer limit in the evaporator (see Sec. 3.2.1.2).

Of course, this conduction heat transfer limit is also a function of wick thickness (Eq. (3-29)) and can thus be superimposed on Fig. 4-5a to yield Fig. 4-5b. The hydrodynamic limit curve, based on flow in fully saturated wicks, is only valid to the left of the intersection between the two curves. For liquid metals this intersection usually falls to the right of the extremum and the hydrodynamic optimum wick, determined in this way, is appropriate. However, for ordinary fluids, the curves generally intersect to the left of the extremum. If the wick design is one that cannot sustain internal vapor generation, the optimum pipe corresponds to the intersection of the two curves. On the other hand, if the wick can sustain internal vapor generation, the optimum pipe would fall to the right of this intersection but Q_{\max} will no longer be given by the hydrodynamic limit curve determined for saturated flow. Vapor generation within the wick will certainly impede liquid flow so that the actual hydrodynamic curve might appear as shown dotted in Fig. 4-5c. The actual shape of this curve cannot, at present, be determined by analytical means. This would require an ability to predict capillary flow in the presence of internal vapor generation. Although data for isolated cases and fluids are available, the results

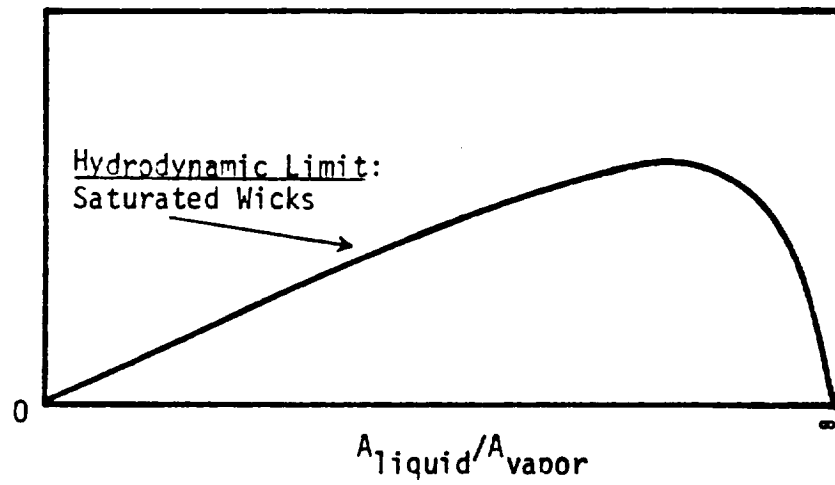
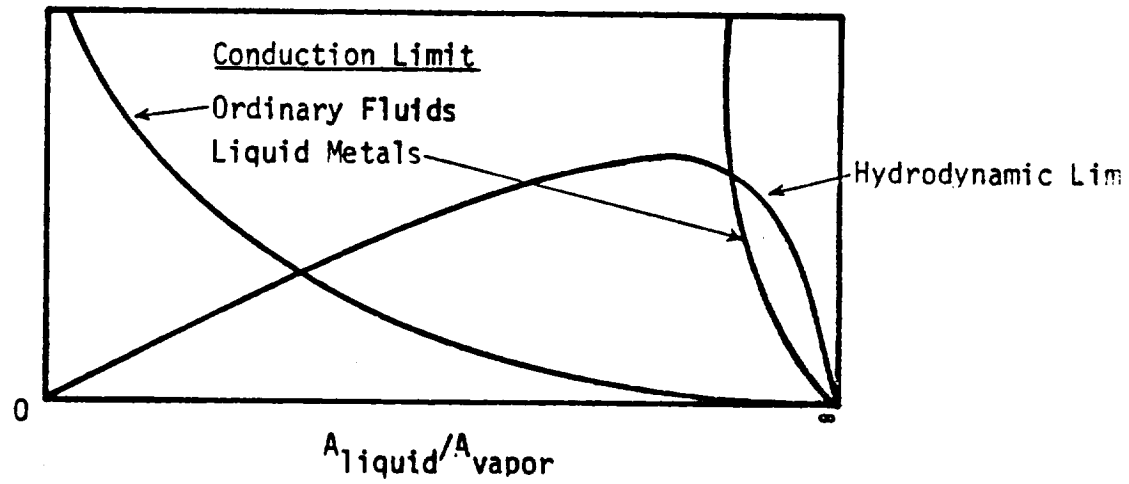
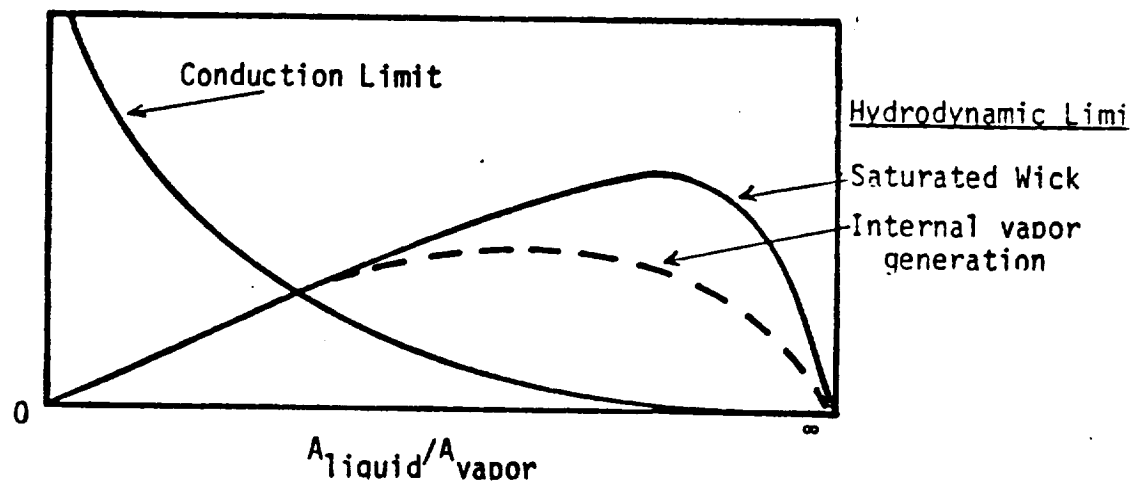
(a) Q_{\max} (b) Q_{\max} (c) Q_{\max} 

FIGURE 4-5. Heat Pipe Optimization

are not sufficient to enable the development of an empirical set of equations at this time.

The basic point to be gleaned from this discussion is that when optimizing heat pipes one must consider all pertinent phenomena and parameters. As seen, hydrodynamic optimization may violate heat transfer limits. It may also lead to heat pipes which are far from minimum weight, maximum conductance, etc. All such criteria must be considered in light of their relative importance when designing a heat pipe for a particular application.

4.1.4 Composite Wicks

It was seen in Sec. 4.1.1 that the maximum capillary head generated by a wick increases with decreasing pore size, which would suggest using wicks with small pores. On the other hand, it was seen in Sec. 4.1.2 that wick permeability increases with increasing pore size, which would suggest using wicks with large pores. Indeed, it is this diverse dependence on pore size which gives rise to an optimum pore size as discussed in Sec. 4.1.3.

A similar statement can be made regarding wick thickness. Increasing wick thickness decreases liquid flow resistance and thus raises heat pipe capacity. However, increasing wick thickness also increases the wick's thermal resistance and thus lowers heat pipe capacity by virtue of a lower maximum evaporator heat flux. This trade-off gives rise to an optimum wick thickness as discussed in Sec. 4.1.3.

Unfortunately, it is often the case that optimum heat pipes designed in this way are limited to low axial throughputs. This is especially true for spacecraft thermal control heat pipes which use relatively poor working fluids (compared with liquid metals). Furthermore, even for throughputs of only a few tens of watts, the temperature drop across the pipe can become excessive. Consequently, experience has shown that conventional designs with homogeneous wick-lined walls are inappropriate for high performance heat pipes.

The difficulty with such heat pipes arises because of the opposite dependence of key phenomena on the same variable. If the maximum capillary head and wick permeability were not dependent on the same (or related) pore size, it would be possible to make both large simultaneously. Similarly, if wick flow area and evaporator thermal resistance were not dependent on the same dimension, it would be possible to simultaneously increase the former and decrease the latter. In other words, one wants to de-couple capillary pumping from flow resistance in the wick, and axial wick hydrodynamics from radial heat transfer in the pipe. This has given rise to heat pipes with composite wicks.

Figure 4-6 shows four composite capillary structures which have been used in heat pipes to effect the de-coupling discussed above.

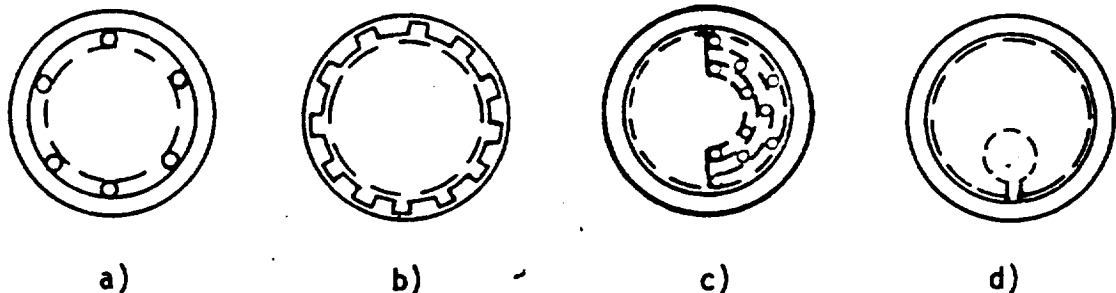


FIGURE 4-6. Composite Wick Heat Pipes

Configuration (a) represents a concentric annular artery formed by spacing a capillary surface (screen or otherwise) away from the tube wall with wires. In this way, a low axial flow resistance (high permeability) is obtained, corresponding to the resistance of the annular gap, while simultaneously achieving a high capillary pumping head representative of the pore size of the capillary surface. Thus, by departing from a homogeneous wick it is possible to de-couple the capillary head and wick permeability.

It should be noted that in this, and all other arterial wick structures, the local maximum capillary head is determined by the largest available pore or opening. Consequently, it is necessary that the capillary surface be sealed at the evaporator end and along its length to prevent any openings or holes that are larger than the pores of the wick material. The condenser end can be left open in cases where there doesn't exist any liquid-vapor pressure differential at that point (see Sec. 3.1.6).

The fact that the artery is sealed makes it particularly susceptible to internal boiling. If vapor is generated within an artery, its path of least resistance is to expand along the artery and cause it to empty of liquid. This, of course, eliminates the heat pipe's liquid pumping capability. Thus, great care must be exercised in design to assure that vapor does not form within or penetrate the artery.

This points up a drawback in the arterial design of configuration (a), for the heat must pass through the artery to reach the vapor-liquid interface for evaporation. Thus, the artery gap thickness is limited to that which causes a temperature drop sufficient to cause nucleation of vapor bubbles at the evaporator wall (within the artery). In other words, the axial hydrodynamics and radial heat transfer are still coupled through the wick thickness.

This situation is improved somewhat with configuration (b) which represents an axially grooved heat pipe wall with a cover layer of screen mesh or some other fine-pored material. Again, a low resistance axial flow path is provided by the grooves while the fine-pored cover provides a high capillary head. This system is less sensitive to the nucleation problem because almost all of the radial heat transfer is shunted through the metallic lands between the grooves and thus the superheat at the base of the grooves is not much higher than that at the groove-wick interface. There still will exist some liquid superheat in the grooves, the minimum corresponding to the temperature drop through the liquid-saturated wick covering both the grooves and lands. However,

this is rather insensitive to the grooves' depth and hence this wick structure does tend to de-couple the heat transfer (through the lands) from the hydrodynamics (through the grooves).

A deficiency of the grooved wall design is that one achieves large liquid flow areas at the expense of increased wall thickness, which can result in heavy heat pipes. Another geometry which accomplishes a similar heat transfer-hydrodynamic de-coupling with thin walled pipes is shown as configuration (c). In this case a thin wick lines the entire tube wall and a partial annular artery (or series of them) is placed asymmetrically along a portion of the wall. In this system, the portion of the pipe with the thin wick is utilized for heat transfer while the opposite side is used for fluid flow. This configuration permits considerable latitude in liquid flow area without altering the pipe wall or the heat transfer path. Also, it allows for high perpendicular body force fields such as might be found on spinning spacecraft. The thin wick need only be sufficient to handle the circumferential flow to and from the artery. This allows for minimum heat conduction paths and hence small input and output temperature drops.

Configuration (d) represents a pedestal-type internal artery (or arteries) with a thin wick lining the tube wall. As with configurations (b) and (c), this geometry de-couples the heat transfer (through the thin wick) from the axial hydrodynamics (through the artery). However, a major advantage of this geometry is that the artery is removed from the heat input zone. Since the artery is surrounded by vapor, the fluid within it can be no hotter than saturation temperature. Consequently, since there exists no arterial superheat, there can be no arterial nucleation. Thus, a serious failure mode of arterial heat pipes is eliminated. One must only assure that no vapor generated at the wall penetrates the artery. For ordinary fluids this can readily be done by providing a very fine-pored wick layer to serve as a vapor barrier between the artery and the wall wick.

For moderate evaporator heat fluxes with ordinary fluids in conventional heat pipes, the circumferential wick in configurations (c) and (d) can usually be made thin enough to avoid nucleation, and with it the problem of controlling the vapor formed. However, in the case of variable conductance heat pipes which involve non-condensable gases, the superheat tolerance of the working fluids is much reduced (see Sec. 3.2.1.1). Under such circumstances it appears best to utilize a capillary structure for circumferential pumping which assures a non-boiling, surface evaporation heat transfer mode.

Very impressive results have been obtained along these lines [G6, G11] by replacing the wick lining the tube wall with a series of closely spaced circumferential grooves in the wall (actually, the wall can be internally threaded). Radial heat transfer in this case is almost exclusively through the metal lands between grooves. Conduction through the liquid is only through a very thin layer at the sides of the menisci (Fig. 4-7). In this way, the input temperature drop can be reduced to such small values that nucleation can generally be avoided even in the presence of non-condensable gases. Of course, the output temperature drop is similarly reduced, yielding a very high conductance heat pipe.

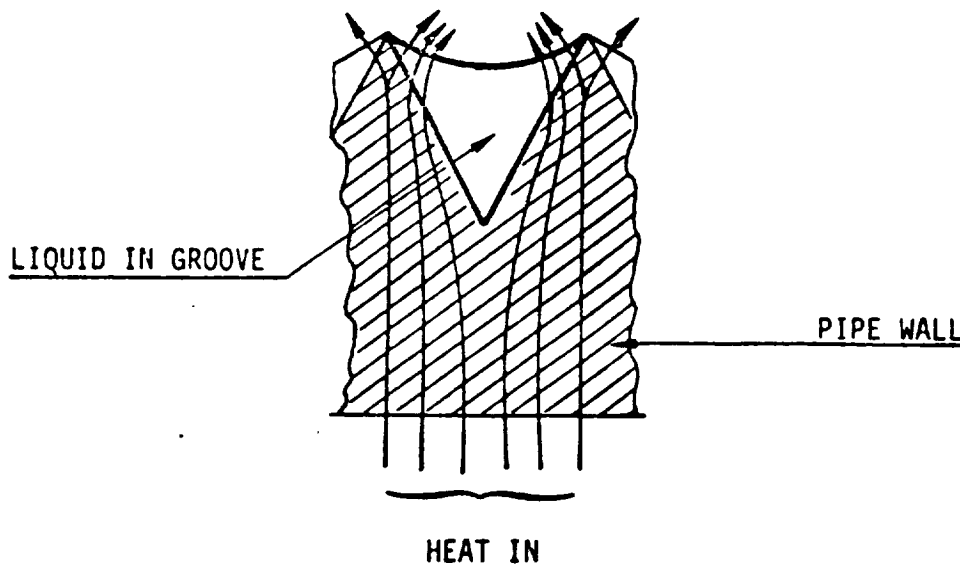


FIGURE 4-7. Heat Flow Path for a Circumferentially Grooved Heat Pipe

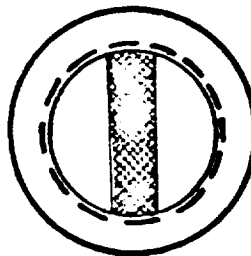
4.1.4.1 Designing Composite Wicks

The composite wick geometries shown in Fig. 4-6 represent but a small fraction of those which have been employed in heat pipe design. Many additional configurations are possible which serve the same primary purposes. These are:

- (1) To de-couple flow resistance from capillary head
- (2) To de-couple radial heat transfer from axial fluid flow

Depending on the requirements of a particular application, one might wish to design for either one or both of these criteria. Thus, for liquid metal pipes where radial heat transfer through the liquid poses no problem, the annular artery (Fig. 4-6a), which only accomplishes criterion (1), represents an excellent design.

Should an application arise which requires a heat pipe with a very low overall temperature drop but not a particularly high axial heat transport capacity, the best design might be based on criterion (2) alone. Such a design is shown in Fig. 4-8. The axial fluid flow is carried in a primary homogeneous wick, while the circumferential fluid flow and radial heat transfer are handled by circumferential grooves cut in the pipe wall. With such designs, the wick flow area can be increased without affecting the input or output temperature drop.



HOMOGENEOUS WICK/CIRCUMFERENTIAL GROOVES

FIGURE 4-8. Non-Arterial Composite Wick Design -
Radial Heat Transfer De-coupled from
Axial Liquid Flow

In many applications, however, the requirements call for both high axial heat transport capacity and low temperature drop. Since the working fluids suitable for spacecraft thermal control are characterized by low thermal conductivities, this often calls for a design which satisfies both criteria. One then requires arterial heat pipes such as those shown in Fig. 4-6b, c, d.

When designing homogeneous wick heat pipes of the class shown in Fig. 4-8, one uses the same design criteria discussed previously, with one important exception. Since the wick flow area can be varied without effecting the temperature drops, one can now optimize the homogeneous wick on hydrodynamic criteria alone. Boiling in the wick is no longer a factor (see Sec. 4.1.3).

When designing arterial heat pipes, however, the wick design criteria change. The purpose of arteries is to allow independent design of the capillary pumping head and the flow resistance. When the artery is completely filled with liquid the capillary head corresponds to the pore size of the material forming the artery while the flow resistance corresponds to the internal artery configuration. Since decreasing the pore size of the artery wall material does not alter the axial flow resistance, there is no longer an optimum pore size as discussed in Section 4.1.3. One wants to use the smallest pore size possible, consistent with (1) available materials, (2) fabricability, (3) pressure drop due to flow into or out of the artery itself, and (4) under certain circumstances, consideration of pore plugging due to erosion or mass transport.

The axial flow resistance of an artery is independent of the artery wall pores. It is determined solely by the internal artery dimensions (e.g., the gap sizes in Fig. 4-6a, c; the groove dimensions in Fig. 4-6b; the artery diameter in Fig. 4-6d). To decrease flow resistance one simply increases these dimensions.

In the absence of body forces (e.g., gravity, centrifugal force, etc.) there is no theoretical limit to the size of the artery other than the geometry of the heat pipe. However, if the pipe must operate in a body force field such as is required for 1-g testing, a constraint is added. It is true that an artery, once filled with liquid, will remain full under expulsive forces up to the maximum capillary head producible by the pores of the artery wall. However, should the artery be partially or fully depleted of liquid, it is necessary to design for automatic refill; i.e., the artery should be self-priming under the surface tension forces provided by its internal dimensions.

The self-priming requirement establishes a limit on the internal dimensions of an artery. For example, the gap of an annular artery (Fig. 4-6a) develops a capillary head given by:

$$\Delta P_{cmax} = \frac{2\sigma}{\delta} \cos\psi \quad (4-32)$$

where δ is the gap width.

For a horizontal heat pipe in a 1-g field, this artery will self-prime if ΔP_{cmax} exceeds the hydrostatic head of liquid corresponding to the pipe diameter.

$$\frac{2\sigma \cos\psi}{\delta} > \rho_l D_w \frac{g}{g_0} \quad (4-33)$$

Thus, the maximum gap size is given by:

$$\delta \leq \frac{2\sigma \cos\psi}{\rho_l D_w g/g_0} \quad (4-34)$$

From a practical point of view, the gap width must be designed smaller than that given by Eq. (4-34). One should always allow a safety factor for manufacturing tolerance. However, even more important in very long heat pipes, it may not be possible to test the pipe in a perfectly horizontal position. Any deviation from horizontal must be added to

the D_w term in Eq. (4-34), since the priming requirement of the liquid is from the lowest point in the system to the highest point within the artery.

In the annular artery heat pipe treated as an example, the self-priming requirement establishes the maximum size of the artery. This, however, does not limit the capacity of a heat pipe since multiple arteries can be used. Fig. 4-6c shows an example of a series of partial annular arteries stacked side by side. Each gap is sized to self-prime; but by placing several in parallel, a large flow capacity can be achieved. Similarly, the screen covered grooves of Fig. 4-6b actually represent a series of arteries where each of the grooves is sized to self-prime.

A final consideration regarding arterial priming is whether or not the artery must self-prime under load. The self-priming criteria previously discussed refer to the case where there is no heat transfer load on the heat pipe. However, it will often be the case in actual applications that it is not possible to completely remove the load on a heat pipe to allow self-priming in the event of arterial failure. For example, the artery of a spacecraft heat pipe may be drained of liquid during launch, and expected to self-prime when the spacecraft enters orbit. It may well be possible to provide reduced load conditions during this phase of the time-line, but it will seldom be possible to provide zero load conditions.

To establish the load under which an artery can self-prime, one uses a criterion similar to that for no-load priming except that the flow losses (pressure drops) are added to the relevant body forces when equated to the capillary head generated by the internal artery dimensions (not the artery wall). For example, Fig. 4-9 shows the self-priming capacity for a pedestal artery as a function of the artery diameter, using ammonia as a working fluid. It is interesting to note that, under 0-g conditions, the load under which the artery can self-prime continually increases with artery diameter, since the flow resistance decreases more

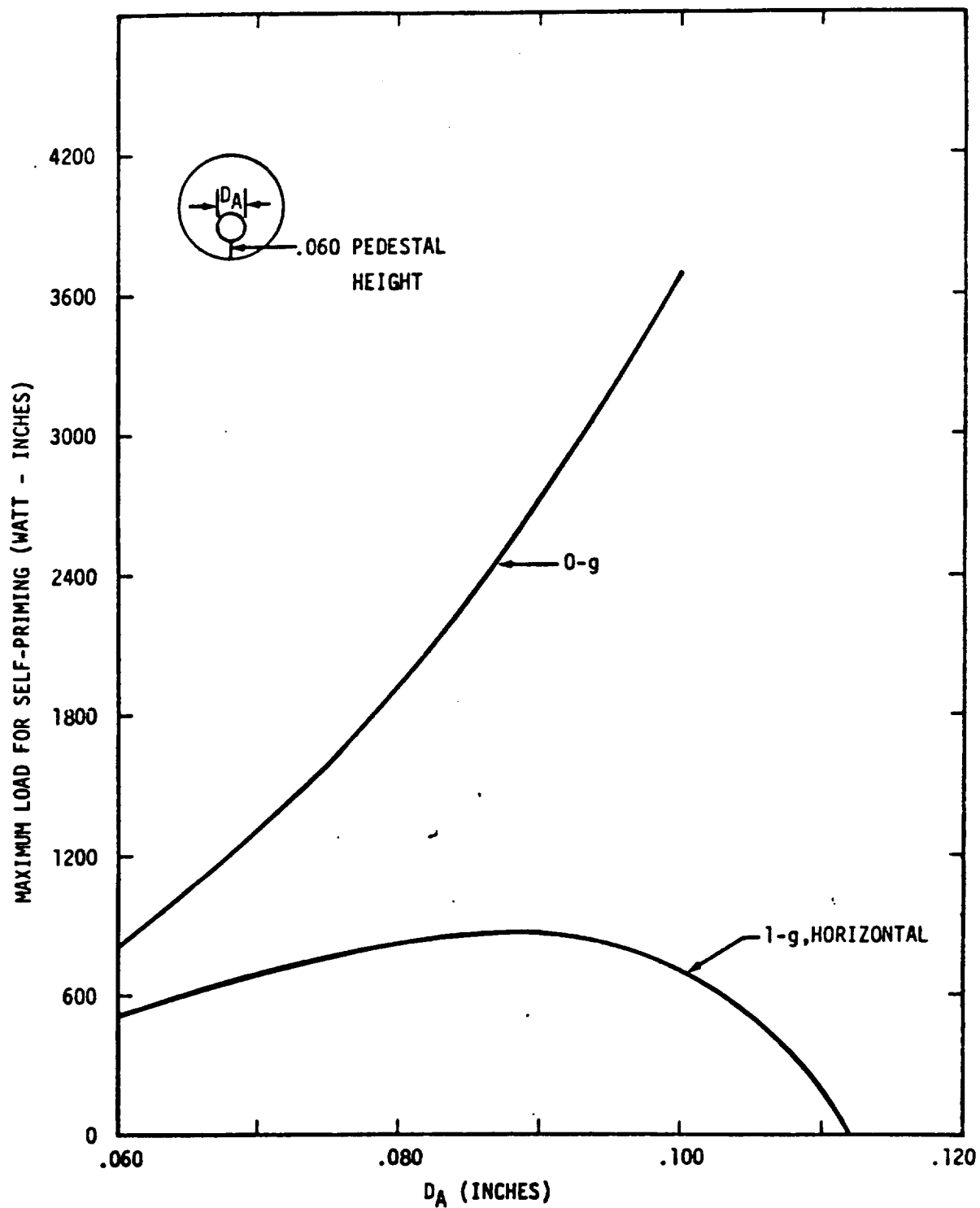


FIGURE 4-9. Self-Priming Capacity of Pedestal Artery Heat Pipe with Ammonia Working Fluid

rapidly ($\propto \frac{1}{D_A^4}$) than the capillary head ($\propto \frac{1}{D_A}$). On the other hand, for a horizontal pipe under 1-g conditions, an optimum artery size exists by virtue of the hydrostatic head which "comes off the top" of the available capillary head.

It should also be noted that the maximum load for self-priming also represents the capacity of the artery if the evaporator end were not sealed.

Although the heat transfer and hydrodynamic design of arterial pipes is fairly straight forward, arteries are characterized by several unique design and manufacturing problems.

As discussed earlier, the local maximum capillary head of a filled artery is determined by the largest available pore or opening. This requires careful fabrication of the artery to assure it is sealed along its length and at the evaporator end.

A more elusive problem is to assure that the artery is completely filled. If an artery contains bubbles, the maximum capillary head will not correspond to the pores of the artery wall but to the bubble radius. If the bubble locally fills the artery, this reduces to the capillary head of the artery itself. In either case, the pumping capability of the artery is very much reduced. (In the latter case, it is reduced to the self-priming capacity.)

There are several ways in which bubbles can be generated in an artery. As discussed previously, if the liquid in the artery is sufficiently superheated, nucleation of vapor bubbles is possible. Furthermore, even if boiling does not occur within the artery itself, boiling in close proximity could lead to vapor penetration.

It is also possible to generate arterial bubbles during initial fill or any subsequent repriming of the artery made necessary by liquid expulsion

due to vibration, shock, excessive tilting, excessive heat load, etc. If the artery walls are self-wetting, they are generally wetted before the interior fills, permitting bubbles to be trapped inside.

A third mechanism for generating arterial bubbles is peculiar to heat pipes which contain non-condensable gases, whether to aid in start-up from the frozen state or for use in gas-controlled variable conductance heat pipes. Under operating conditions, the non-condensable gas in such heat pipes is swept to the condenser end where it forms a gas plug. This gas plug acts as a diffusion barrier to the flowing vapor, causing the blocked region of the condenser to fall in temperature. Because the solubility of gases in liquids varies inversely with temperature, the axial temperature gradient caused by gas blockage represents a potential bubble forming mechanism within arteries. The gas dissolves in the liquid at the cold, gas-blocked region of the condenser. As the liquid flows back to the hot evaporator, part of the gas comes out of solution due to its decreased solubility at the higher temperature.

The formation of arterial bubbles would not represent a particularly serious problem if mechanisms existed for their rapid elimination under ordinary operating conditions. Unfortunately, this does not appear to be the case.

The fact that the artery is sealed everywhere* by a wetted wall makes physical expulsion usually impossible. By using a non-self-wetting artery wall (e.g., a single layer of screen), Bienert [G-16] has demonstrated that the artery wall can be locally dried by overheating, allowing bubbles to escape. However, this approach will often be unacceptable in actual applications in that it involves at least a temporary failure of the arterial system.

*Under conditions where one portion of the heat pipe always represents the condenser, the artery need not be sealed at that end.

If the bubbles cannot escape through the artery wall, the remaining removal mechanism is for them to collapse. Pure vapor bubbles will rapidly collapse within a uniform temperature, non-superheated liquid due to surface tension forces. However, if the liquid in the artery is superheated, vapor bubbles of sufficient size will grow and displace the liquid in that region.

Unfortunately, it is also possible to sustain relatively stable bubbles within a non-superheated artery if they contain non-condensable gas. Relatively small quantities of non-condensable gas within the bubbles can increase their internal total pressure (vapor pressure plus partial pressure of gas) sufficiently to stabilize them against the surface tension forces trying to collapse them. In an operating heat pipe, such bubbles can only collapse by the diffusion of the stabilizing non-condensable gas through the wetted artery wall into the vapor core. This is, however, a very slow process. Bienert [G16] reports typical collapse rates of elongated arterial bubbles on the order of $\sim 10^{-4}$ cm/sec.

In view of these bubble stability considerations, what can the heat pipe designer do to assure successful operation of arterial heat pipes? In the first place, it appears that fabricating the artery with non-self-wetting walls (e.g., a single layer of screen) avoids the problem of bubble entrapment during arterial priming. Second, one should design to avoid arterial superheat. If the hydrodynamic requirements permit, this can be assured by utilizing a "hybrid" wick design where the artery is constrained to the condenser and adiabatic section, and a homogeneous wick is utilized in the superheated evaporator section. This simultaneously avoids problems of nucleation within the artery and penetration of vapor due to boiling in close proximity to the artery. Also, it assures that pure vapor bubbles within the artery will collapse.

Finally, there remains the problem of eliminating gas-stabilized bubbles in heat pipes containing non-condensable gases. At this point, the only practical removal mechanism which has been identified is diffusion of

the stabilizing gas out of the artery through the wetted artery wall. Although this is indeed a slow process, the significance of the rate is only in comparison with the rate in which such bubbles are formed. If, through proper design, one avoids entrapment of bubbles during priming, and generation or penetration of bubbles due to boiling, the only apparent mechanism for bubble formation is that due to gas accumulation as a consequence of an existing temperature gradient combined with the inverse solubility of gas in the liquid. However, this is also a very slow process. Thus, the relevance of this problem is a question of relative rates of gas accumulation by virtue of solubility variations and gas removal by diffusion.

To the author's knowledge, this problem has not yet been treated analytically and thus no general statements can be made. There is, however, some limited experimental data available which indicate that, at least in certain cases, the gas removal rate by diffusion is sufficient to avoid gas accumulation in the artery. Long term successful operation of gas-loaded arterial heat pipes has been achieved at TRW for water-nitrogen with an annular artery (Fig. 4-6a) and methanol-nitrogen with an asymmetric artery (Fig. 4-6c). In addition, successful life tests of ammonia-helium systems with a pedestal artery (Fig. 4-6d) have been reported in the literature [G8].

4.2 Fluid Inventory

An important design consideration in the manufacture of all heat pipes is to determine the appropriate quantity of working fluid with which to fill the pipe. Excess fluid in a heat pipe is undesirable from two points of view. First, under 0-g conditions (and, in some cases, 1-g conditions) the constant flow of vapor from evaporator to condenser pumps the excess fluid to the condenser end, forming a liquid plug which "shuts off" that portion of the condenser which it fills. If the application calls for a short condenser length, this could be a critical factor. Second, excess fluid in a heat pipe can slosh within the vapor core, leading to undesirable effects on spacecraft dynamics.

On the other hand, a deficiency of working fluid is also undesirable. If the capillary structure is characterized by a single pore size (e.g., identical axial grooves), the fluid deficiency appears at the evaporator end leading to local dryout. The degree of dryout which can be tolerated depends on the particular application and how much axial conduction the pipe wall (or saddles, etc.) can provide.

If the heat pipe contains an artery, even a small fluid deficiency will prevent the artery from filling, leading to grossly reduced performance.

The most tolerant wick system with respect to underfill is a homogeneous wick with a pore size distribution (e.g., metal felt). In this case the fluid deficiency does not all appear at the end of the evaporator, but is spread among the larger pores all along the wick. The small pores in the evaporator continue to pump liquid.

Once again, however, the pumping capacity of the wick will be reduced. Because the wick is partially desaturated, the liquid flow area is reduced. To make matters worse, it is the largest pores (those of minimum flow resistance) which are unavailable for flow. Furthermore, the available capillary head is reduced because the maximum local liquid pressure need no longer be equal to the vapor core pressure (see Sec. 3.1.6). Instead it will be reduced by the capillary head corresponding to the largest pores which remain filled at the point of zero axial condenser flow.

We thus see that, qualitatively, homogeneous wicks can tolerate underfill but with reduced capacity. To analytically quantify the reduction in capacity requires detailed knowledge of the pore size distribution in the wick and the permeability as a function of desaturation. Since this information is generally not available for homogeneous wicks, it is currently necessary to determine the effects of underfill empirically for the particular wick involved.

4.2.1 Fluid Inventory Variations

According to the previous discussion, there are undesirable consequences of either over-filling or under-filling a heat pipe. Ideally, one should introduce just enough inventory to completely saturate the wick structure. Unfortunately, this is generally impossible in practical heat pipes. This is because both the liquid volume and the wick inventory requirements vary within a given heat pipe as a function of operating conditions. Several phenomena leading to this behavior are as follows:

- If a wick is saturated under no-load conditions, fluid will be expelled when the pipe is under load due to meniscus recession at the wick surface.
- If boiling occurs in the evaporator, fluid will be expelled by vapor within the wick.
- Homogeneous wicks with pore size distributions can partially desaturate when operated in a body force field (e.g., tilted against gravity).
- The liquid density, the vapor density and the void volume all vary with operating temperature, but not in proportion to each other. Consequently, 100% fill at one temperature corresponds to either over-fill or under-fill at other temperatures.

The relative importance of these phenomena depend on the type of wick structure used and the nature of the application. However, for space-craft thermal control heat pipes, the most troublesome source of volume variation is the last one. Fortunately, this problem can be handled analytically.

The following assumptions are made in the analysis:

- (1) The pipe has a constant cross-section along its entire length.
- (2) The wick is always fully saturated.

- (3) The pipe is filled to 100% theoretical at temperature T_0 .
- (4) Thermal expansion or contraction of the wall and wick is negligible compared with liquid and vapor density variations. Calculations have shown that this is a very good assumption.

The basis of the analysis is that the mass of working fluid within the heat pipe is a constant. Thus,

$$m = \rho_l V_l + \rho_v V_v = \text{constant} \quad (4-35)$$

where:

- m - mass of working fluid
- ρ_l - liquid density
- ρ_v - vapor density
- V_l - liquid volume
- V_v - vapor volume

Using the subscript "0" for conditions when the pipe is filled, and the subscript "T" for operating conditions, Eq. (4-35) can be written:

$$(\rho_l V_l)_0 + (\rho_v V_v)_0 = (\rho_l V_l)_T + (\rho_v V_v)_T \quad (4-36)$$

Solving Eq. (4-36) for V_{lT} yields:

$$V_{lT} = \frac{(\rho_l V_l)_0 + (\rho_v V_v)_0 - (\rho_v V_v)_T}{\rho_{lT}} \quad (4-37)$$

For uniform pipe cross-section and saturated wicks; and for the case of net liquid expansion:

$$\left. \begin{aligned} V_{l0} &= \phi A_w L_p \\ V_{v0} &= A_v L_p \\ V_{vT} &= A_v (L_p - L_{ex}) \end{aligned} \right\} \quad (4-38)$$

where:

- ϕ - wick porosity
- A_w - wick cross-sectional area
- A_v - vapor core cross-sectional area
- L_p - length of pipe
- L_{ex} - length of liquid slug in condenser
due to net liquid expansion

Substituting Eq. (4-38) into Eq. (4-37) yields:

$$V_{\ell T} = \frac{\rho_{\ell 0} \phi A_w L_p + \rho_{v0} A_v L_p - \rho_v A_v (L_p - L_{ex})}{\rho_{\ell T}} \quad (4-39)$$

But, the length of the excess liquid slug in the condenser can also be expressed in terms of volumes, lengths and areas, as follows:

$$L_{ex} = \frac{V_{\ell T} - V_{\ell 0}}{A_v} = \frac{V_{\ell T} - \phi A_w L_p}{A_v} \quad (4-40)$$

Now substituting Eq. (4-39) for $V_{\ell T}$ in Eq. (4-40), and performing some algebra, one arrives at the following expression for L_{ex}/L_p , the length of the excess fluid slug ratioed to the pipe length.

$$\frac{L_{ex}}{L_p} = \frac{(\rho_{\ell 0} - \rho_{\ell T}) \phi \frac{A_w}{A_v} + (\rho_{v0} - \rho_{vT})}{\rho_{\ell T} - \rho_{vT}} \quad (4-41)$$

Equation (4-41) is the desired result. It expresses the length of the excess fluid slug at any operating temperature as a function of the pipe geometry and the temperature at which it was filled to 100% of theoretical.

It is interesting to examine the behavior of this equation as a function of operating temperature. Fig. 4-10 shows this behavior for an ammonia heat pipe filled to 100% theoretical at 15°F. L_{ex}/L_p is plotted as a function of operating temperature with the geometrical grouping $\phi A_w/A_v$ as a parameter.

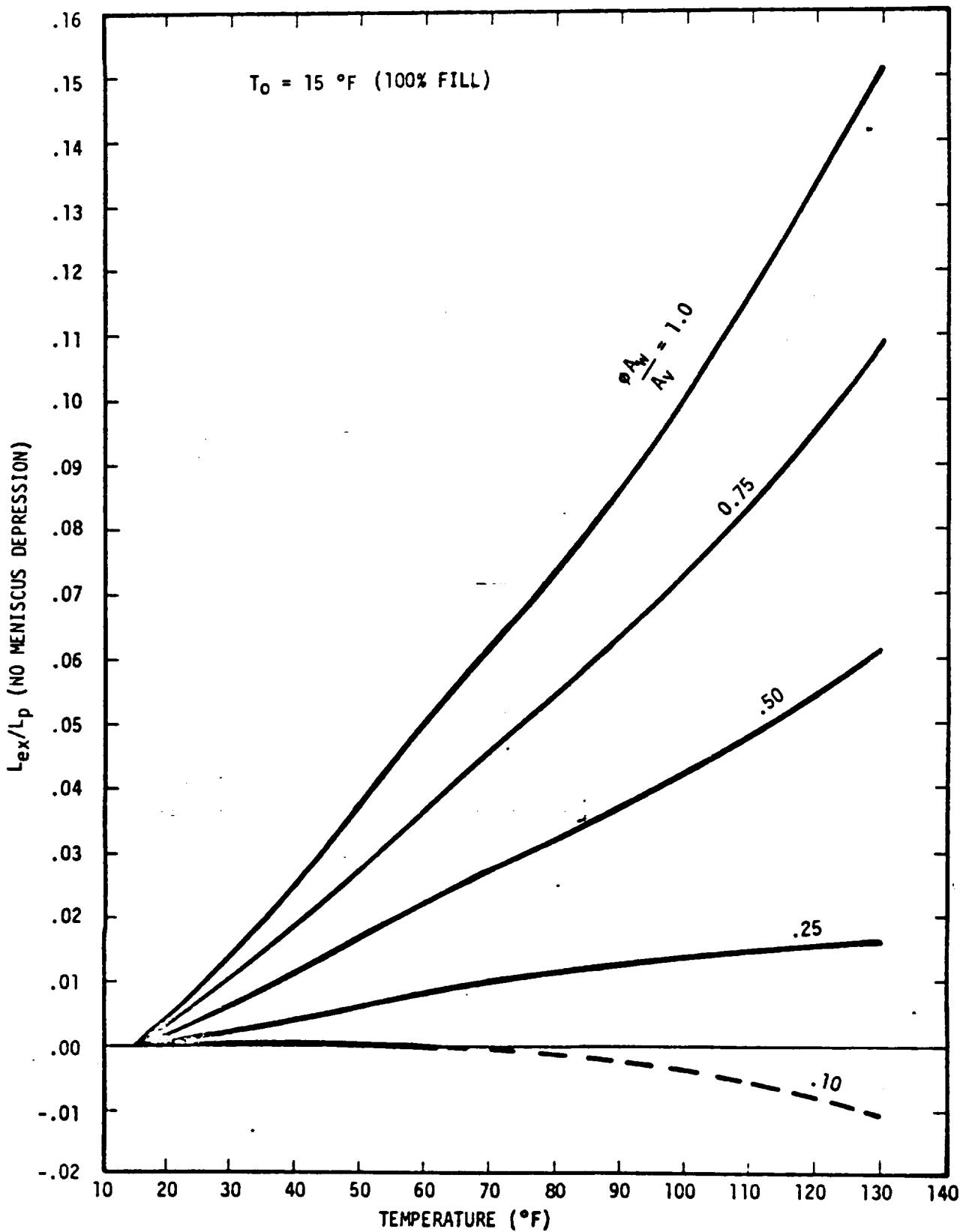


FIGURE 4-10. Liquid Volume Variation with Operating Temperature - Ammonia

As one would expect, the excess fluid slug, as a percent of pipe length, increases with the wick to vapor core area ratio. However, it is particularly interesting to note that L_{ex}/L_p does not necessarily increase with operating temperature. At low values of $\phi A_w/A_v$, L_{ex}/L_p can actually decrease with increasing T , and can even be negative.*

The reason for this behavior is that, although as temperature increases the liquid density decreases causing fluid expulsion, the vapor density also increases resulting in a conversion of liquid to vapor. If the liquid volume to vapor volume ratio is small enough ($\propto \phi A_w/A_v$), liquid to vapor conversion is greater than liquid expansion, and an increase in temperature results in a net decrease in liquid volume.

The critical value of $\phi A_w/A_v$ at which a change in operating temperature from T_0 to T results in no change in liquid volume can be deduced from Eq. (4-41) by setting L_e/L_p equal to zero. Thus,

$$\left(\frac{A_w}{A_v}\right)_{L_{ex}=0} = - \frac{\rho_{v0} - \rho_{vT}}{\rho_{l0} - \rho_{lT}} \quad (4-42)$$

The negative values of L_{ex}/L_p on Fig. 4-10 are, of course, not physically realistic, but correspond to the case of decreased liquid volume leading to wick desaturation. To obtain the percent desaturation for such cases, a similar analysis is performed in terms of a percent wick desaturation rather than L_{ex} .

The implications of these results depend, of course, on the type of wick system used. For example, heat pipes with arterial wicks generally have low values of the parameter $\phi A_w/A_v$. Thus, assuming a value of 0.1, an ammonia heat pipe which must operate above 60°F should be filled to 100% theoretical at the highest anticipated operating temperature, or else the artery would be partially empty and not function at that temperature.

*A negative L_{ex} is not a physical reality but corresponds to wick desaturation. More will be said about this later.

4.3 Excess Fluid Reservoirs

As discussed in the last section, it is not possible to fill a heat pipe such that it has 100% theoretical inventory under all operating conditions. However, as was also pointed out, both overfill and underfill conditions are undesirable. In fact, under certain circumstances, both conditions are intolerable. An example of such conditions would be a long, arterial heat pipe with a very short condenser. A fluid deficiency would result in failure of the artery while a fluid excess might block the condenser to an intolerable degree.

Under such circumstances, one can incorporate a capillary excess fluid reservoir in the wicking system. This concept, developed for the Ames Heat Pipe Experiment on this contract, is simply an additional capillary structure placed within the heat pipe to act as a "sponge". The pore size of the reservoir must be larger than any of those in the primary wick structure (including arteries) such that it does not draw liquid from the wick unless it is fully saturated. However, it will draw liquid from the tube itself, and thus prevents build-up of a liquid slug at the condenser end.

By using a capillary excess fluid reservoir, the pipe can be filled to 100% theoretical under minimum fluid volume and maximum wick saturation conditions. The reservoir volume should be sized to hold the maximum fluid excess generated by the anticipated variation in operating conditions. In this way, all fluid volume variations are taken up by the capillary reservoir. The primary wicks remain saturated and a condenser liquid slug is prevented under all operating conditions.

One must, however, use care in the sizing and placement of such "sponges" in the heat pipe. The simplicity of the concept under static conditions can lead to improper design, for the device must operate under dynamic conditions. Thus, the maximum capillary head generated by the excess fluid reservoir must not simply be larger than that of the vapor core, but must exceed the local liquid pressure depression in the wick. If not, the reservoir could not pump liquid from a slug at the end of the condenser.

Analytically, this criterion can be expressed as follows:

$$(\Delta P_{cmax})_{\text{reservoir}} > \left[\Delta P_{\ell} + \Delta P_v + \Delta P_b \right]_{(Z)}^{(Z)} p_{\ell} = p_v \quad (4-43)$$

where the bracket represents the integrated pressure losses from the position of the excess fluid reservoir to the point where the liquid and vapor static pressures are equal.

Graphically, this criterion is shown on Fig. 4-11 for a heat pipe operating in the absence of body forces (e.g., 0-g). Figure 4-11 represents a pressure balance curve similar to those discussed in Sec. 3.1.6. The bracketed terms on the right hand side of Eq. (4-43) are represented by the vertical distance between the ΔP_v and ΔP_{ℓ} curves.

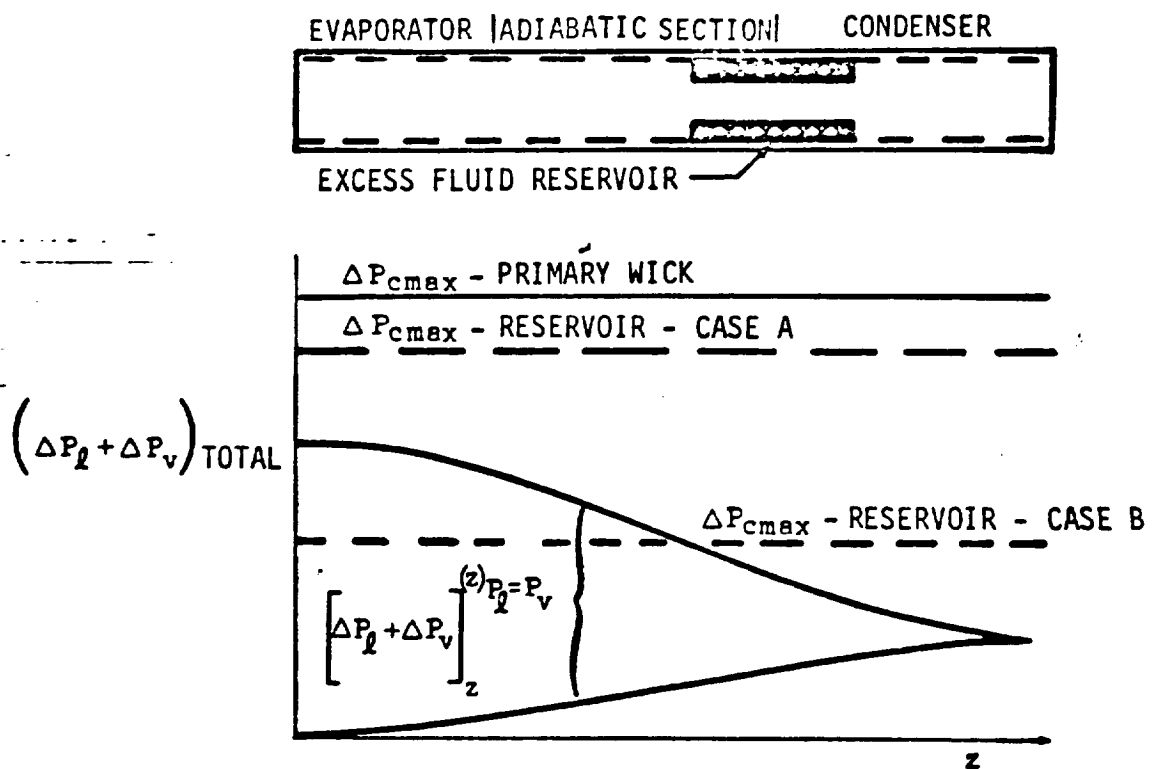


FIGURE 4-11. Pressure Balance Criterion for Locating Excess Fluid Reservoir

Thus, if $(\Delta P_{\text{cmax}})_{\text{res}}$ is greater than $\Delta P_{\ell} + \Delta P_v$ everywhere in the pipe, the excess fluid reservoir can be placed anywhere in the system (e.g., case A). On the other hand, if $(\Delta P_{\text{cmax}})_{\text{res}}$ is not greater than $\Delta P_{\ell} + \Delta P_v$ at all points (e.g., case B), the excess fluid reservoir must be placed in a region where this criterion does hold; i.e., to the right of the point where $\Delta P_{\ell} + \Delta P_v = (\Delta P_{\text{cmax}})_{\text{res}}$.

4.4 Working Fluid

The selection of the appropriate working fluid for a given application is based on many considerations. These include:

- (a) operating temperature range
- (b) heat transfer requirements
- (c) expected body-force field (e.g., 0-g, 1-g, etc.)
- (d) tolerance of wick structure to boiling
- (e) type of heat pipe (conventional or variable conductance)
- (f) special requirements
- (g) materials compatibility and stability

Brief discussions of these considerations follow.

4.4.1 Operating Temperature Range

Clearly, a heat pipe cannot be operated below the freezing point or above the thermodynamic critical point of its working fluid. Thus, the first criteria for selection of a fluid is that these two thermodynamic conditions bracket the required operating temperature range.

These conditions, however, actually represent lower and upper bounds which are seldom approached. Most often, the low end of a given fluid's operating temperature range is established by adverse vapor dynamics (sonic limit, entrainment limit, or simply excessive ΔP_v) due to low vapor densities and corresponding high vapor velocities. The high end of the temperature range is frequently set by the mechanical aspects of containing the fluid vapor pressure.

4.4.2 Heat Transfer Requirements

The axial heat transport requirement can have a major impact on the choice of working fluid. Different fluids will yield different capillary pumping limits for the same wick structure. Thus, the case can easily arise where a simple homogeneous wick design can be substituted for a complex arterial wick design by the choice of fluid.

To determine the best fluid for a given application, one must theoretically examine optimal designs for each fluid by integrating the loss equations to determine their respective capillary pumping limit (see Sec. 3.1.6). Sometimes this is actually necessary since, in the general case, there is no simple grouping of fluid properties which serves as a basis for selection. There do, however, exist such groupings for special cases which at least provide some general guidelines. Thus, for a heat pipe operating in the absence of body forces and for which the vapor pressure drop is negligible, the capillary pumping limit can be shown to be proportional to the grouping $(\sigma \rho \ell \lambda / \mu \ell)$, sometimes referred to as the "liquid transport factor" or "0-g figure of merit". Figure 4-12 shows the liquid transport factor for the principal fluids of interest in spacecraft thermal control as a function of operating temperature. Additional curves for many other fluids can be found in the literature [G4, G14, G17].

Although this grouping applies to the special case of negligible body forces and vapor pressure drop, those conditions do pertain to many spacecraft thermal control applications so that this is a valid basis of comparison for such heat pipes. However, as mentioned previously, it is not of general value. As Joy [G4] has shown, the presence of even small body forces (e.g., acceleration fields) can render this basis of comparison invalid for cryogenic fluids.

4.4.3 Expected Body-Force Field

As pointed out in the last section, the presence of body forces can have a major impact on the relative performance of various fluids. This situation is due to two phenomena: (1) the body force head is

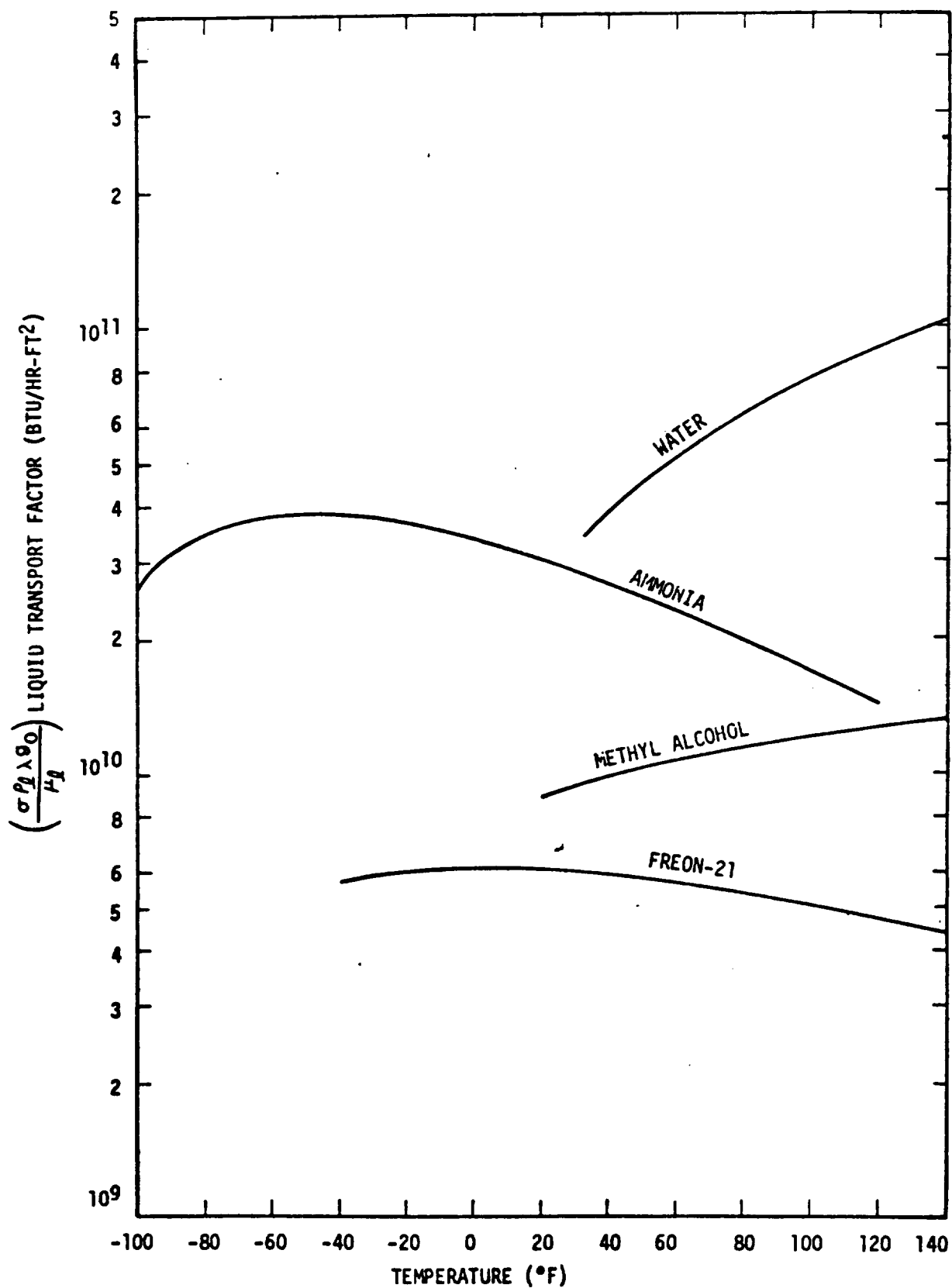


FIGURE 4-12. Liquid Transport Factor for Heat Pipe Working Fluids

subtracted from the maximum capillary head in establishing the pumping head available to overcome flow losses, and (2) the body force head must be overcome by surface tension effects in order to prime arteries, etc.

Since, in both cases, the problem is one of surface tension forces working against body forces, the ratio of these forces represents a basis of fluid comparison. In terms of fluid properties, this ratio is proportional to the grouping $(\sigma/\rho g)$. Thus, to minimize adverse body-force effects, one should select a fluid with a high value of this parameter. Fig. 4-13 shows the variation in $(\sigma/\rho g)$ with operating temperature for the principal spacecraft thermal control fluids.

4.4.4 Tolerance of Wick Structure to Boiling

In the last two sections, fluids were compared on the basis of their hydrodynamic and hydrostatic properties. However, as has been emphasized in this report, one must also consider radial heat transfer in the evaporator, especially if boiling would seriously degrade hydrodynamic performance (e.g., nucleation with arteries). The criteria for nucleation were discussed in Section 3.2.1.1. Assuming the critical radius (r_n) in Eq. (3-27) for the critical superheat is equal to the wick pore size, the pertinent fluid property grouping for superheat tolerance is $(\sigma/\lambda \rho_v)$. Multiplying this grouping by the thermal conductivity of the liquid yields a measure of the fluids' radial heat transfer tolerance with respect to nucleation. Fig. 4-14 shows the variation of this parameter $(k\sigma/\lambda \rho_v J)$ with operating temperature for the principal spacecraft thermal control fluids.

4.4.5 Conventional or Variable Conductance Heat Pipe

The fluid selection criteria discussed so far apply to all heat pipes. However, if one is designing variable conductance heat pipes, additional criteria may be involved, depending on the control scheme. Thus, heat pipes which employ vapor throttling as a control mechanism require low pressure working fluids. Similarly, the non-condensable

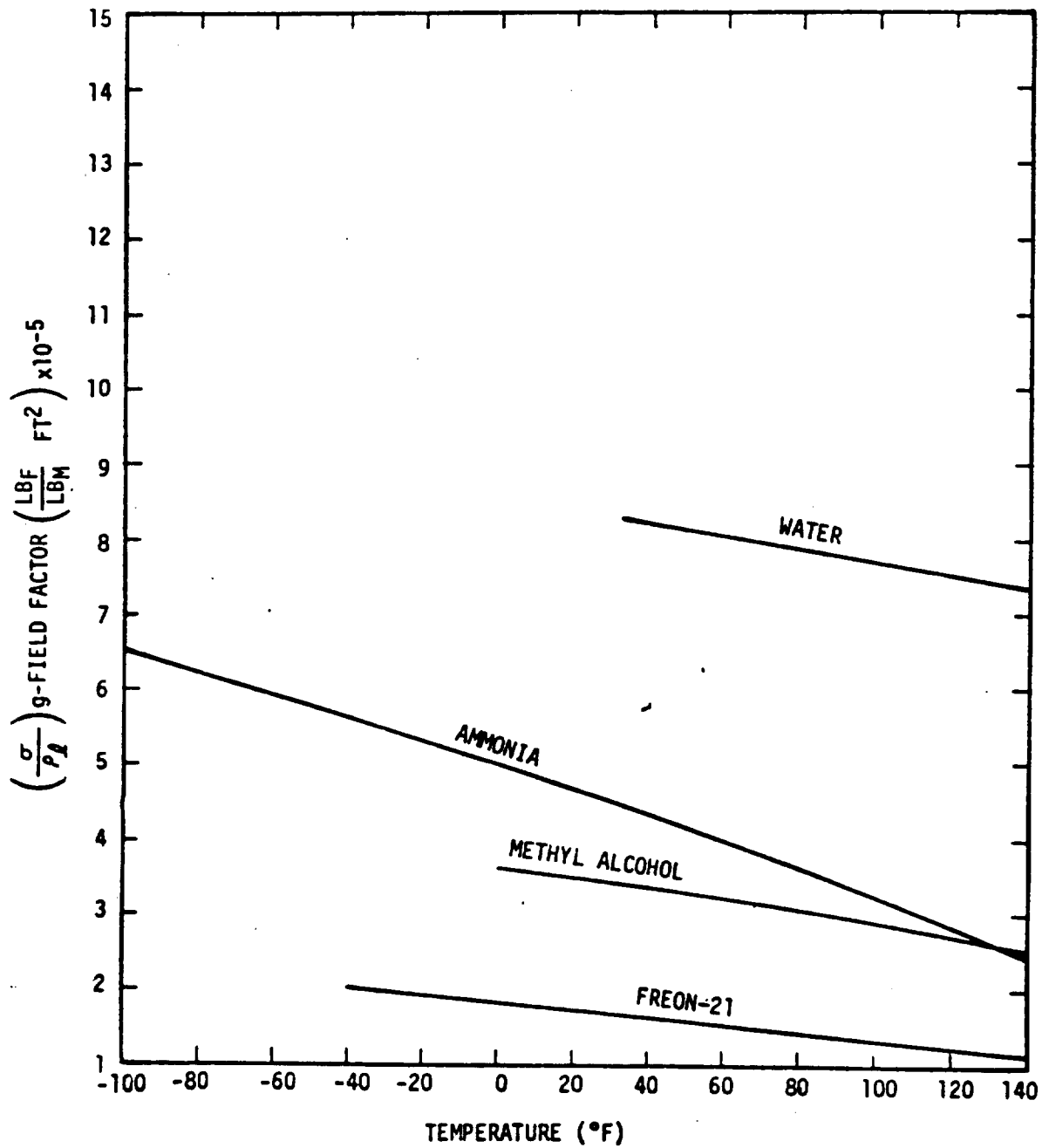


FIGURE 4-13. g-Field Figure of Merit for Heat Pipe Working Fluids

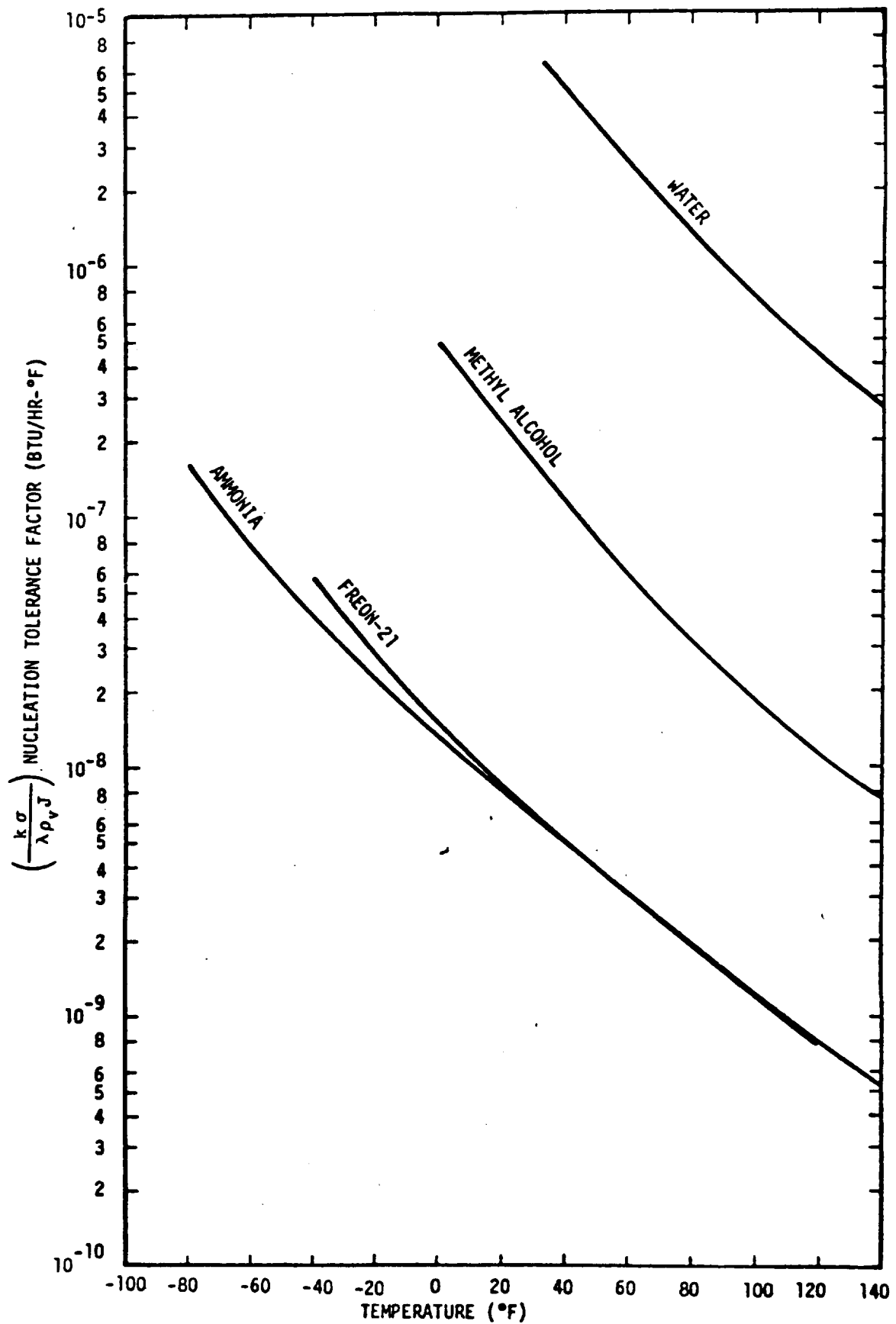


FIGURE 4-14. Nucleation Tolerance Parameter for Heat Pipe Working Fluids

gas control scheme provides additional selection criteria based on the slope of the vapor pressure curve.

The fluid property requirements imposed by the various variable conductance control schemes will be dealt with in Research Report No. 2.

4.4.6 Special Requirements

In addition to properties which affect the thermodynamic and hydrodynamic performance of heat pipes, there are other factors which can impose severe constraints on fluid selection for particular applications. For example:

- Many applications wherein the heat pipe concept is integrated into the packaging of electronic equipment will require the use of dielectric working fluids.
- Applications of heat pipes on-board manned spacecraft or aircraft may require the use of non-toxic and/or non-flammable working fluids.

4.4.7 Materials Compatibility and Stability

A major factor in selection of working fluids is their stability and compatibility with other materials in the heat pipe system. Certain low temperature heat pipes, of the type applicable to spacecraft thermal control, are subject to continuous performance degradation as a result of (1) chemical reaction or decomposition of the working fluid, or (2) corrosion or erosion of the container and wick.

Chemical reaction or decomposition of the working fluid may result in non-condensable gas evolution (e.g., H_2 , N_2 , O_2). A specific example of this is the hydrolysis of water yielding hydrogen gas when one attempts to build a water-aluminum heat pipe. In an ordinary heat pipe all non-condensable gas is swept to the condenser end, forming a diffusion barrier to vapor flow and effectively reducing the available condenser area. In gas controlled, variable conductance heat pipes, the generation of

additional non-condensable gas raises the operating temperature of the heat pipe above design conditions. Similar effects can result from a change in the chemical composition of the working fluid by virtue of a change in its vapor pressure as a function of temperature.

Corrosion and erosion of the container and wick can be manifested as a change in the wetting angle of the working fluid as well as the permeability, porosity, or capillary pore size of the wick. Solid precipitates resulting from corrosion and erosion are transported by the flowing liquid to the evaporator region where they are deposited when the liquid vaporizes. This leads to an increased resistance to fluid flow in the evaporator, resulting in a decrease in the heat transport capacity of the heat pipe.

At this point in time, there does not appear to exist any generally satisfactory way to predict stability or compatibility under arbitrary operational conditions. Consequently, faced with the need for such information, many heat pipe laboratories have run extensive test programs to empirically establish stable materials combinations and processing variables.

A widely used approach to compatibility testing is to employ actual heat pipe hardware and monitor the rate of gas generation with time. As mentioned previously, non-condensable gas generated within a heat pipe collects at the end of the condenser, blocking vapor flow and causing a local temperature drop (see Fig. 4-15). Thus, by monitoring the temperature distribution along an operating heat pipe, one has a measure of gas build-up as it actually affects performance. Note that the tests should be run with the condenser elevated above the evaporator to avoid artifacts due to fluid puddling.

Several such compatibility tests were performed on this contract as part of the development program leading to the Ames Heat Pipe Experiment on the OAO-C spacecraft. Control range considerations for this variable

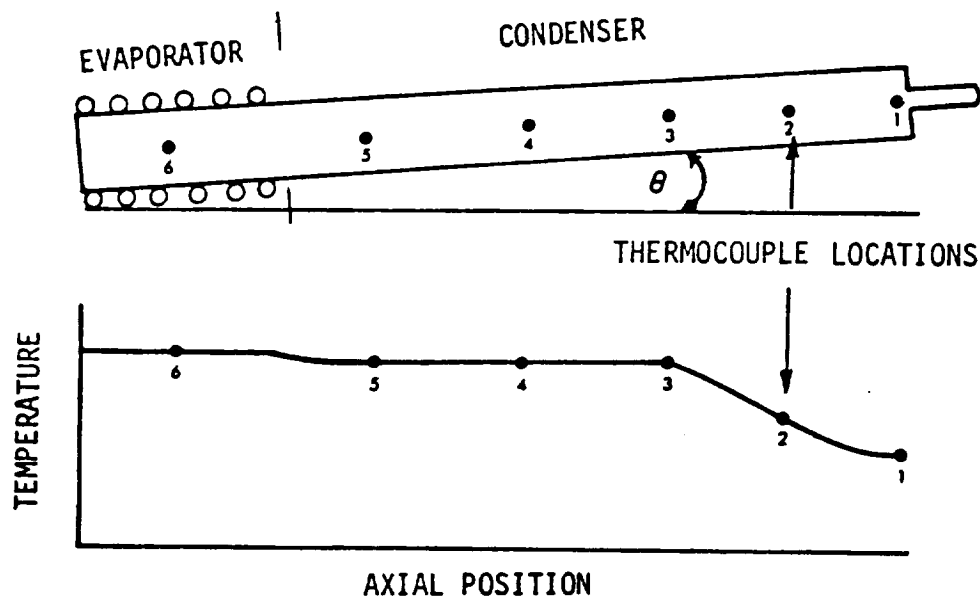


FIGURE 4-15. Schematic Diagram of Gas Generation Compatibility Test

conductance heat pipe led to the choice of methanol as the working fluid and stainless steel as the wick and container material. Because the heat pipe was to operate at $65 \pm 5^\circ\text{F}$ the internal pressure would be quite low (~ 2 psia) and the pipe would thus be very sensitive to even small quantities of gas generation.

Four 304 stainless steel/methanol heat pipes were fabricated utilizing different surface and fluid preparation techniques. After ultrasonically cleaning all parts in various solvents and firing all parts in dry hydrogen at 1200°C , two of the pipes were vacuum fired at 1100°C for two hours and two were oxidized in air at 500°C for one hour. The methanol used in all cases was spectrophotometric grade. However, in two pipes the fluid was used as received while, in the second two, it was specially dried by passing it through dried molecular sieve. The following material/fluid matrix was thus established.

<p>No. 100</p> <p>Vacuum fired S.S.</p> <p>Specially dried methanol</p>	<p>No. 101</p> <p>Vacuum fired S.S.</p> <p>As received methanol</p>
<p>No. 102</p> <p>Oxidized S.S.</p> <p>Specially dried methanol</p>	<p>No. 103</p> <p>Oxidized S.S.</p> <p>As received methanol</p>

The four heat pipes were placed on continuing life test at $105^{\circ} \pm 5^{\circ}\text{F}$ and the temperature profiles recorded periodically. A typical result is shown on Fig. 4-16 where the temperature difference between thermocouples 1 and 5 (see Fig. 4-15) is plotted as a function of time. After 2200 hours with no apparent gas generation (except in H.P. No. 102*), the operating temperature was raised to $145 \pm 10^{\circ}\text{F}$ and the test continued. At this point, over 7000 hours of test data have been accumulated without evidence of any gas generation in pipe nos. 100, 101 and 103, nor additional gas generation in pipe no. 102 following apparent cracking of the methanol during an accidental high temperature excursion.

Although these test results can only be reliably applied to the fabrication of heat pipes using precisely the same processing techniques and operating at similar temperatures, they do provide the guideline that methanol/stainless steel is an acceptable combination. Many similar

*After 1300 hours of testing with no gas generation, pipe no. 102 experienced a severe overheat and heater burnout due to a malfunction in equipment. After installation of a new heater, the pipe exhibited about 8°F temperature gradient suggesting gas generation by cracking of the methanol. This temperature difference has remained constant in 6000 hours of additional testing, supporting the thesis that this was a decomposition rather than a corrosion type phenomenon. Unfortunately, the maximum temperature reached by the heat pipe during this excursion is not known.

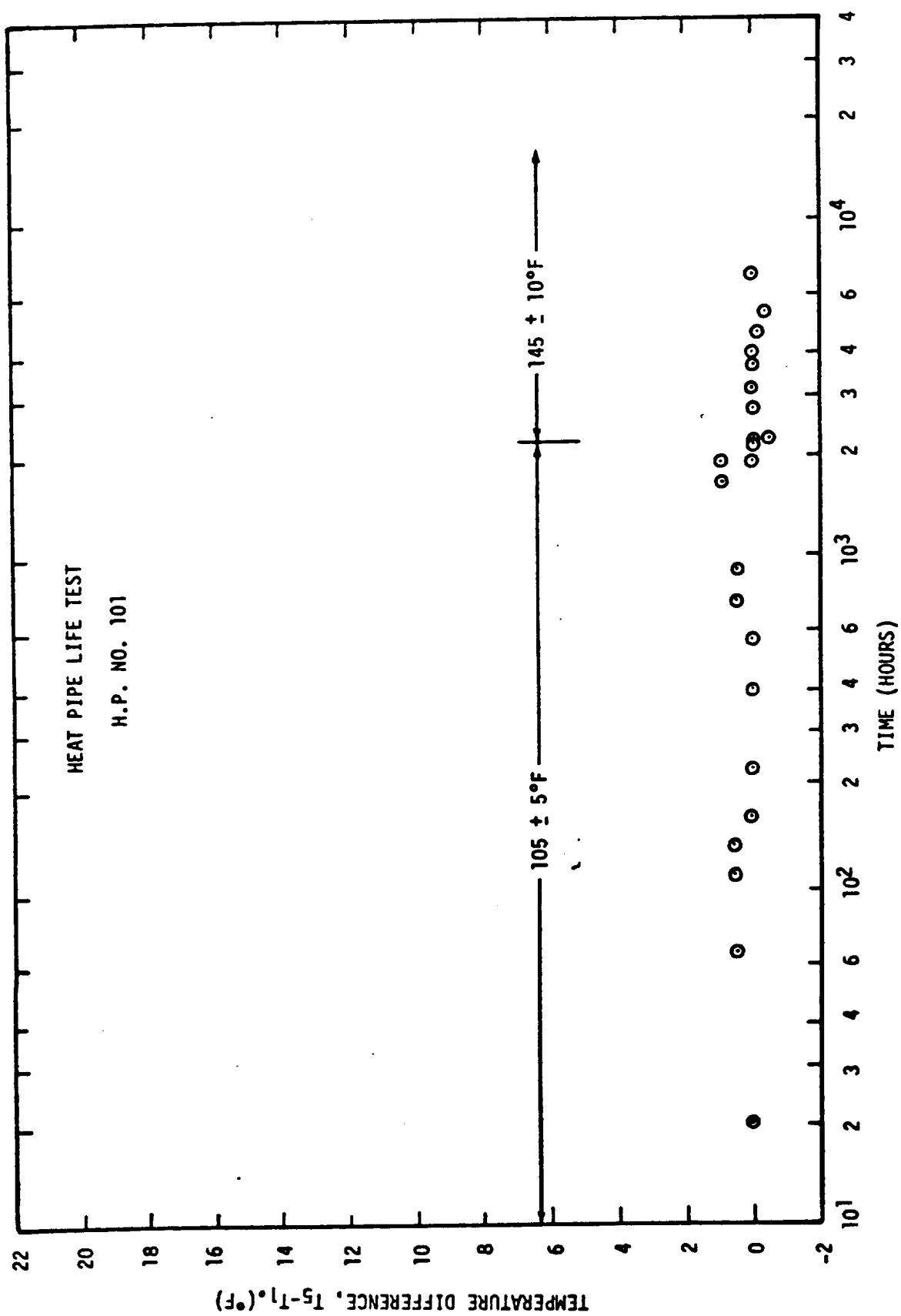


FIGURE 4-16. Compatibility Test Results - Heat Pipe No. 101

experiments have been performed by workers in the field, and although most of this work has not yet reached the open literature, enough has been reported to at least provide similar guidelines for most fluid/material combinations of interest in spacecraft thermal control.

Table 4-1 is a compilation of much of the available literature on this subject [M1, M2, M3, G7, G8, G17, G18]. The table indicates combinations of fluids and materials of construction which have been reported to be compatible or not on the basis of non-condensable gas generation. Of course, even in those cases listed as compatible, considerable attention must be given to cleanliness of the materials and purity of the working fluids to achieve satisfactory performance.

4.4.8 Summary

As is apparent from the previous discussion, the choice of working fluid depends very much on the requirements of the particular application. For the operating temperature range of interest in spacecraft thermal control, the four best working fluids are water, ammonia, methanol and Freon-21. In Table 4-2, these four fluids are ranked in terms of the various criteria discussed.

It would appear from the table that, from most points of view, water is the best fluid. In certain cases it will be. However, the high freezing point of water and its low vapor pressure at relevant temperatures limits its use to the high end of the thermal control range.

From a hydrodynamic point of view, ammonia is the next best fluid. Because this fluid is compatible with aluminum, it also allows for light weight heat pipes. It has very little superheat tolerance, however, and care must be used to avoid designs which are very sensitive to boiling, especially if the pipe contains non-condensable gases.

In the event that ammonia's toxicity is unacceptable, methanol and Freon-21 are alternatives. Methanol is the superior fluid thermodynamically, but its incompatibility with aluminum is a drawback, and it is still toxic. It is much less toxic than ammonia, however, and its sub-atmospheric vapor pressure at temperatures of interest prevents the expulsion of vapor into a controlled atmosphere (manned spacecraft) in the event of pipe failure.

If the application calls for a variable conductance heat pipe, additional fluid selection criteria are involved. These will be discussed in Research Report No. 2.

TABLE 4-2. Potential Heat Pipe Working Fluids for
Spacecraft Thermal Control

	(Ranking at 70°F)			
	Water	Ammonia	Methanol	Freon-21
Liquid transport factor ($\sigma \rho_L \lambda / \mu_L$)	1	2	3	4
g-field operation (σ / ρ_L)	1	2	3	4
Superheat tolerance ($\sigma / \lambda \rho_V$)	1	4	2	3
Toxicity	1	4	3	2
Flammability	1	2	4	3
Materials compatibility	3	1	2	?

5.0 SELECTED BIBLIOGRAPHY PERTINENT TO SPACECRAFT THERMAL CONTROL

5.1 Hydrodynamics & Hydrostatics

- H1 T. P. Cotter, "Theory of Heat Pipes", Los Alamos Scientific Laboratory, LA-3246-MS, March 1965.
- H2 D. M. Ernst, "Evaluation of Theoretical Heat Pipe Performance", Thermionic Conversion Specialist Conference--Conference Record, pp. 349-354, Palo Alto, Calif., 30 Oct - 1 Nov 1967.
- H3 C. L. Tien and K. H. Sun, "Minimum Meniscus Radius of Heat Pipe Wicking Materials", submitted for publication.
- H4 E. C. Phillips and J. D. Hinderman, "Determination of Properties of Capillary Media Useful in Heat Pipe Design", A.S.M.E. Paper No. 69-HT-18, 1969.
- H5 R. A. Farran and K. E. Starner, "Determining Wicking Properties of Compressible Materials for Heat Pipe Applications", Proceedings of the Annual Aviation and Space Conference, Beverly Hills, Calif., pp. 659-670, 16-19 June 1968.
- H6 C. A. Busse, "Pressure Drop in the Vapor Phase of Long Heat Pipes", Thermionic Conversion Specialist Conference--Conference Record, pp. 391-398, Palo Alto, Calif., 30 Oct - 1 Nov 1967.
- H7 G. H. Parker and J. P. Hanson, "Heat Pipe Analysis", ASME-Advances in Energy Conversion Engineering, pp. 847-857, August 1967.
- H8 G. A. Carlson, M. A. Hoffman, "Effect of Magnetic Fields on Heat Pipes", Lawrence Radiation Laboratory.
- H9 J. E. Kemme, "High Performance Heat Pipes", Thermionic Conversion Specialist Conference--Conference Record, pp. 355-358, Palo Alto, Calif., 30 Oct - 1 Nov 1967.
- H10 E. K. Levy, "Investigation of Heat Pipe Operating at Low Vapor Pressures", Proceedings of the Annual Aviation and Space Conference, Beverly Hills, Calif., pp. 671-676, 16-19 June 1968.
- H11 R. A. Freggens, "Experimental Determination of Wick Properties for Heat Pipe Applications", RCA Electronic Components, Paper #699108, Proceedings of the Fourth Intersociety Energy Conversion Engineering Conference, Washington, D. C., 1969.

- H12 L. S. Langston and H. R. Kunz, "Liquid Transport Properties of Some Heat Pipe Wicking Materials", ASME Paper No. 69-HT-17, 1969.
- H13 T. I. Sweeney, "The Performance of a Sodium Heat Pipe", A.I.Ch.E. Preprint No. 7, A.I.Ch.E.-A.S.M.E. Heat Transfer Conference, Minneapolis, 1969.
- H14 J. Bohdanský, H. Strub, and Evan Andel, "Heat Transfer Measurements Using a Sodium Heat Pipe Working at Low Vapor Pressure", Thermionic Conversion Specialist Conference--Conference Record, pp. 144-148, 1966.
- H15 J. E. Kemme, "Heat Pipe Capability Experiments", Los Alamos Scientific Laboratory, LA-3585-MS, August 22, 1966.
- H16 A. Carnesale, J. H. Cosgrove, J. K. Ferrel, "Operating Limits of the Heat Pipe", Proceedings of the Joint Atomic Energy Commission--Sandia Laboratories Heat Pipe Conference, Vol I, Sandia Corporation Report SC-M-66-623, Albuquerque, New Mexico, pp. 30-44, October 1966.
- H17 S. Frank, J. T. Smith, K. M. Taylor and W. J. Levedahl, "Heat Pipe Design Manual", Martin Nuclear Report MND-3288, Martin Marietta Corp., Baltimore, Md., February 1967.
- H18 A. E. Scheidegger, The Physics of Flow Through Porous Media, The Macmillan Co., pp. 68-90, 1960.
- H19 Sidney Frank, "Optimization of a Grooved Heat Pipe", ASME-Advances in Energy Conversion Engineering, pp. 833-846, August 1967.
- H20 F. J. Stenger, "Experimental Feasibility Study of Water-Filled Capillary-Pumped Heat-Transfer Loops", NASA-Lewis Research Center Report No. NASA TM X-1310, November 1966.
- H21 W. L. Haskin, "Cryogenic Heat Pipe", Technical Report AFFDL-TR-66-228, June 1967.
- H22 T. P. Cotter, "Heat Pipe Start-up Dynamics", Presented at the 1967 Thermionic Conversion Specialist Conference, Palo Alto, Calif., 30 Oct - 1 Nov 1967.
- H23 J. E. Deverall, "The Effect of Vibration on Heat Pipe Performance", LASL Report LA-3798, Oct 1967.
- H24 J. E. Deverall, et al, "Heat Pipe Performance in a Zero Gravity Field", J. Spacecraft Rockets, Vol. 4, No. 11, pp. 1556-1557, Nov 1967.

- H25 T. P. Cotter, "Status of the Engineering Theory of Heat Pipes", Proceedings of Joint Atomic Energy Commission/Sandia Laboratories Heat Pipe Conference, Vol. 1, NASA N67-26791, Rpt. No. SC-M-66-623 CONF-660645, Oct 1966.
- H26 J. E. Deverall and E. W. Salmi, "Heat Pipe Performance in a Space Environment", Thermionic Conversion Specialist Conference --Conference Record, pp. 359-362, Palo Alto, Calif., 30 Oct - 1 Nov 1967.
- H27 Johns Hopkins University, "The GEOS-2 Heat Pipe System and its Performance in Test and in Orbit", Report No. S2P-3-25, NASA CR-94585, NASA N68-23540, 29 April 1968.
- H28 J. K. Ferrell, "A Study of the Operating Characteristics of the Heat Pipe", Report No. ORO 3411-9, NASA N68-23098, 1 Nov 1967.
- H29 J. K. Ferrell and E. M. Schoenborn, "A Study of the Operating Characteristics of the Heat Pipe: Capillarity in Porous Media", Report No. ORO-3411-10, NASA N68-23099, 20 Feb 1968.
- H30 W. Bienert, et al, "Application of Heat Pipes to SNAP-29", Proceedings of Intersociety Energy Conversion Engineering Conference, Boulder, Colorado, pp. 477-486, 1968.
- H31 C. J. Feldmanis, "Feasibility Study of Low Temperature Cooling Systems", TM-68-1-FDFE, April 1968.
- H32 F. W. Holm, P. L. Miller, "Thermal Scale Modeling of a Heat Pipe", Texas A&M Univ., ASME Paper No. 70-HT/SpT-14, 1970.
- H33 M. Green, "An Improved Method of Calculating Frictional Pressure Losses Along Grooved Heat Pipes", Grumman Aircraft Engineering Corp., Bethpage, N.Y. Report No. ADN-04-02-69.1, June 1969.
- H34 J. W. Richardson, et al, "The Effect of Longitudinal Vibration on Heat Pipe Performance, J. Astronaut. Sci., V. 17, no. 5, Mar-Apr 70, p. 249-266.

5.2 Heat Transfer

- T1 A. E. Bergles and W. M. Rohsenow, A.S.M.E. Transactions, Journ. of Heat Transfer, August 1964.
- T2 D. W. Green and R. H. Perry, "Heat Transfer with a Flowing Fluid through Porous Media", Chem. Engr. Progress Symp. Series, Heat Transfer, Buffalo

- T3 R. L. Goring and S. W. Churchill, "Thermoconductivity of Heterogeneous Materials", Chemical Engineering Progress, Vol. 57, No. 7, pp. 53-59, July 1961.
- T4 M. M. Soliman, D. W. Grauman, P. J. Berenson, "Effective Thermal Conductivity of Saturated Wicks", AiResearch Manufacturing Co., ASME Paper No. 70-HT/SpT-40, 1970.
- T5 W. D. Allingham and J. A. McEntire, "Determination of Boiling Film Coefficient for a Heated Horizontal Tube in Water-Saturated Wick Material", J. Heat Transfer, pp. 71-76, Feb 1961.
- T6 C. P. Costello and E. R. Redeker, "Boiling Heat Transfer and Maximum Heat Flux for a Surface with Coolant Supplied by Capillary Wicking", Chem. Engr. Progress Symp. Series, No. 41, 59, pp. 104-113, 1963.
- T7 C. P. Costello and W. J. Frea, "The Role of Capillary Wicking and Surface Deposits in the Attainment of High Pool Boiling Burnout Heat Fluxes", AIChE Journal, 10, pp. 393-368, May 1964.
- T8 P. J. Marto and W. L. Mosteller, "Effect of Nucleate Boiling on the Operation of Low Temperature Heat Pipes", A.S.M.E. Paper No. 69-HT-24, 1969.
- T9 J. K. Ferrell, H. R. Johnson, "The Mechanism of Heat Transfer in the Evaporator Zone of a Heat Pipe", North Carolina State University, A.S.M.E. Paper No. 70-HT/SpT-12, 1970.
- T10 J. K. Ferrell and J. Alleavitch, "Vaporization Heat Transfer in Capillary Wick Structures", Chem. Eng. Prog. Symp. Ser. Vol. 66, 1970.
- T11 J. K. Ferrell and J. Alleavitch, "A Study of the Operating Characteristics of the Heat Pipe, Part III: Vaporization Heat Transfer From Flooded Wick Covered Surfaces", North Carolina State University Final Report No. ORO-3411-12, 158 p., 30 April 1969.
- T12 J. K. Ferrell and H. R. Johnson, "A Study of the Operating Characteristics of the Heat Pipe, Part IV: Heat Transfer in the Evaporator Zone of a Heat Pipe", North Carolina State University Final Report No. ORO 3411-12, 150 p., April 1969.

5.3 Materials Compatibility

- M1 J. Schwartz, "Performance Map of the Water Heat Pipe and the Phenomenon of Non-Condensable Gas Generation", ASME Paper No. 69-HT-15, 1969.

- M2 E. D. Waters and P. O. King, "Compatibility Evaluation of an Ammonia-Aluminum-Stainless Steel Heat Pipe", ASME Paper No. 70-HT/SpT-15, 1970.
- M3 A. Basiulis and M. Filler, "Operating Characteristics and Long Life Capabilities of Organic Fluid Heat Pipes", AIAA Paper No. 71-408, AIAA 6th Thermophysics Conf., 1971.
- M4 A. P. Shlosinger, Materials Research Report, TRW Systems No. 06462-6003-RO-00, NASA CR 73169, September 1967.
- M5 W. Woo, "Study of Passive Temperature and Humidity Control Systems for Advanced Space Suits - Material Research Report - Second Year", TRW Systems Report No. 06462-6007-RO-00, November 1968.

5.4 Variable Conductance Techniques

- V1 A. P. Shlosinger, "Heat Pipes for Space Suit Temperature Control", Proc. ASME Aviation and Space Conference, Beverly Hills, Calif., 1968.
- V2 D. K. Anand and R. B. Hester, "Heat Pipe Application for Spacecraft Thermal Control", Tech. Memo. DDC AD 662 241, NASA NG8-15338, 1967.
- V3 W. Bienert, "Heat Pipes for Temperature Control", Proc. 4th Intersociety Energy Conversion Engineering Conference, Washington, D.C., 1969.
- V4 R. C. Turner, "The Constant Temperature Heat Pipe--A Unique Device for the Thermal Control of Spacecraft Components", AIAA Paper No. 69-632, AIAA 4th Thermophysics Conference, 1969.
- V5 B. D. Marcus and G. L. Fleischman, "Steady-State and Transient Performance of Hot Reservoir Gas-Controlled Heat Pipes", ASME Paper No. 70-HT/SpT-11, 1970.
- V6 J. P. Kirkpatrick and B. D. Marcus, "A Variable Conductance Heat Pipe Flight Experiment", AIAA Paper No. 71-411, AIAA 6th Thermophysics Conference, 1971.
- V7 W. B. Bienert and P. J. Brennan, "Study to Evaluate the Feasibility of a Feedback Controlled Variable Conductance Heat Pipe", NASA CR 73475, 1970
- V8 W. B. Bienert, P. J. Brennan, and J. P. Kirkpatrick, "Feedback Controlled Variable Conductance Heat Pipes", AIAA Paper No. 71-421, AIAA 6th Thermophysics Conference, 1971.

- V9 J. D. Hinderman and E. D. Waters, "Design and Performance of Non-condensable Gas Controlled Heat Pipes", AIAA Paper No. 71-420, AIAA 6th Thermophysics Conference, 1971.
- V10 F. Edelstein and R. J. Hemback, "The Design, Fabrication and Testing of a Variable Conductance Heat Pipe for Equipment Thermal Control", AIAA Paper No. 71-422, AIAA 6th Thermophysics Conference, 1971.

5.5 General

- G1 G. M. Grover, T. P. Cotter and G. F. Erickson, "Structures of Very High Thermal Conductance", J. Appl. Phys. 35, 1990, 1964.
- G2 B. D. Marcus, "On the Operation of Heat Pipes", TRW Report 9895-6001-TU-000, May 1965.
- G3 L. S. Langston, et al, "Vapor-Chamber Fin Studies", Pratt & Whitney Aircraft, Final Report, NASA CR-812, June 1967.
- G4 ICICLE Feasibility Study, Final Report, NASA Contract NAS5-21039, RCA-Defense Electronic Products, Camden, New Jersey.
- G5 S. Katzoff, "Heat Pipes and Vapor Chambers for Thermal Control of Spacecraft", Paper No. 67-310, AIAA Thermophysics Specialist Conference, New Orleans, April 1967.
- G6 C. A. Busse, "Heat Pipe Thermionic Converter Research in Europe", Paper #699105, Proc. Fourth Intersociety Energy Conversion Engineering Conf., Washington, D. C., 1969.
- G7 O. W. Clausen, B. D. Marcus, et al, "Circumferential Heat Pipe System for Large Structures", Final Report, NASA Contract No. NAS 9-10299, 1970.
- G8 J. D. Hinderman, J. Madsen and E. D. Waters, "An ATS-E Solar Cell Space Radiator Utilizing Heat Pipes", AIAA 4th Thermophysics Conference, San Francisco, Paper No. 69-630, 1969.
- G9 P. E. Eggers and A. W. Serkiz, "Development of Cryogenic Heat Pipes", ASME Paper No. 70-WA/Ener-1, 1970.
- G10 A Luikov, Heat and Mass Transfer in Capillary-Porous Bodies, 1st Ed. Pergamon Press, New York, 1966.
- G11 E. Schmidt, Contribution a l'Etude des Calodues, Ph.D. Thesis, Univ of Grenoble, France, 1968.
- G12 W. M. Kays, Convective Heat and Mass Transfer, McGraw Hill, 1966.

- G13 R. Bird, W. Stewart and E. Lightfoot, Transport Phenomena, John Wiley & Sons, New York, 1960.
- G14 E. C. Phillips, "Low-Temperature Heat Pipe Research Program", NASA Report No. NASA CR-66792.
- G15 B. G. McKinney, "An Experimental and Analytical Study of Water Heat Pipes for Moderate Temperature Ranges", NASA Technical Memorandum Report No. 53849, June 6, 1969.
- G16 W. B. Bienert, "Fabrication and Evaluation of Aluminum Heat Pipes", Technical Summary Report, DTM-70-2, NASA Contract No. NAS5-11271.
- G17 E. E. Gerrels and J. W. Larson, "Brayton Cycle Vapor Chamber (Heat Pipe) Radiator Study", NASA CR-1677, 1971.
- G18 J. A. Bilenas, W. Harwell, "Orbiting Astronautical Observatory Heat Pipes--Design, Analysis and Testing", ASME Paper No. 70-HT/SpT-9, 1970.
- G19 K. T. Feldman and G. L. Whitlow, "Experiments with a Two-Fluid Heat Pipe", Proc. 4th Intersociety Energy Conversion Engineering Conf., Washington, D. C. Paper No. G99127, 1969.
- G20 F. E. Bliss, E. G. Clark, B. Stein, "Constructure and Test of a Flexible Heat Pipe", ASME Paper No. 70-HT/SpT-13, 1970.
- G21 S. W. Chi, T. A. Cygnarowicz, "Theoretical Analyses of Cryogenic Heat Pipes", Catholic Univ. of America, ASME Paper No. 70-HT/SpT-6, 1970.
- G22 A. Basiulis and J. C. Dixon, "Heat Pipe Design for Electron Tube Cooling", ASME Paper No. 69-HT-25, 1969.
- G23 C. L. Tien, "Two-Component Heat Pipes", AIAA Paper No. 69-631, AIAA 4th Thermophysics Conference, 1969.
- G24 H. Cheung, "A Critical Review of Heat Pipe Theory and Applications", Lawrence Radiation Lab, Calif. Univ. Livermore, Report No. UCRL 50453, July 1968, NASA N69-22519, 70 p.
- G25 J. E. Kemme, "Ultimate Heat Pipe Performance", Thermionic Conversion Specialist Conference-Conference Record, pp. 266-271, October 1968.
- G26 J. K. Ferrell, et al, "A Study of the Operating Characteristics of the Heat Pipe, Part I: An Analytical Model for the Prediction of Operating Limits of Heat Pipes, Part II: Capillarity in Porous Media", North Carolina State Univ. Final Report No. ORO 3411-12, 50 p., 30 April 1969.

- G27 E. van Andel, "Heat Pipe Design Theory", International Conference on Thermionic Electrical Power Generation, 2nd Proceedings, (Stresa, Italy, 27-31 May 1968), Luxembourg, EURATOM Center for Information and Documentation, (EUR no. 4210 f, e), 1969, 1438 p.
- G28 J. L. Thurman and S. Mei, "Application of Heat Pipes to Spacecraft Thermal Control Problems" Brown Engineering Co., Inc., Huntsville, Ala., Report No. TN-AST-275, July 1968, 102 p., NASA CR 109991, NASA N70-34436.
- G29 A. Basiulis, "Unidirectional Heat Pipes to Control TWT Temperature in Synchronous Orbit, p. 165-173, Thermodynamics and Thermophysics of Space Flight, Proceedings of the Symposium, Palo Alto, Calif., 23-25 March 1970, Sunnyvale, Calif., Lockheed Missiles and Space Co., 1970, 269 p.

6.0 NOMENCLATURE

A, A_w	- Wick cross-sectional area
A_F	- Flow area of groove, channel, etc.
A_v	- Vapor core flow area
CPL	- Capillary, pumping limit on axial heat transport
D_A	- Artery diameter
D_e	- Effective pore diameter for axial flow
D_s	- Diameter of spheres in packed sphere bed
D_w	- Wick diameter
F	- Crimping factor for screens
F_b	- Body force
J	- Mechanical equivalent of heat
K	- Permeability
L, L_p	- Length of heat pipe
L_e, L_a, L_c	- Lengths of evaporator, adiabatic section and condenser
L_{ex}	- Length of excess fluid slug in condenser
M	- Mesh size for screen - wires per inch
P_l	- Local pressure in liquid
P_v	- Local pressure in vapor core
P_w	- Wetted perimeter of groove, channel, etc.
Q	- Total axial heat transport
Q'	- Radial heat transport per unit length
Q_e	- Axial heat transport at entrainment
Q_s	- Axial heat transport at sonic limit
Q_{BL}	- Axial heat transport at boiling limit
R, R_1, R_2	- Meniscus radii of curvature
R_e	- Reynolds number
R_o	- Outside radius of pipe.
R_v	- Radius of vapor core
R_w	- Outside radius of wick
S	- Shape factor; safety factor
T_0	- Temperature at 100% theoretical fluid fill
T_{sat}	- Saturation temperature

- V - Velocity of vapor
- V_s - Sonic velocity of vapor
- V_v, V_l - Volume of vapor and liquid
- We - Weber number

- b - Tortuosity factor
- d - Wire or fiber diameter
- f - Effective pore size factor - parallel wire wick
- g - Magnitude of acceleration field
- k - Ratio of specific heats
- k_{eff} - Effective thermal conductivity of saturated wick
- k_l - Thermal conductivity of liquid
- k_s - Thermal conductivity of solid wick material
- m - Mass of fluid in heat pipe
- \dot{m}_l - Axial mass flow rate of liquid
- \dot{m}_v - Axial mass flow rate of vapor
- q'_r - Radial heat flux at evaporator
- r_e, r_{eA}, r_{eB} - Effective pore radius for capillary pumping
- r_h - Hydraulic radius
- r_n - Effective radius of nucleation cavity
- r_p - Radius of cylindrical pore; effective pore radius for axial flow
- r_s - Radius of spheres in packed sphere bed
- v_{lg} - Difference in specific volume between vapor and liquid
- v_o - Average liquid velocity
- w - Groove width - axial rectangular grooves
- z - Axial position; characteristic dimension for entrainment

- dV - Volume element
 ΔP_b - Body force head
 $\Delta P_{b_{\parallel}}, \Delta P_{b_{\perp}}$ - Components of body force head parallel and perpendicular to heat pipe axis
 ΔP_c - Net capillary head
 ΔP_i - Interfacial pressure difference
 ΔP_l - Liquid pressure drop
 ΔP_o - Wick "loading" - defined by Eq. (4-31)
 ΔP_v - Vapor pressure drop
 ΔT - Temperature difference
 ΔT_{crit} - Critical evaporator ΔT for nucleation
- β - Circumferential angle around pipe or wire
 δ - Wire spacing; gap width
 θ - Angle of heat pipe axis with respect to acceleration field vector
 λ - Latent heat of vaporization
 μ_l, μ_v - Viscosity of liquid and vapor
 ρ_l, ρ_v - Density of liquid and vapor
 σ - Surface tension
 ϕ - Wick porosity
 ψ - Wetting angle

Subscripts

- $avail$ - Available
 c - Condenser
 e - Evaporator
 f - Friction
 l - Liquid
 m - Momentum

min - Minimum
max - Maximum
opt - Optimum
v - Vapor